



Technische Universität München
TUM School of Natural Sciences

Discoveries in Ruthenium Oxide-Based Catalysts: From Morphology Control for Water Electrolysis to Surface Structure Determination via Machine-Learning

YONGHYUK LEE

DISSERTATION



Technische Universität München
TUM School of Natural Sciences

Discoveries in Ruthenium Oxide-Based Catalysts: From Morphology Control for Water Electrolysis to Surface Structure Determination via Machine-Learning

Yonghyuk Lee

Vollständiger Abdruck der von der TUM School of Natural Sciences der Technischen Universität München zur Erlangung des akademischen Grades eines

Doktors der Naturwissenschaften (Dr. rer. nat.)

genehmigten Dissertation.

Vorsitzender: Prof. Dr. Hubert A. Gasteiger

Prüfer der Dissertation:

1. Prof. Dr. Karsten Reuter
2. Priv.-Doz. Dr. Aras Kartouzian

Die Dissertation wurde am 23.09.2022 bei der Technischen Universität München eingereicht und durch die TUM School of Natural Sciences am 28.10.2022 angenommen.

*To my family
for their love, support and encouragement.*

*“Keep Ithaka always in your mind.
Arriving there is what you’re destined for.
But don’t hurry the journey at all.
Better if it lasts for years,
so you’re old by the time you reach the island,
wealthy with all you’ve gained on the way,
not expecting Ithaka to make you rich.”*

Constantine P. Cavafy

Preface

This dissertation is publication-based¹, thus its scientific content is published in a series of independent articles [1, 2], all of which have undergone the scientific peer-review process in international scientific journals. The first four chapters mainly deliver an introduction to motivations, backgrounds, methodologies, and further unpublished results. Summaries of both articles are then presented in chapter 5. The main part of the presented work was carried out at the Chair of Theoretical Chemistry of Technische Universität München (TUM) from September 2017 to December 2020, and it has been completed at Fritz-Haber-Institut der Max-Planck-Gesellschaft in Berlin from January 2021 and September 2022, under the supervision of Prof. Dr. Karsten Reuter.

München, September, 2022

¹The first paper [1] is a collaborative work with experimentalists, and I was in charge of all theoretical calculations and analysis within the paper.

Abstract

As air pollution and energy crises threaten the survival of mankind, various ways to efficiently obtain clean and renewable energies have been discussed in academia and industry. Amongst them, Power-to-X (P2X) conversions have been considered as important chemical reactions for future renewable energy generation. Hydrogen gas is one of the highly focused next-generation fuels in terms of the stability in supply as well as the suitability to buffer the fluctuation of energy supply from green power sources. Although water electrolysis is the most promising sustainable way to produce hydrogen, natural gas reforming techniques, which use fossil gases such as methane, still dominate the entire industry due to their economic efficiency. To overcome this, proton exchange membrane (PEM) water electrolyzers have been extensively studied due to their essential advantages. To date, a major drawback of PEM electrolysis is the sluggish kinetics of the oxygen evolution reaction (OER) at the anode and indispensable precious transition metal-based OER catalysts, which need to be durable under harsh acidic reaction conditions. Iridium oxide (IrO_2) has been known as the only active and stable catalyst under such conditions. However, the low abundance of iridium constrains the generalization of PEM techniques. A significant reduction of Ir mass loading on catalysts is thus required. Utilizing ruthenium oxide (RuO_2) is one promising way since it is more cost-efficient compared to IrO_2 . The only obstacle is the relatively poor stability of RuO_2 at OER operation conditions.

Morphology control via nanostructuring is an often used experimental approach to enhance stability. In predictive-quality computational science, many highly efficient morphologies have been proposed, however, long-term stability in industrial operating conditions and a possible subsequent transformation of the morphology have been rarely discussed. Consequently, there are still many longstanding questions on catalysts under working conditions. In this dissertation, structure-function and structure-stability relationships of RuO_2 based catalyst are mainly discussed by using first-principles density functional theory calculations. Two different types of structural modification in RuO_2 were discovered that promise better thermodynamic stability and enhanced OER activity. Furthermore, by combining state-of-the-art machine-learning methods with computational chemistry, the complex potential energy surface of rutile oxide materials was explored and hitherto unknown surface reconstructions of rutile RuO_2 were determined. The theoretical concepts and approaches developed throughout the dissertation may lay the platform for future works to design novel catalysts for PEM OER and other electrocatalytic reactions.

Zusammenfassung

Da die Luftverschmutzung und die Energiekrise das Überleben der Menschheit bedrohen, werden in Wissenschaft und Industrie verschiedene Möglichkeiten zur effizienten Gewinnung sauberer und erneuerbarer Energien diskutiert. Die Power-to-X (P2X)-Umwandlung wird dabei als wichtige chemische Reaktion für die künftige Erzeugung erneuerbarer Energie angesehen. Wasserstoffgas ist einer der am stärksten fokussierten Brennstoffe der nächsten Generation, sowohl im Hinblick auf die Stabilität der Versorgung als auch auf die Eignung, die Schwankungen der Energieversorgung aus grünen Stromquellen abzufangen. Obwohl die Wasserelektrolyse die vielversprechendste Methode zur nachhaltigen Herstellung von grünem Wasserstoff ist, dominiert noch die umweltschädliche Erdgasreformierung, bei der fossile Gase wie Methan verwendet werden, aufgrund ihrer wirtschaftlichen Effizienz. Um dies zu überwinden, wurden Wasserelektrolyseure mit Protonenaustauschmembran (PEM) aufgrund ihrer wesentlichen Vorteile eingehend untersucht. Ein großer Nachteil der PEM-Elektrolyse ist die bisher träge Kinetik der Sauerstoffentwicklungsreaktion (OER) an der Anode und die unentbehrlichen OER-Katalysatoren auf der Basis von wertvollen Übergangsmetallen, die unter den harschen sauren Reaktionsbedingungen haltbar sein müssen. Iridiumoxid (IrO_2) ist als einziger aktiver und stabiler Katalysator unter solchen Bedingungen bekannt und wurde kommerziell vermarktet, jedoch schränkt die geringe Häufigkeit von Iridium die Verallgemeinerung von PEM-Techniken ein. Daher ist eine deutliche Verringerung der Ir-Massenbeladung der Katalysatoren erforderlich. Die Verwendung von Rutheniumoxid (RuO_2) ist hierfür ein vielversprechender Weg, da es im Vergleich zu IrO_2 kostengünstiger ist. Das einzige Hindernis ist die relativ geringe Stabilität von RuO_2 unter OER-Betriebsbedingungen.

Die Morphologiekontrolle durch Nanostrukturierung ist ein häufig genutzter experimenteller Ansatz zur Verbesserung der Stabilität. Mittels quantitativer numerischer Simulation wurden bereits viele hocheffiziente Morphologien vorgeschlagen. Die Langzeitstabilität unter industriellen Betriebsbedingungen und die mögliche anschließende Umwandlung der Morphologie wurden jedoch kaum diskutiert. Folglich gibt es noch viele offene Fragen zu Katalysatoren unter Betriebsbedingungen. In dieser Dissertation werden solche Struktur-Funktions- und Struktur-Stabilitäts-Beziehungen von Katalysatoren auf RuO_2 -Basis hauptsächlich mit Hilfe von Dichtefunktionaltheorieberechnungen erörtert. Es wurden zwei verschiedene Arten von Strukturmodifikationen in RuO_2 entdeckt, die eine bessere thermodynamische Stabilität und eine erhöhte OER-Aktivität gewährleisten. Durch die Kombination modernster Methoden des maschinellen Lernens mit computergestützter Chemie wurde die komplexe potenzielle Energieoberfläche von Rutil-strukturierten Oxidmaterialien erforscht und bislang unbekanntes Oberflächenrekonstruktionen von Rutil- RuO_2 bestimmt. Die in der Dissertation entwickelten theoretischen Konzepte und Ansätze können die Grundlage für künftige Arbeiten zur Entwicklung neuartiger Katalysatoren für die PEM OER und andere elektrokatalytische Reaktionen bilden.

Contents

1 Introduction	1
2 Rutile Transition Metal Oxide Catalysts and Their Industrial Applications	5
2.1 Anodic Oxygen Evolution Reaction Catalysts in Acidic Media	6
2.1.1 Proton Exchange Membrane Electrolyzer	7
2.1.2 Reaction Mechanisms in Acidic Media	9
2.2 Note for RuO ₂ : CO Oxidation Catalyst	13
3 Computational Surface Science	17
3.1 Periodic Slabs and Approximations	18
3.2 Ab Initio Thermodynamics	20
3.2.1 Surface Free Energy in Gaseous Environments	21
3.2.2 Surface Free Energy in Aqueous Environments	26
3.3 Case Studies	27
3.3.1 OER and Tafel Slope at Core-Shell Surfaces	27
3.3.2 CO Oxidation at $c(2 \times 2)$ -RuO ₂ (100) Reconstruction	28
4 Machine-Learning Gaussian Approximation Potentials	33
4.1 Gaussian Process Regression	34
4.2 Representation of Atomic Environments	36
4.2.1 Two-Body Descriptor	36
4.2.2 Many Body Descriptor: Smooth Overlap of Atomic Positions	37
4.2.3 Model in the Thesis	38
4.3 Hyperparameter Selection in a Nutshell	39
4.3.1 Locality Test	39
4.3.2 Hyperparameters from Physics-Inspired Heuristics	40
4.3.3 Hyperparameters from Four-Fold Crossvalidation	41
4.3.4 UniversalSOAP	42
4.4 Case Study: $c(2 \times 2)$ RuO ₂ (100) Reconstruction	42
5 Publications	45
5.1 Ruthenium Oxide Nanosheets for Enhanced Oxygen Evolution Catalysis in Acidic Medium	46
5.2 Epitaxial Core-Shell Oxide Nanoparticles: First-Principles Evidence for Increased Activity and Stability of Rutile Catalysts for Acidic Oxygen Evolution	47
5.3 Further works	48
6 Summary, Conclusions, and Outlook	49
Acknowledgments / Danksagung	51

1 Introduction

A major challenge worldwide is to limit global warming to achieve climate neutrality. Contemporary climate changes have accelerated since the 20th century, provoked mainly by the emission of greenhouse gases (GHGs), such as carbon dioxide (CO_2) and methane (CH_4). According to the United Nations Intergovernmental Panel on Climate Change (IPCC), temperatures could rise by $2\text{ }^\circ\text{C}$ by 2050, creating a very high risk of threats to ecological and human systems [3]. The combustion of fossil fuels, particularly coal, petroleum, and natural gas, is the primary source of anthropogenic GHG emissions [4]. Therefore, to become climate-neutral, the only options are to decarbonize energy production and develop renewable energies.

In particular, renewable energy sources have attracted broad interest from industry and seen a rapid expansion in recent years as substitutes for fossil fuels. However, one of the largest obstacles to the energy transition is the fluctuating supply of renewable energies, such as wind and solar power [5, 6]. Power-to-X (P2X) technologies convert and store renewable energy in the form of chemical energy carriers (i.e., eco-friendly fuels), and studies have considered them as a key research objective [5, 7]. Green hydrogen is also a promising option, which can be a substitute for fossil fuels and store excess electricity simultaneously. Specifically, hydrogen production through the catalyst-aided electrolysis of liquid water provides a promising approach to decarbonization. However, at present, a majority of hydrogen fuel is obtained through steam reforming of natural gas, which reacts (mostly) CH_4 with water (H_2O), consequently generating carbon monoxide (CO) and CO_2 . Thus, only 4 % of hydrogen is produced through water electrolysis due to economic inefficiency [8–10].

The most industrially relevant technology is membrane-based electrolysis (e.g., alkaline electrolysis) and proton exchange membrane (PEM) electrolysis [5, 7, 11–14]. In particular, PEM electrolyzers (PEMELs) have been extensively investigated, with studies demonstrating clear advantages of high current density and voltage efficiency over alkaline electrolyzers [5, 7]. However, many as-yet unexplored questions remain to be answered before the requirements for industrial applications of PEMELs can be met.

A PEMEL consists of two electrodes (i.e., a cathode and an anode) and a polymer electrolyte membrane in between them. Water decomposes into H_2 and O_2 through an anodic oxygen evolution reaction (OER) and a counter hydrogen evolution reaction (HER) at the cathode. The sluggish OER kinetics are known as a primary bottleneck in this conversion process, since OER is a complicated multistep reaction involving a four-electron transfer [15]. Therefore, the development of high-performance OER catalysts is at the center of interest for both academia and industry. To date, only a few precious materials are known to be stable catalysts under the harsh acidic operation conditions of PEMELs. Iridium oxide (IrO_2) may be the most promising and active catalyst among them, and thus, commercialized OER catalysts mostly contain a large amount of iridium [16, 17]. Due to the open rutile structure of IrO_2 , many undercoordinated atoms are present at

its surface, providing potential catalytically active reaction sites. Despite these favorable physical and chemical properties as OER catalysts, the following critical limitation exists to iridium-based PEM stacks: Iridium is one of the rarest elements, with an abundance of approximately 0.08 ppb in the Earth’s crust and an estimated annual production of iridium metal of approximately 8 tons; therefore, PEM stacks in commercial electrolyzers are unlikely to become competitive on a large scale. Thus, lowering the price of IrO₂-based catalysts while maintaining or even improving OER activity is a key challenge for future applications on an industrial scale.

Using rutile ruthenium oxide (RuO₂) is one feasible option [16, 17]. RuO₂ exhibits even higher OER catalytic activity and is also more cost-efficient than IrO₂ [18, 19]. The only obstacle is that it dissolves faster under operation than IrO₂ due to the overoxidation of ruthenium [20]. A common approach for modulating the stability of RuO₂ without sacrificing desirable properties is to control the morphology using nanostructuring techniques, such as the reshaping of nanoparticles, formation of solid solutions or core-shell particles, and phase transformation [21–27]. Although many highly efficient morphologies have been suggested on the basis of predictive-quality first-principle calculations, the influence of dynamic working conditions on catalyst systems has scarcely been analyzed by computational chemistry.

This thesis presents the research that I have pursued throughout my PhD studies regarding two promising morphologies of RuO₂: two-dimensional RuO₂ nanosheets [1] and core-shell nanostructures [2]. First, the RuO₂ nanosheets were initially synthesized by our experimental collaborators in the group of Prof. Bettina Lotsch at the Max Planck Institute for Solid State Research in Stuttgart, Germany. Motivated by the desire to understand these nanosheets’ exceptional OER activity and stability, we conducted theoretical analysis based on density-functional theory (DFT) calculations. By varying configurations of the sheet surface and edge models, the origin of the stability and active sites were successfully determined. Specifically, the relevant OER intermediates for oxide pathways were found to be stabilized under working conditions only at the edges and defects of nanosheets. These stabilizations of intermediates further enabled the OER only at a very low theoretical overpotential, which was entirely consistent with our experimental observations.

Second, a fully theoretical study was conducted on RuO₂- and IrO₂-based core-shell catalysts. Core-shell catalysts have been widely investigated due to their high efficiency and flexibility in tuning their morphology. Previous experimental work has already demonstrated that IrO₂ may be diluted by cheaper materials, either as a solid solution or core-shell structure with maintained electrical conductivity and catalytic activity [28–31]. Another successful example is the commercial Umicore catalyst with a composite of titanium dioxide (TiO₂) and IrO₂, which is often used as a reference system for the development of novel OER catalysts [31–35]. However, they have been massively loaded composites with incoherent thick catalyst films or small nanoparticles with high surface-area supports, rather than an epitaxially grown thin shell catalyst on the core. TiO₂ exhibits a stable rutile modification, which is a significant advantage for minimizing the lattice mismatch at the interface due to relatively similar lattice constants of rutile oxides. This encouraged us to pursue epitaxial core-shell nanoparticles with thin IrO₂ or RuO₂ films encapsulating an inexpensive TiO₂ core. By analyzing adhesion, strain, and surface energies, we demonstrated that current gas-phase synthesis techniques would only be able to stabilize thin films in a few-monolayer regime at some low-index facets of TiO₂ for both IrO₂ and RuO₂. By contrast, the formation of coherent shell films should be possible under more oxidizing synthesis conditions. Most

intriguingly, our ab initio thermodynamics-based studies demonstrated that these particles exhibit increased activity and stability under OER operation conditions. Thus, we concluded that rutile $\text{IrO}_2/\text{TiO}_2$ or $\text{RuO}_2/\text{TiO}_2$ core-shell nanoparticles are a promising target for future catalyst design.

Both studies have been published in international peer-reviewed journals. This publication-based dissertation thus mainly delivers an introduction to the motivations, background, and relevant methodologies essential for understanding the details of this research. The remainder of this thesis is organized as follows: In Chapter 2, general and historical knowledge about rutile transition metal oxide catalysts and their industrial applications is introduced. In addition, I discuss the OER reaction mechanisms proposed to date, both within experiments and theory, as well as the current challenges. In Chapter 3, the known methods and techniques in computational surface science are reviewed (i.e., periodic slab approximations and ab initio thermodynamics for different environmental conditions), as well as some of my own related case studies. In Chapter 4, descriptions and the practical usage of a more state-of-the-art machine-learning interatomic potential are presented, including as-yet unpublished results of the surface structure exploration of working RuO_2 catalysts under dynamic conditions. Lastly, Chapter 5 presents the summary, conclusions, and outlook of the thesis.

2 Rutile Transition Metal Oxide Catalysts and Their Industrial Applications

The development of novel materials for catalysis in (electro)chemistry is at the center of interest for both industry and academia. Both experiments and theoretical calculations have identified some transition metal oxides (TMOs) as promising heterogeneous catalyst materials. Among them, rutile-type RuO₂ and IrO₂ have been extensively studied as highly active OER catalysts due to their desirable physical properties and chemical stability, even under harsh reaction conditions. Specifically, these rutile oxides are utilized for PEM-based water electrolysis, which is a promising alternative to conventional alkaline electrolysis for producing high-purity hydrogen [5].

Furthermore, both rutile RuO₂ and IrO₂ are highly conductive metallic oxides. RuO₂ has an experimental electrical resistivity of $35.2 \pm 0.5 \mu\Omega\text{cm}$, which is slightly higher for IrO₂ (that of RuO₂ is isotropic, whereas that of IrO₂ is anisotropic: $49.1 \pm 0.5 \mu\Omega\text{cm}$ in [001] and $34.9 \pm 1.0 \mu\Omega\text{cm}$ in [011] direction) [36]. This specialty allows both oxides to be intensively used as electrocatalysts within various electronic devices. The rutile structure of both oxides contains two formula units of MO₂ (M = Ru and Ir) in a tetragonal unit cell, where the metal atoms are centrally coordinated to six neighboring O atoms in a near-perfect (slightly distorted) MO₆ octahedral coordination [37, 38]. Two distinct types of O atoms exist in the octahedron: four basal O atoms, which have longer M-O σ bonds, and two axial O atoms, which have shorter bonds. Both oxides have a strong σ -bond character, where O 2p orbitals are hybridized with *d* (*e_g*) orbitals. In the case of RuO₂, two of the five *d* orbitals of Ru are combined with one *s* and three *p* orbitals of O to form *e_g²sp³*. The three remaining *d* (*t_{2g}*) orbitals make one σ and one π metal-metal bond along the edges of the octahedron and one weak π bond with the axial O atom. Since the *t_{2g}* bands are partially filled, the Fermi level lies within the *t_{2g}* range of the density-of-states (DOS), resulting in these oxides' metallic character [38, 39]. As an additional remark, other nanostructures of RuO₂ and IrO₂ can also exhibit metallic behavior, such as the 2D nanosheet introduced in this thesis [1].

Cherevko *et al.* compared the catalytic activity and stability of metallic iridium and ruthenium as well as their oxides and confirmed their relative stability in the order of IrO₂ > RuO₂ > Ir > Ru and activity in reverse order [40]. Consequently, IrO₂ is currently the most promising material as it is durable enough under the acidic operating conditions of PEM cells to be commercialized. However, it is costly due to the low abundance of and increasing demand for electronic devices. On the other hand, RuO₂ is cheaper and even more active than IrO₂ for acidic OER, but it dissolves upon operation unacceptably rapidly. The primary reason for its dissolution is the overoxidation of ruthenium in the catalyst, which results in soluble RuO₄ molecules [20]. The onset of Ru corrosion coincides with the onset of oxygen evolution, suggesting the build-up of higher-valence-state Ru at the catalyst-electrolyte interface within the working potential range [41, 42]. It is thus highly desirable to improve the stability of RuO₂-based catalysts without sacrificing the high

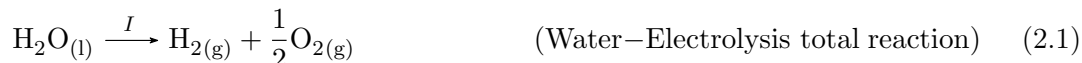
activity, ultimately substituting the rare iridium.

Morphology control is a possible approach. Experiments have indicated that nanostructured electrode materials, such as nanoparticles (NPs) or nanoflakes, significantly enhance stability. For this purpose, various synthesis techniques have been used, such as chemical vapor deposition [43], electrochemical deposition [44], and other techniques [18, 45, 46] for RuO₂, whereas solution based synthesis [47–50] and the thermal oxidation of Ir particles [18] have been successful for IrO₂. However, the catalytic activities of these synthesized oxides are often not similar due to differences in crystal structure [1, 50–52] and particle size (according to high surface-area-to-mass ratios) [47, 48, 50] among others. Neither optimal morphologies nor systematic routes for improving OER are currently known due to the lack of atomistic structural models and missing insight into microscopic mechanisms. To determine relevant factors that contribute to the efficiency of OER and predict catalyst structures with higher activity, computational simulations play a pivotal role.

In this chapter, I present a theoretical overview of the anodic oxygen evolution reaction, particularly in acidic media, with a historical research tendency in PEMELs. Suggested reaction mechanisms at the catalyst-electrolyte interface are introduced along with experimental techniques and theoretical capabilities for designing and evaluating a better catalyst.

2.1 Anodic Oxygen Evolution Reaction Catalysts in Acidic Media

The intermittent supply of renewable energy from wind and solar sources necessitates grid power storage [53, 54]. A promising option is P2X technology [5, 7], which stores excess energy in chemical bonds (e.g., H₂, NH₃, and organic fuels) through electrochemical processes. In most cases, these chemical products are obtained by a cathodic reduction reaction, which requires a counter-reaction at the anode, namely the OER in water splitting. Under the acidic conditions often used in PEMELs, the overall reaction of water splitting proceeds in two half-reactions, namely the HER at the cathode and the OER at the anode.



During the overall reaction (Eq. 2.1), the spontaneous removal of gas phase products from the liquid electrolyte shifts the equilibrium to the right according to Le Chatelier’s principle. However, the splitting of water at standard temperature and pressure is thermodynamically unfavorable due to the significant standard Gibbs free energy ΔG° of 237.24 kJ mol⁻¹ (1.23 V) as well as the thermal entropic energy $T\Delta S^\circ$ of 48.6 kJ mol⁻¹ (0.5 V). Once the aforementioned energy is applied in the form of thermoneutral cell potential (approx. 1.48 V), the electrochemical cell is kinetically controlled. In particular, low-temperature electrolyzers such as PEMELs and alkaline electrolyzers (AELs) are operated above the thermoneutral potential due to losses in ohmic resistance U_{ohm} , activation potential U_{act} , and concentration potential U_{con} . The overpotential η is the amount of the required additional potential on the thermodynamic standard cell potential of 1.23 V.

Two major technologies exist for water electrolyzers, which operate either in an acidic or an alkaline environment. Alkaline (basic) electrolyzers are well-established methods

of hydrogen production and are economically mature at a commercial level. Still, major drawbacks stem from concerns over their efficiency and safety, namely their low partial load range, limited current density, and low operating pressure [5]. In particular, hydrogen gas diffuses to the oxygen evolution chamber across the diaphragm, which reduces efficiency and increases the risk of explosion. This is especially pronounced at low loads (40 %) because the oxygen production rate drops, causing the hydrogen concentration to rise to dangerous levels (lower explosion limit > 4 mol % H_2) [55]. On the other hand, acidic electrolyzers have several advantages, including higher current densities, higher HER efficiency, and the capacity to operate under dynamic conditions [13, 56]. However, an acidic OER (presented in Eq. 2.3) requires high energy to break the strong O-H covalent bonds of H_2O , which results in more sluggish kinetics [15]. Catalysts thus play a crucial role in the acidic OER; however, they mostly require precious and rare transition metal-based catalysts (e.g., ruthenium and iridium) due to the corrosive acidic regime [5, 57, 58].

2.1.1 Proton Exchange Membrane Electrolyzer

The earliest PEMEL was developed by General Electric in the 1960s to overcome the drawbacks of alkaline electrolyzers [11, 12]. The initial performance reported in 1973 [12] was a current density of 1 A cm^{-2} at 1.88 V and 2 A cm^{-2} at 2.24 V with a cell life of 15,000 h [14]. This surpassed the efficiency of AELs, and consequently, PEMELs were developed faster, attracting broad interest from the industry.

Similar to PEM fuel cell technology, PEMELs introduce solid polysulfonated membranes such as Nafion[®] or Fumapem[®] as an electrolyte [5]. Using such polymer electrolyte membranes prevents gas crossover between the HER/OER chambers as well as ensures safe operation and a large load range [5]. It also promises to produce H_2 with high purity and allows the PEMEL to operate over a wide range of power densities (up to 4.4 mW cm^{-2}) [5, 59]. Moreover, it guarantees high proton conductivity (0.1 S cm^{-1}) compared with AELs, which use a liquid electrolyte that induces high resistance and a slow response to any power fluctuation due to inertia. In addition, functioning under a highly acidic environment ($\text{pH} \sim 2$) means that acidic electrolyzers have inherent advantages over AELs [13], such as the significantly higher electric conductivity of H_3O^+ ions ($350 \text{ S cm}^2 \text{ mol}^{-1}$) compared with OH^- ions ($198 \text{ S cm}^2 \text{ mol}^{-1}$). Consequently, a well-developed PEMEL can operate at high current densities of approximately $0.6\text{--}2.0 \text{ mA cm}^{-2}$ with low ohmic loss. Furthermore, it would have a wider operating temperature ($20\text{--}80^\circ\text{C}$) [14, 60] and low membrane thickness ($20\text{--}300 \mu\text{m}$) [5]; thus, PEMELs are economically effective due to running at a high overpotential as well as the fact that stacks can be constructed at lower cost.

The central part of a PEMEL is a stack of PEM cells, each of which consists of electrodes (a cathode and an anode) separated by a polymer electrolyte membrane (the same as a proton exchange membrane), as illustrated in Fig. 2.1. The electrodes adjoin to the membrane directly in most cell architectures to leverage the major advantages stated above due to the reduction of diffusion processes of protons toward the membrane. This membrane electrode assembly (MEA) is the core component of a PEM cell. Furthermore, gas diffusion layers (GDL), which supply electric current to and from the electrodes, are located on both sides of the MEA and are permeable to H_2/O_2 gas and liquid water. Lastly, these two half-cells are surrounded by bipolar plates, which transfer the reactant water to the MEA

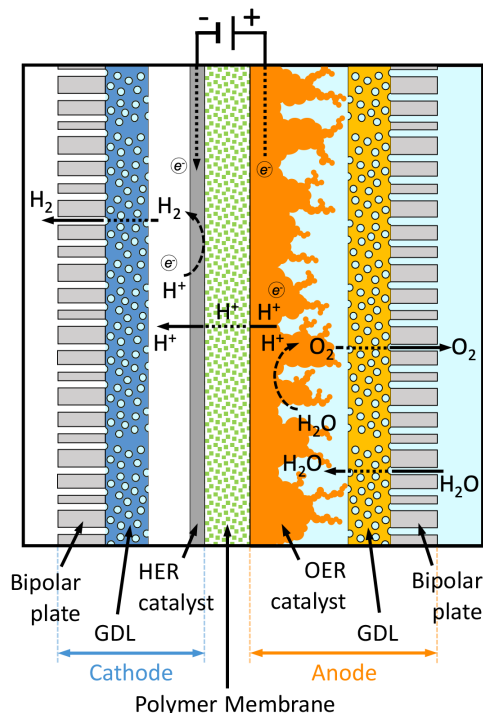


Fig. 2.1: Schematic sketch of a proton exchange membrane electrolyzer (PEMEL) stack. Both electrodes (cathode and anode) consist of a bipolar plate, a gas diffusion layer (GDL), and an HER/OER catalyst layer. The electrodes are separated by a polymer membrane electrolyte, which behaves as a selective proton transfer pathway.

interfaces and remove gas products.

A solid (polymer) electrolyte allows for a compact design of the cell system along with capable properties (e.g., high-pressure operation) [61]. This high-pressure operation has the benefit of providing hydrogen to the end user at a high electrochemical compression, which means that less energy is required for subsequent hydrogen compression and storage [61, 62]. It also enhances gas product removal through an increased rate of diffusion.

While the PEMEL operates, water molecules are supplied to the chamber adjacent to the cell and permeate through the bipolar plate and the GDL. They reach the interface between the membrane and the catalyst layer and decompose into protons, electrons, and oxygen gas molecules through the OER. The O_2 molecules diffuse back through the GDL and bipolar plate and transpire out of the water chamber. The remaining protons travel through the proton conducting membrane to the cathode side, which is the other side of the MEA, while electrons transfer from the OER catalyst to the GDL through the electric current supplied by the source. Finally, the protons and electrons recombine into H_2 gas molecules at the interface of the HER catalyst. These H_2 molecules then transfer to the hydrogen-collecting water chamber through the GDL and the bipolar plate.

A major drawback of PEMELs is the limited stability of OER catalysts. This is also problematic for AELs, but their anode materials are mostly nickel-, iron-, and cobalt-based, which are Earth-abundant and relatively stable under alkaline conditions. Nevertheless, only precious transition metal-based catalysts are sufficiently stable and active under acidic

conditions [63, 64]. (Although metallic ruthenium and iridium were recognized as OER catalysts in earlier studies, most recent studies have concluded that their oxide forms are much more stable [65, 66].) Thus, as previously mentioned, reducing the mass load of iridium in catalysts or stabilizing RuO₂-based catalysts against corrosion/dissolution is the prime challenge. Extensive research has pursued the idea of introducing other elements into the catalyst, such as making alloys or core-shell heterostructures, to reduce the commercial price and corrosion rate [2, 22, 30, 31, 33, 67–71].

2.1.2 Reaction Mechanisms in Acidic Media

Various reaction mechanisms have been proposed for OER in acidic media, especially on heterogeneous electrocatalysts, and they are listed in Table 2.1 [72, 73]. However, none of these have been completely verified based on experiments since a mechanistic understanding of the catalytic processes can only be obtained at the atomistic level of the elementary subprocesses, and consequently, it is not trivial. Instead, experimentalists have suggested kinetic models for diverse imaginable OER mechanisms and analyzed observations based on them.

Tab. 2.1: Proposed reaction mechanisms for the oxygen evolution reaction [72, 73].

Mechanism	Reaction pathways
I. Oxide path	$* + \text{H}_2\text{O} \rightarrow \text{OH}^* + \text{H}^+ + e^-$ $2\text{OH}^* \rightarrow \text{O}^* + * + \text{H}_2\text{O}$ $2\text{O}^* \rightarrow 2* + \text{O}_2$
II. Electrochemical oxide path	$* + \text{H}_2\text{O} \rightarrow \text{OH}^* + \text{H}^+ + e^-$ $\text{OH}^* \rightarrow \text{O}^* + \text{H}^+ + e^-$ $2\text{O}^* \rightarrow 2* + \text{O}_2$
III. Electrochemical metal peroxide path	$* + \text{H}_2\text{O} \rightarrow \text{OH}^* + \text{H}^+ + e^-$ $2\text{OH}^* \rightarrow \text{O}^* + * + \text{H}_2\text{O}$ $\text{O}^* + \text{H}_2\text{O} \rightarrow \text{OOH}^* + \text{H}^+ + e^-$ $2\text{OOH}^* \rightarrow \text{O}^* + * + \text{H}_2\text{O} + \text{O}_2$
IV. DFT-predicted peroxide path	$* + \text{H}_2\text{O} \rightarrow \text{OH}^* + \text{H}^+ + e^-$ $\text{OH}^* \rightarrow \text{O}^* + \text{H}^+ + e^-$ $\text{O}^* + \text{H}_2\text{O} \rightarrow \text{OOH}^* + \text{H}^+ + e^-$ $\text{OOH}^* \rightarrow * + \text{O}_2 + \text{H}^+ + e^-$

Tafel analysis is a conventional—but still the most commonly used—approach for probing electrochemical kinetics and discovering rate-determining steps (RDSs) [74–76]. Here, the Tafel equation, which is a limiting case of the Butler-Volmer equation at high overpotential $\eta > 0.1$ V, explains how the electric current through an electrode relies on the voltage differential between the electrode and the bulk electrolyte for a simple redox reaction. The full Butler-Volmer equation is as follows:

$$I = I_0 \left[\exp\left(\frac{\alpha_A z F \eta}{RT}\right) - \exp\left(-\frac{\alpha_C z F \eta}{RT}\right) \right], \quad (2.4)$$

where I is an electrode current density and I_0 is an exchange current density—the current in the absence of net electrolysis and at zero overpotential. z is the number of electrons involved in the electrode reaction, and α_A and α_C are anodic and cathodic charge transfer coefficients, respectively. Here, α_A and α_C are highly correlated as $\alpha_A + \alpha_C = 1$. Lastly, R is a universal gas constant, T is temperature, and F is the Faraday constant. Under the extreme condition of a highly positive overpotential, anodic current density dominates Eq. 2.4, and cathodic current density becomes negligible. Eq. 2.4 can be reformulated to an anodic Tafel equation as follows:

$$I = I_0 \exp\left(\frac{\alpha_A z F \eta}{RT}\right) \quad . \quad (2.5)$$

On the other hand, when the overpotential is highly negative, Eq. 2.4 becomes a cathodic Tafel equation:

$$I = -I_0 \exp\left(-\frac{\alpha_C z F \eta}{RT}\right) \quad . \quad (2.6)$$

Consequently, the applied overpotential η under these extreme cases can be written as

$$\eta = \pm b \log\left(\frac{I}{I_0}\right) = \pm \frac{RT \ln 10}{\alpha z F} \log\left(\frac{I}{I_0}\right) = \pm \frac{k_B T \ln 10}{\alpha z e} \log\left(\frac{I}{I_0}\right) \quad , \quad (2.7)$$

where b is a Tafel slope, k_B is the Boltzmann constant, and e is an elementary charge. α is the representative transfer coefficient between α_A and α_C . Therefore, the experimental Tafel slope b for each linear region can be extracted as follows [20]:

$$b = \frac{d\eta}{d \log I/I_0} = \frac{k_B T \ln 10}{\alpha z e} = \frac{k_B T \ln 10}{(\gamma + r_{\text{rds}} \alpha_{\text{rds}}) e} = \frac{59 \text{ mV/dec}}{\gamma + r_{\text{rds}} \alpha_{\text{rds}}} = \frac{59 \text{ mV/dec}}{\beta} \quad . \quad (2.8)$$

At ambient (room) temperature, $k_B T \ln 10 / e \simeq 59 \text{ mV}$. Here, $\alpha \cdot z$ in the denominator can be represented as $(\gamma + r_{\text{rds}} \alpha_{\text{rds}})$, where γ counts the number of transferred electrons from the resting state to the reaction intermediate just before the rate limiting transition state; r_{rds} denotes whether the reaction is a chemical (i.e., no charge transfer [$r_{\text{rds}} = 0$]) or an electrochemical ($r_{\text{rds}} = 1$) reaction step; and α_{rds} is the transfer coefficient of the RDS [20].

In general, a kink in the Tafel slopes is accepted as a change in the RDS. This indicates the change of the number of transferred electrons γ to the rate-limiting transition state from the resting state of the active catalyst. The conceivable OER mechanisms could be demonstrated through this kinetic analysis.

One of the earliest studies for acidic OER was performed by Bockris *et al.*, who suggested mechanisms I-III in Table 2.1 [72]. Here, * denotes an active site on the catalyst surface. In the case of $\text{RuO}_2(110)$, the Tafel analysis fits a reaction mechanism of the electrochemical oxide path with an additional rearrangement of the intermediate surface hydroxyl group (OH) [77]. Two linear Tafel lines have been found—one at potentials lower than 1.52 V, which indicates that this rearrangement of the OH step is the RDS, and the other at potentials higher than 1.52 V, which indicates that the first water oxidation step is the RDS. Although this OER mechanism is solely proposed based on Tafel slopes, a real RDS cannot be determined unambiguously because different mechanisms can yield similar Tafel slopes [72].

According to the electrochemical oxide path, a water molecule is first adsorbed at the active site, generating an adsorbate of OH species, a proton, and an electron. As stated above, the first adsorbed OH species exists as an intermediate surface complex that undergoes some additional rearrangement before further oxidation [77]. The OH* then repels an additional proton and electron through a deprotonation step by the positively charged electrode under reaction conditions. Lastly, the remaining oxygen adsorbates O* combine to produce O₂ gas molecules and empty active sites (*).

Within the computational approach, extensive attention has been concentrated on revealing the potential-determining step (PDS) since 2005 [73, 78]. The focus is on the thermodynamics of the OER process and the relative stabilities of intermediate species under reaction conditions. For a given reaction mechanism, ab initio calculations make it possible to quantify the Gibbs free energy difference ΔG of each elementary subprocess as a function of applied potential U . The PDS is then assigned to the subprocess, which possesses the largest ΔG for the two connected intermediate species. It also yields the minimum required applied bias voltage, which results in all subprocesses being downhill.

In the pioneering research of Rossmeisl *et al.*, their thermodynamic analysis allowed them to first understand the dehydrogenation of RuO₂(110) at high potentials, where the resting state of the active catalyst is oxygen-covered. In addition, they established that the oxygen binding energy and the binding energy of two other intermediate species (OH and OOH) are correlated by scaling relations. Based on such relations, a volcano plot can be derived, which illustrates the OER activity of a catalyst as a function of only the O binding energy. This volcano plot has led to numerous related studies [2, 79–83].

Rossmeisl *et al.* also proposed the DFT-predicted peroxide path, listed in Table 2.1 IV [73]. Here, the first and second steps are identical to the electrochemical oxide path. However, the authors claimed that an additional water molecule may combine with O* at the third step and produce surface hydroperoxo (OOH*) and a set of a proton and an electron. This is undoubtedly acceptable since OOH* has a higher oxidation state than O* and could be preferable in such highly oxidative working conditions [84]. Lastly, OOH* dissolves into an O₂ molecule, a proton, and an electron. The DFT peroxide pathway consequently involves a four-electron transfer and is a much more complicated multistep reaction.

However, authors have overlooked that the desorption of O₂ (OOH* \rightarrow * + O₂ + H⁺ + e⁻) could require high energy. Binniger *et al.* recently demonstrated that the activation energy of the conventional O₂ evolution step through desorption is 0.95 eV at IrO₂(110), which is significant and not negligible [85]. They suggested a novel step of O₂ evolution by adjacent *OO–OO* association (*OO + *OO \rightarrow *O + *O + O₂), which only requires an activation energy of 0.34 eV. This novel OER mechanism is much more favorable than the conventional DFT-peroxide path at any potential. At 1.53 V vs NHE in particular, all steps of the novel mechanism become downhill in their calculations, while the conventional O₂ evolution is still considerably endergonic by 0.46 eV. This also explains the high activity and substantial stability of crystalline IrO₂, since the breaking of any Ir-O bonds is not involved in the OER process.

The aforementioned studies have revealed active sites on rutile-type RuO₂ and IrO₂ catalysts. Specifically, a coordinatively unsaturated (cus) metal site exposed on the surface is catalytically active, as verified in a series of later experiments [27, 84, 86, 87]. The detailed atomic structures and surface adsorption sites are discussed in Section 2.2.

These computational techniques—so-called *ab initio* thermodynamics [37, 88] and the computational hydrogen electrode (CHE) approach [73, 78, 89]—efficiently and effectively allow one to understand microscopic insights and thermodynamic overviews of a specific reaction mechanism; however, drawbacks apparently exist. For example, they rely on the hypothesized conceivable reaction mechanisms analogous to Tafel analysis and the targeted surfaces [20, 90]. In addition, they neglect any kinetic contributions. The Brønsted-Evans-Polanyi (BEP) principle indirectly bypasses the actual activation energy, as that between two reactions of the same family is proportional to the difference of their enthalpy of reaction, and Sabatier’s principle can bridge between thermodynamics and kinetics; nevertheless, the actual activity does not always follow the thermodynamic results. Lastly, simulating realistic solid-liquid interfaces is extremely demanding; instead, most studies involve approximated solid-vacuum interfaces, which might have significant differences depending on systems [91–93].

Several solutions have been proposed for investigating kinetic barriers and reaction rates, such as nudged elastic band (NEB) methods and microkinetic simulations [88, 94, 95]. For instance, Ping *et al.* calculated the kinetic barriers for the OER on the IrO₂(110) surface at constant potential conditions [80]. The computed Tafel slope and overpotentials correlated well with their experimental measurements, and they confirmed that thermodynamically favorable reaction steps are not always kinetically favorable. In the case of RuO₂, Dickens *et al.* used the climbing image NEB and found that the O-O bond formation at the third step in Table 2.1 IV for generating hydroperoxo is rate-limiting [96]. A new kinetic activity volcano plot was suggested based on their results with a microkinetic model, which was in good agreement with experimental observations.

Although such kinetic investigations have been successful in many cases, they are computationally demanding and often challenging to use to find global minimum transition states. Thus, various studies have been attempted to avoid the complicated transition state theory [97–99]. The recently introduced scheme of the electron step symmetry index (ESSI) descriptor is one strategy for incorporating thermodynamic and kinetic factors. This is because it includes an experimental input parameter in the scheme with the same computational costs as thermodynamic calculations, providing improved results in the screening of potential electrode materials [97, 100]. Exner also used the concept of $G_{\max}(\eta)$, which involves all free energy changes in the reaction pathway, to compute Tafel slopes as a function of applied bias and the location of kinks [101].

Furthermore, the electrostatic contributions to solid-liquid interfaces are approximately accounted for by implicit solvation models, such as the Poisson-Boltzmann description of solvent and ion distribution [93, 102]. These models, however, treat charges unphysically close to the surface and the dielectric constant drops stiffly at the interface. More crucially, the possibly larger energetic stabilizations of adsorbates from solvation effects are residual for the OER due to strong hydrogen bonds between water molecules and surface adsorbates, such as OH and OOH [103]. In the case of IrO₂(110), a water bilayer causes a decrease in $\Delta G_{\text{O}} - \Delta G_{\text{OH}}$ by 0.2 eV, whereas $\Delta G_{\text{OOH}} - \Delta G_{\text{OH}}$ causes an increase of 0.2 eV [104]. A study also found that the amount of binding energy changes is negligible for all OER intermediate adsorbates besides OOH*, which decreased by 0.4 eV with explicit water molecules [92]. The aforementioned studies have indicated the still elusive influence of solvation effects on the surfaces of transition metal oxides.

Most studies have been conducted primarily on the (110) surface for both RuO₂ and IrO₂

[20, 73, 80, 91, 92, 96, 105–107], since it is the most stable facet under synthesis conditions [108, 109]. However, the PEMEL works at high cell voltages to reach industrially viable current densities, and catalysts are suspected of transforming into environment-specific favorable morphologies. Opalka *et al.* found the Wulff shape of IrO₂ nanoparticles in the onset potential range through ab initio thermodynamics [83]. The most stable IrO₂(110) at the open circuit potential became thermodynamically less stable than other low-index facets, such as (111), as the potential increased. At the OER onset, the Wulff crystal reshaped into a (111) mono-faceted particle. We confirmed the same feature for RuO₂ in our previous publication [2]. This finding is intriguing since activities are not only material system-dependent but also surface orientation-specific [27, 86, 110]. Stoerzinger *et al.* reported that RuO₂(100) and (101) surfaces were more active for the OER than their (110) and (111) counterparts, where the density and electronic structure of undercoordinated Ru atoms strongly correlated with the actual activity [27, 86]. Moreover, Roy *et al.* reported a correlation between the activity and density of Ru_{cus}-O bonds [110].

In Chapter 3, more detailed theoretical approaches are introduced that were used in our studies to investigate catalyst surfaces along with case studies from independent research conducted for this thesis. Before moving on, a special note for RuO₂ as a CO oxidation catalyst is presented in the next section.

2.2 Note for RuO₂: CO Oxidation Catalyst

The oxidation of carbon monoxide (CO) at the surfaces of heterogeneous catalysts is one of the most quintessential catalytic reactions, as it has paved the way for an enhanced understanding of heterogeneous catalysis at the microscopic level [111, 112]. At the surface of late transition metal catalysts, such as Rh, Pd, Pt, or Ag, it simply involves chemisorbed CO and dissociatively adsorbed O, such as $\text{CO}^* + 1/2\text{O}^* \rightarrow \text{CO}_{2(\text{g})}$ through the Langmuir-Hinshelwood (LH) mechanism. Likewise, the catalyzed CO oxidation is less complicated as well as straightforward to explore through ab initio calculations. In particular, CO oxidation on RuO₂ has been extensively studied for the past few decades both through experiments and theory due to its high activity [113–136].

Work on supported catalysts by Cant *et al.* first sparked a focus on CO oxidation over Ru [137]. At the time, Ru(0001) was generally recognized as a poor catalyst under ultra-high vacuum (UHV) conditions [138], becoming an active catalyst only under oxidizing conditions [139, 140]. This large discrepancy was resolved in the early 2000s through the observation of the formation of a thin RuO₂ film under actual reaction conditions [113, 141]. After applying the technique of low energy electron diffraction (LEED), Kim *et al.* noticed the existence of RuO₂(110) domains at the catalytically active oxygen-rich Ru(0001) surface [113]. In 2002, DFT calculations by Reuter *et al.* identified that a high concentration of surface oxygen beyond 1.5 ML causes the formation of a metastable O-Ru-O trilayer, which eventually unfolds into rutile RuO₂(110) once a certain thickness is achieved [142].

Follow-up theoretical investigations on RuO₂(110), such as ab initio thermodynamics [120, 121] and the kinetic Monte Carlo (kMC) [124, 127], have enabled the understanding of relative stabilities among surfaces with different CO/O coverages as well as turnover frequencies (TOFs) for CO oxidation. There are two preferred adsorption sites on the O-poor (110) surface, as indicated in the left panel in Fig. 2.2, namely the cus and bridge (br) sites.

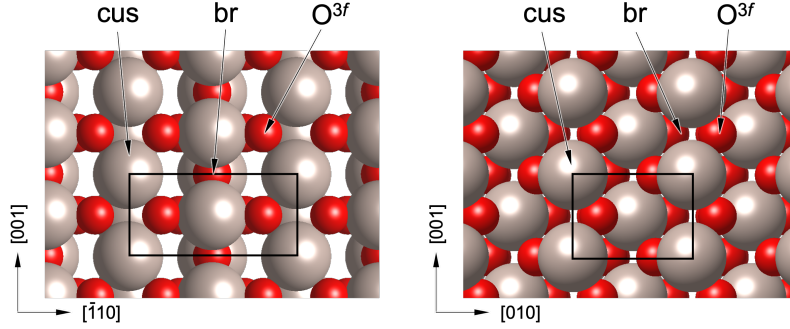


Fig. 2.2: Top views of O-poor $\text{RuO}_2(110)$ (left) and $\text{RuO}_2(100)$ surfaces (right). Representative adsorption sites are notated as coordinatively unsaturated (*cus*), bridge (*br*), and threefold coordinated lattice oxygen (O^{3f}). Grey and red spheres indicate ruthenium and oxygen atoms, respectively, and each primitive surface unit cell is indicated by the black rectangle.

Oxygen atoms preferably occupy all bridge sites first, which yields a stoichiometric surface, followed by *cus* sites, leading to O-rich termination. Stoichiometric termination is obtained experimentally from the annealing process in UHV, while slow quenching in the oxygen environment results in O-rich termination [120, 121, 143].

Similar to transition metal catalysts, the competitive adsorption and desorption of O and CO decide the catalytic activity of the RuO_2 surface. The fully coordinated lattice O^{3f} is not involved in the catalytic reaction since it is strongly bound and hardly desorbed. Thus, the majority of the CO_2 yield relies on the LH mechanism between the chemisorbed CO and O at the *cus* and bridge sites.

Ab initio calculations confirmed that the lateral interactions between adsorbates are relatively small as the variations in the binding energies are within ± 150 meV due to the open crystal structure of $\text{RuO}_2(110)$ [127]. The resulting binding energies of O_{cus} , O_{br} , CO_{cus} , and CO_{br} are approximately -1.0 , -2.3 , -1.3 , and -1.6 eV, respectively. In detail, oxygen binds much more strongly to bridge sites than *cus* sites, whereas CO binds to *cus* and bridge sites at a rather similar strength. These binding features imply the barriers to CO oxidation, in which reactants with multiple binding sites are involved; the resulting barriers, including the strongly bound O_{br} , are higher— $E_{\text{O}_{\text{br}}+\text{CO}_{\text{br}}}^{\text{barrier}} = 1.5$ eV and $E_{\text{O}_{\text{br}}+\text{CO}_{\text{cus}}}^{\text{barrier}} = 1.3$ eV, while those involving O_{cus} are smaller— $E_{\text{O}_{\text{cus}}+\text{CO}_{\text{br}}}^{\text{barrier}} = 0.8$ eV and $E_{\text{O}_{\text{cus}}+\text{CO}_{\text{cus}}}^{\text{barrier}} = 0.9$ eV.

As previously mentioned, most research has focused on the (110) surface, which is known as the most stable among all five low-index facets under experimental conditions [20]. This is true under the experimental synthesis condition of 1 atm and 1073 K suggested by Rosenthal *et al.* [144, 145], and the Wulff shape of a nanoparticle seems to (110) dominate [108]. Under the more oxidative synthesis condition of 0.1 atm and 573 K suggested by Narkhede *et al.* [146], however, the majority of nanoparticles become $\text{RuO}_2(111)$ [108]. Likewise, the discovery of novel surface motifs is critical to understanding the working state of heterogeneous catalysts under dynamic conditions, and alternative reaction mechanisms on different surface orientations should not be overlooked.

Regarding this argument, a longstanding puzzle on RuO_2 surfaces is the unknown $c(2 \times 2)$ reconstruction, which was first observed in 2005 by Ałman *et al.* [126]. They measured the CO conversion over oxidized polycrystalline RuO_2 with differing temperatures in a stepwise

variation. The conversion was only rapid in the first cycle, followed by a dramatic decrease in the second. There was no such phenomenon with prereduced RuO_2 , which presented a maximum conversion efficiency of approximately 60 % at 453 K. This finding is contrary to the general knowledge of ruthenium catalysts, in which the oxidized surface is more active. Scanning tunneling microscopy (STM) images detected a rough RuO_2 film on $\text{Ru}(0001)$ after treatment under oxidizing conditions, and these microfacets caused the deactivation of the catalyst. The microfacets were disclosed as the combination of $\text{RuO}_2(100)$ with the inactive $c(2 \times 2)$ regions. The atomic structure of the $c(2 \times 2)$ reconstruction remains elusive and the origin of inactivity is hidden. Very recently, Hess *et al.* suggested a potential $c(2 \times 2)$ geometry, which has a lower surface free energy; however, the theoretical LEED-I(V) analysis did not fit perfectly with their experiments [147].

In Section 3.3.2, I discuss unpublished results on activity loss at the suggested $c(2 \times 2)$ surface with various feasible reaction pathways and activation barriers obtained from NEB calculations.

3 Computational Surface Science

To find and design more effective catalysts, a mechanistic understanding of the target chemical systems is critical. Thus, it is necessary to determine all of the elementary processes that constitute the catalytic cycle at the atomistic level, which is an extremely demanding task. A possible solution is to simplify the problem and obtain this knowledge for model catalysts first, such as single crystalline structures and well-defined facets [148]. Although this hides many real-world problems, it represents the only way to start a theoretical analysis.

In this respect, the first-principles approach has become one of the most potent and standardized tools for effectively exploring surfaces and interfaces and examining catalytic chemical reactions, particularly on heterogeneous catalysts [149]. Whereas most experiments employ the top-down approach as the analyses and characterizations follow the observations (i.e., microscopy and spectroscopy), first-principles-based calculations follow a bottom-up strategy. Therefore, complementing observations with modern computational theory has resulted in numerous synergistic effects in many fields of materials science and chemistry [81]. These include conventional calculations, such as thermodynamic stability, spectroscopy, and activity descriptors, as well as state-of-the-art theoretical approaches, such as first-principles kinetic models and in situ simulations [88, 89, 94, 150–154].

To understand heterogeneous catalysis, it is first pivotal to construct the surface structure and composition of the working catalyst under the given reaction conditions in the form of the reactant partial pressure p_i and temperature T . Both thermodynamics and statistical mechanics based on electronic structure calculations contribute to achieving this. One powerful approach that has been well established for the former aspect and generalized for studies on catalyst surfaces is ab initio thermodynamics [37, 88, 152]. It provides information on the surface structure and energetics as a function of the effective concentration of reactants under p_i and T scales. Ab initio thermodynamics represents a general concept for extending the DFT results, as a zero p and T technique, to situations under a finite p and T . Thus, one can use first-principles-based potential energy surface (PES) information to calculate suitable thermodynamic quantities, such as the Gibbs free energy [155]. The theory has several approximations to cover using more accurate methods. It is thus computationally efficient and more relevant to examine complex surfaces and screen a large number of surfaces. Another explicit limitation is that the surface structural candidates must be sampled using specific rules and chemical intuition. Infinite possibilities may exist depending on how high-index orientations and how large supercells one would explore. Moreover, there could be unexpected reconstructions, which have hardly been addressed through DFT geometry optimization for constrained unit cell structures in most studies—they are often overlooked. These shortcomings, however, can be mitigated by combining the technique with other techniques, such as global optimization algorithms, grand canonical sampling, and machine-learning (ML) potentials [156–162].

In this chapter, I introduce the theory and methodology of ab initio thermodynamics

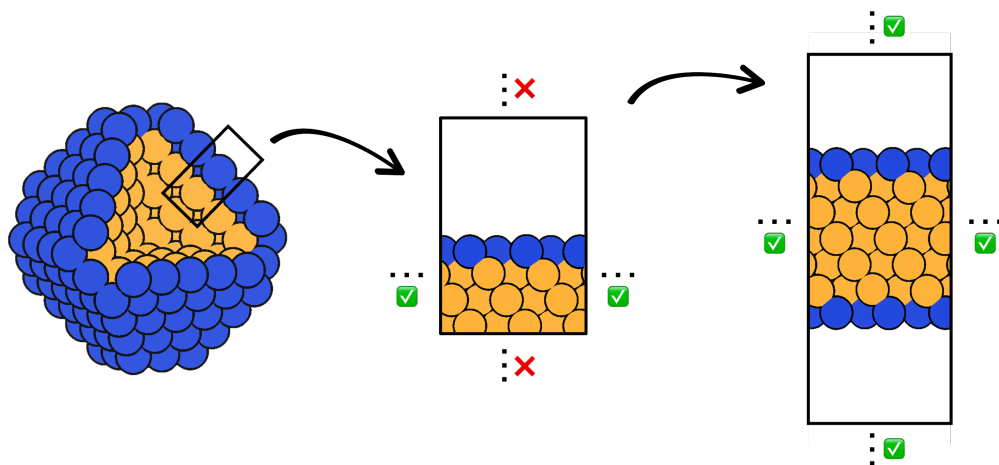


Fig. 3.1: Schematic description of the implementation of a slab model. A simplified nanoparticle model (left) leads to a surface model, which is periodic in lateral directions but not perpendicular and hard to be employed within periodic DFT calculations (middle). An alternative two-dimensional slab model (a symmetric slab) achieves periodicity in all directions (right).

and its implementation for practical use in application to heterogeneous catalysis with some examples. The chapter contains results that I obtained, not only from the two main publications that this thesis is based on but also from others, including both published and unpublished results.

3.1 Periodic Slabs and Approximations

An ideal surface in a microscopic view is (semi-)infinite in the two dimensions but finite along the direction perpendicular to the plane, as depicted in the middle panel of Fig. 3.1. Thus, in first-principles calculations, periodic boundary conditions are beneficial in two dimensions but not in the other. To overcome this limitation, an alternative model can be adopted, for which the supercell along the vertical direction (the direction perpendicular to the surface) contains multiple atomic and vacuum layers to prevent interactions between repeating images in the same direction. This specific model is called a slab model since the two-dimensional slabs are stacked along the surface normal direction, separated by a vacuum. A schematic of the basic idea is presented in Fig. 3.1. To achieve a sufficient level of approximation, each slab should be thick enough to decouple its two surfaces. In addition, the central region of the slab must mimic the perfect bulk crystal so that the surface reconstruction is entirely screened out before reaching the bulk-like region. However, no values have been stipulated for the thickness of the slab or vacuum layer; rather, they are system- and surface-dependent. The total energy and forces of the slab should be tested for convergence with respect to those thicknesses to achieve convincing calculation results.

Based on these methodological foundations, the bulk crystal is truncated along the facet orientations with specific terminations, generating an arbitrary number of unique

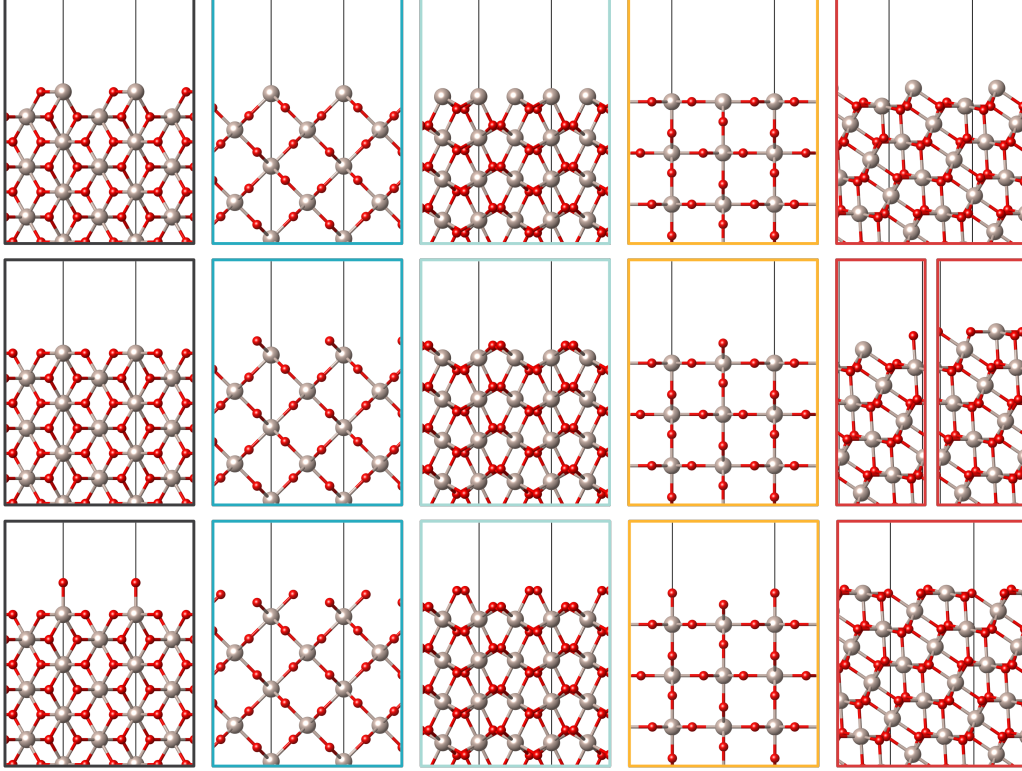


Fig. 3.2: Side views of 16 bulk-truncated surface structures for rutile RuO_2 . Other rutile oxides are analogous (from left to right): (001) , $(010)/(100)$, $(011)/(101)$, (110) , and (111) facets; and (from top to bottom): metal-rich, stoichiometric, and O-rich terminations. There are two stoichiometric surfaces for (111) orientation. Ruthenium and oxygen atoms are depicted as grey and red spheres, respectively.

surfaces. A group of lattice planes is established by three integers (hkl) , which are called Miller indices [163]. Miller indices determine the vector perpendicular to the lattice plane $g_{(hkl)} = h\alpha + k\beta + l\gamma$, where α , β , and γ are coefficients on the basis of the reciprocal lattice vectors \vec{a} , \vec{b} , and \vec{c} , respectively. In the case of pure RuO_2 (as for IrO_2), rutile is the unique stable bulk phase; consequently, it has a tetragonal symmetry of $\vec{a} = (a, 0, 0)$, $\vec{b} = (0, a, 0)$ and $\vec{c} = (0, 0, c)$. Therefore, it takes five symmetry-inequivalent low-index orientations, namely (001) , $(100)/(010)$, $(011)/(101)$, (110) , and (111) [108]. Based on the chemical environment, terminations of these surfaces are determined by thermodynamic driving forces to the equilibrium, such as a preferred oxygen coverage at a given oxygen partial pressure. It is critical to define both orientations and terminations of surfaces of heterogeneous catalysts because they uniquely determine the electronic structure of adsorption sites, which is critical for activity and selectivity. For instance, the surface morphology of rutile structures exposes many undercoordinated transition metal atoms at the catalyst-electrolyte interface, which become critical reactive sites in the water oxidation mechanism [16]. Since an infinite number of possible terminations exist depending on the size of the surface unit cell, the adsorption sites, and the adsorption pattern, simulating them all is impractical and they should be thinned out systematically. As an example, all possible (1×1) terminations for

each orientation are illustrated in Fig. 3.2 by truncating the crystal stacking at different planes. In the case of (001) surfaces, such bulk truncation only allows one stoichiometric surface. Additional terminations are thus generated by removing an oxygen atom from or adding one to the previous or next atomic layer, respectively.

A surface is created by cutting the bulk crystal (i.e., breaking the chemical bonds in a specific plane), which of course involves energy consumption if the system (surface and surrounding atmosphere) is single-component (note that a possibility exists of negative surface energy in multicomponent systems, but it is not germane in this basic concept for understanding surface free energy [164]). The energy required to create each peculiar surface from the stable bulk crystal is defined as Gibbs surface free energy. In principle, the morphology of nanoparticles is determined by thermodynamics to minimize the sum of surface free energies for all exposed facets (also corners and edges). Thus, the ideal equilibrium shape of a crystal should follow that of the Wulff crystal, which has the minimum surface energy for the fixed volume inside [165].

Low-index surfaces, which are lower in surface free energy than higher index orientations in most cases, are exclusively considered in this thesis [166, 167]. When a plane (hkl) is cleaved, the broken and unbroken bonds at the surface are established by the normal vector of the plane and each bond vector [168, 169]. Consequently, a higher atomic density at low-index surfaces results in lower surface free energy, whereas high-index surfaces exhibit higher surface energy.

As briefly mentioned, the catalytic activity strongly correlates with the surface atomic arrangement and configuration of the catalysts. Higher-index facets of catalysts can have more step edges and kinks, with sites exhibiting enhanced activity [166, 167, 170]. However, it is extremely difficult to control the morphology of nanoparticles to expose the surfaces due to the high surface energy in general. While particles are growing, they disappear due to the thermodynamic preference for reducing the surface energy [166]. High-index facets are only available when the energetic contributions from edges and corners are no longer negligible and the Gibbs-Wulff theorem cannot be satisfied. Thus, sufficiently small nanoparticles can expose those facets on their surface [171, 172]. As Su *et al.* claimed, DFT calculations have determined high-index facets of RuO₂, such as (210) and (211), with higher relative surface free energy compared with other low-index surfaces by 18-76 % [167]. Thus, high-index surfaces are not discussed in this thesis.

3.2 *Ab Initio Thermodynamics*

Assuming that the system follows the microcanonical ensemble, the total energy E^{tot} is dependent on the number of each species in the system and their particular configurations. This enables a comparison of the stability of two different configurations using the DFT total energies if both have the exact same number of atoms for each species. However, it is often necessary to compare the stability of surface systems with different numbers of species, since the surface composition varies in the context of the surrounding atmosphere. In the case of the surface of rutile RuO₂, the surface coverage of oxygen changes with varying oxygen partial pressure, and one must compare the relative stability of configurations with different oxygen coverages to determine which coverage occurs at a given pressure. Thus, one must quantify the energetic contribution from the differences in species between two

configurations depending on the effective concentration of each species in the surrounding atmosphere.

Therefore, the basic idea is to obtain this information from the concept of atomic reservoirs, with which species are exchanged in thermodynamic equilibrium [88]. Heterogeneous catalysts operate under given temperatures T and reactant partial pressures p_i , for which the appropriate thermodynamic measure is Gibbs free energy. To assess the relative stability of surfaces with a certain Miller index (hkl) and a termination σ in thermodynamic equilibrium, the surface free energy $\gamma_{\text{surf}}^{(hkl),\sigma}$ can be calculated as a function of chemical potentials of atomic reservoirs as follows:

$$\gamma_{\text{surf}}^{(hkl),\sigma}(T, p_i) = \frac{1}{A^{(hkl)}} \left[G_{\text{surf}}^{(hkl),\sigma}(T, p_i, \nu_i^{(hkl),\sigma}) - \sum_i \nu_i^{(hkl),\sigma} \mu_i(T, p_i) \right] , \quad (3.1)$$

where $G_{\text{surf}}^{(hkl),\sigma}$ is the Gibbs free energy of a given surface with surface area $A^{(hkl)}$, and $\nu_i^{(hkl),\sigma}$ and μ_i are the number of atoms and the chemical potential of the corresponding reservoirs of species i present in the system, respectively. This can be simply interpreted as the Gibbs free energy of the entire system, composed of the contribution of the bulk phase of the solid, gas phase of the surrounding atmosphere, and interface between the two phases:

$$G_{\text{sys}} = G_{\text{bulk}} + G_{\text{gas}} + G_{\text{surf}} \quad . \quad (3.2)$$

By calculating $\gamma_{\text{surf}}(T, p_i)$ for conceivable surface configurations, the one with the lowest surface energy would be the most stable surface at the given temperature and pressure and be observed experimentally in equilibrium.

3.2.1 Surface Free Energy in Gaseous Environments

As an example of RuO_2 , bulk rutile RuO_2 is considered a thermodynamic reservoir, with which the surface is equilibrated in the presence of macroscopic quantities of RuO_2 . At ambient temperatures, this assumption constrains the chemical potentials of ruthenium μ_{Ru} and oxygen μ_{O} to the Gibbs free energy (per formula unit) $G_{\text{RuO}_2,\text{bulk}}$ of RuO_2 as follows:

$$G_{\text{RuO}_2,\text{bulk}} = \mu_{\text{Ru}} + 2\mu_{\text{O}} \quad . \quad (3.3)$$

In equilibrium with the oxygen environment, Eq. 3.1 can be reformulated to define the surface free energy as a function of the chemical potential of the gas phase reservoir μ_{O} :

$$\gamma_{\text{surf}}^{(hkl),\sigma} = \frac{1}{A^{(hkl)}} \left[G_{\text{surf}}^{(hkl),\sigma} - \nu_{\text{Ru}}^{(hkl),\sigma} G_{\text{RuO}_2,\text{bulk}} - \left(\nu_{\text{O}}^{(hkl),\sigma} - 2\nu_{\text{Ru}}^{(hkl),\sigma} \right) \mu_{\text{O}} \right] \quad . \quad (3.4)$$

If the surface is stoichiometric, i.e. $\nu_{\text{O}}^{(hkl),\sigma} = 2\nu_{\text{Ru}}^{(hkl),\sigma}$, Eq. 3.4 is simplified to

$$\gamma_{\text{surf}}^{(hkl),\sigma} = \frac{1}{A^{(hkl)}} \left[G_{\text{surf}}^{(hkl),\sigma} - \nu_{\text{Ru}}^{(hkl),\sigma} G_{\text{RuO}_2,\text{bulk}} \right] \quad . \quad (3.5)$$

This indicates that the surface energy of the stoichiometric surface is independent of the oxygen chemical potential. The surface energy from sub- or superstoichiometric surfaces would have a slope of $-\left(\nu_{\text{O}}^{(hkl),\sigma} - 2\nu_{\text{Ru}}^{(hkl),\sigma} \right) / A^{(hkl)}$ for varying μ_{O} .

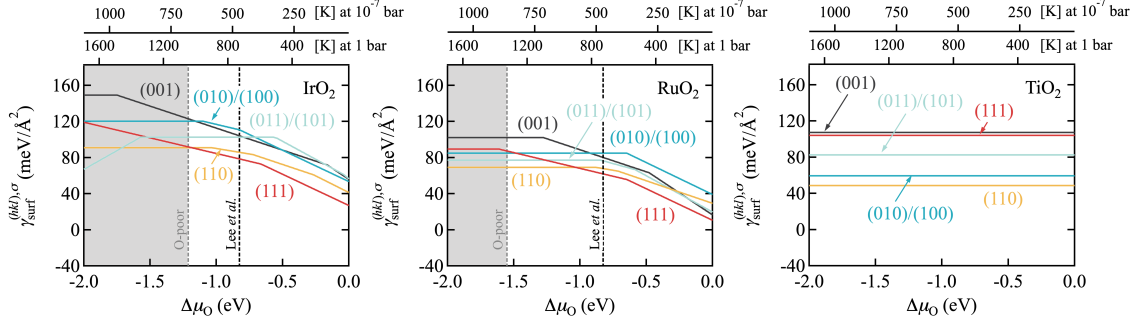


Fig. 3.3: Computed surface free energies $\gamma_{\text{surf}}^{(hkl),\sigma}$ of the five low-index facets of rutile IrO_2 , RuO_2 , and TiO_2 in an oxygen environment. Kinks in the individual lines indicate a change of the most stable termination σ , generally from O-poor terminations (positive slope with respect to the oxygen chemical potential $\Delta\mu_{\text{O}}$) over stoichiometric terminations (horizontal lines) to O-rich terminations (negative slope) [108, 162, 173]. The vertical gray dotted lines indicate the thermodynamic bulk oxide stability (O-poor limit) as computed from the bulk heat of formation (the limit is -3.76 eV outside of the depicted range for TiO_2). Along the top x axis, the dependence on $\Delta\mu_{\text{O}}$ is translated into a temperature scale at different oxygen pressures. The black vertical dotted line in the phase diagram for IrO_2 and RuO_2 represent the synthesis conditions employed by Lee et al. [18]. Color codes for different surface orientations correspond to those of Fig. 3.2. Reproduced from reference [2] under CC-BY.

In most experiments, the oxygen partial pressure p_{O_2} and temperature T are usually varied. Thus, it is both crucial and useful to understand which values μ_{O} can take. When μ_{O} becomes too low (i.e., all oxygen preferably leaves the oxide sample), the oxide may decompose into the bulk metal and oxygen gas, which can be represented as

$$\mu_{\text{O}}^{\min} \rightarrow \mu_{\text{Ru}}^{\max} = G_{\text{Ru,bulk}} \quad , \quad (3.6)$$

where $G_{\text{Ru,bulk}}$ is the Gibbs free energy of Ru in the bulk phase (here in a hexagonal closed-packed [HCP] system) per formula unit. From Eq. 3.3, the lowest limit of μ_{O}^{\min} at $T = 0$ K and $p_{\text{O}_2} = 0$ atm thus becomes

$$\mu_{\text{O}}^{\min} = \frac{1}{2} \left[G_{\text{RuO}_2,\text{bulk}} - G_{\text{Ru,bulk}} \right] \quad . \quad (3.7)$$

This is called the chemical potential of the oxygen-lean limit (or the metal-rich limit). On the other hand, oxygen atoms maximally accumulate on the oxide surface under oxygen-rich conditions, and one can define μ_{O}^{\max} as the chemical potential of pure O_2 approximately as follows [121]:

$$\mu_{\text{O}}^{\max} = \frac{1}{2} E_{\text{O}_2} \quad , \quad (3.8)$$

Therefore, the theoretical boundaries of μ_{O} can be written as follows:

$$\frac{1}{2} \left[G_{\text{RuO}_2,\text{bulk}} - G_{\text{Ru,bulk}} \right] < \mu_{\text{O}} < \frac{1}{2} E_{\text{O}_2} \quad . \quad (3.9)$$

Here, the definition of the Gibbs free energy of formation is introduced as $\Delta G_{\text{RuO}_2}^f = G_{\text{RuO}_2, \text{bulk}} - G_{\text{Ru}, \text{bulk}} - E_{\text{O}_2}$, and Eq. 3.9 reformulates to

$$\frac{1}{2}\Delta G_{\text{RuO}_2}^f < \Delta\mu_{\text{O}} < 0 \quad , \quad (3.10)$$

where $\Delta\mu_{\text{O}} = \mu_{\text{O}} - \frac{1}{2}E_{\text{O}_2}$. With this, the surface free energy from Eq. 3.4 is finally given as a linear function of the chemical potential change $\Delta\mu_{\text{O}}$:

$$\gamma_{\text{surf}}^{(hkl), \sigma} = \frac{1}{A^{(hkl)}} \left[G_{\text{surf}}^{(hkl), \sigma} - \nu_{\text{Ru}}^{(hkl), \sigma} G_{\text{RuO}_2, \text{bulk}} - \left(\nu_{\text{O}}^{(hkl), \sigma} - 2\nu_{\text{Ru}}^{(hkl), \sigma} \right) \left(\Delta\mu_{\text{O}} + \frac{1}{2}E_{\text{O}_2} \right) \right] \quad . \quad (3.11)$$

Now, the relative chemical potential of oxygen, $\Delta\mu_{\text{O}} = \Delta\mu_{\text{O}}(T, p_{\text{O}_2})$, summarizes the dependence of the surface free energy on temperature T and oxygen pressure p_{O_2} [37]. In detail, $\Delta\mu_{\text{O}}(T, p_{\text{O}_2})$, assumed to be an ideal gas-like reservoir, is expressed as follows:

$$\Delta\mu_{\text{O}}(T, p_{\text{O}_2}) = \mu_{\text{O}}(T, p_{\text{O}_2}) - \frac{1}{2}E_{\text{O}_2} = \frac{1}{2} \left[\tilde{\mu}_{\text{O}_2}(T, p^\circ) + k_{\text{B}}T \ln \left(\frac{p_{\text{O}_2}}{p^\circ} \right) \right] \quad . \quad (3.12)$$

The temperature-dependent chemical potential $\tilde{\mu}_{\text{O}_2}(T, p^\circ)$ at the standard state pressure p° is taken from reported experimental values [174]. The zero-point energy (ZPE) of molecular oxygen $E_{\text{O}_2}^{\text{ZPE}}$ is obtained from experimental data and reference tables and considered as $E_{\text{O}_2} = E_{\text{O}_2}^{\text{DFT}} + E_{\text{O}_2}^{\text{ZPE}}$ [175, 176].

The overall formalism, as described above, is based on the Gibbs free energy of the system, while the obtained energies from DFT calculations are total (internal) energies. Both quantities are highly correlated, but DFT total energies neglect the vibrational free energy, configurational free energy, and pV term. In general, the Gibbs free energy can be written as follows:

$$G = E^{\text{total}} + F^{\text{vib}} + F^{\text{conf}} + pV \quad , \quad (3.13)$$

where E^{total} is the DFT total energy, F^{vib} is the vibrational free energy, and F^{conf} is the configurational free energy.

The vibrational free energy F^{vib} can be obtained from integrating over the phonon DOS $\sigma(\omega)$ instead of the sum of discrete fundamental modes ω_i as follows:

$$F^{\text{vib}} = \int d\omega F^{\text{vib}}(T, \omega) \sigma(\omega) \quad , \quad (3.14)$$

where

$$F^{\text{vib}}(T, \omega) = \frac{\hbar\omega}{2} + k_{\text{B}}T \left(1 - \exp \left(\frac{\hbar\omega}{k_{\text{B}}T} \right) \right) \quad . \quad (3.15)$$

From an earlier study on RuO_2 [37], the vibrational contribution to the change in Gibbs free energy stays within $\pm 10 \text{ meV}/\text{\AA}^2$, which is certainly not negligible but does not affect

the physical analysis in the present cases. Thus, in this thesis, it is approximated by the difference of the corresponding ZPE-corrected total energy contributions [177].

The configurational entropy contribution per surface area is given by the following equation:

$$\frac{TS^{\text{conf}}}{NA_{\text{site}}} = \frac{k_{\text{B}}T}{NA_{\text{site}}} \ln \frac{(N+n)!}{N!n!} , \quad (3.16)$$

where S^{conf} is the configuration entropy, N is the total number of surface sites, n is the small number of defect or adsorbate sites ($n \ll N$), and A_{site} is the surface area per site. For $\text{RuO}_2(110)$, a study found that the configurational contribution to the surface free energy is less than $5 \text{ meV}/\text{\AA}^2$ for any $T < 1000 \text{ K}$, which is negligible [121].

Lastly, a simple dimensional analysis provides hints about the contribution of the pV term to the surface free energy as $pV/A^{(hkl)} = \text{atm } \text{\AA}^3/\text{\AA}^2 \simeq 10^{-3} \text{ meV}/\text{\AA}^2$ [152]. This is clearly negligible even up to the high partial pressure of 1000 atm , where it is less than $\sim 0.1 \text{ meV}/\text{\AA}^2$.

Therefore, in this thesis, Eq. 3.4 is approximated by the ZPE-corrected DFT total energies as follows:

$$\gamma_{\text{surf}}^{(hkl),\sigma} = \frac{1}{A^{(hkl)}} \left[E_{\text{surf}}^{(hkl),\sigma} - \nu_{\text{Ru}}^{(hkl),\sigma} E_{\text{RuO}_2,\text{bulk}} - \left(\nu_{\text{O}}^{(hkl),\sigma} - 2\nu_{\text{Ru}}^{(hkl),\sigma} \right) \mu_{\text{O}} \right] . \quad (3.17)$$

Fig. 3.3 illustrates calculated surface free energies $\gamma_{\text{surf}}^{(hkl),\sigma}$ as a function of oxygen chemical potential change for the rutile transition metal oxides IrO_2 , RuO_2 , and TiO_2 [2]. This already provides abundant information. In the case of TiO_2 , surface energies for all five low-index facets are represented by horizontal lines in the range of relevant $\Delta\mu_{\text{O}}$, which means that stoichiometric surfaces always dominate. The Wulff shape of rutile TiO_2 is thus highly stable and consistent in the large temperature and oxygen partial pressure ranges. On the other hand, IrO_2 and RuO_2 exhibit a similar trend, where O-rich terminations become more stable under oxygen-rich conditions for all low-index orientations. Therefore, the corresponding morphology of nanoparticles under different temperatures and pressures would change since the gradients of surface free energy are different for the various orientations and terminations.

If another influential (i.e., chemisorbing or reacting) gas exists, the change of oxygen chemical potential $\Delta\mu_{\text{O}}$ is not the only variable for $\gamma_{\text{surf}}^{(hkl),\sigma}$. As discussed in Chapter 2, RuO_2 is a highly active catalyst for the CO oxidation reaction, and both O_2 and CO would coexist under the reaction conditions. Consequently, Eq. 3.1 is reformulated to demonstrate the surface free energy as a function of the chemical potentials of two gas phase reservoirs μ_{O} and μ_{CO} :

$$\begin{aligned} \gamma_{\text{surf}}^{(hkl),\sigma} = & \frac{1}{A^{(hkl)}} \left[G_{\text{surf}}^{(hkl),\sigma} - \nu_{\text{Ru}}^{(hkl),\sigma} G_{\text{RuO}_2,\text{bulk}} \right] \\ & - \frac{1}{A^{(hkl)}} \left[\left(\nu_{\text{O}}^{(hkl),\sigma} - \nu_{\text{CO}}^{(hkl),\sigma} - 2\nu_{\text{Ru}}^{(hkl),\sigma} \right) \mu_{\text{O}} + \nu_{\text{CO}}^{(hkl),\sigma} \mu_{\text{CO}} \right] . \end{aligned} \quad (3.18)$$

Analogous to μ_{O} , the value for the CO chemical potential μ_{CO} at $T = 0 \text{ K}$ is the total energy of the isolated CO molecule E_{CO} . Therefore, it can be defined as $\Delta\mu_{\text{CO}} = \mu_{\text{CO}} - E_{\text{CO}}$.

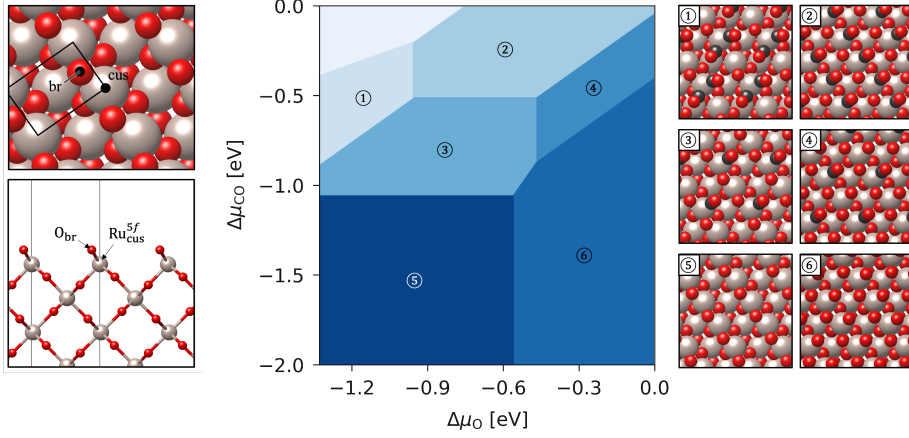


Fig. 3.4: Left panel: Top (top left) and side (bottom left) views of the stoichiometric $p(1 \times 1)$ - $\text{RuO}_2(100)$ surface are illustrated. Grey and red spheres indicate ruthenium and oxygen atoms, respectively, and the periodic boundary condition for the supercell is indicated by the black rectangle. In a $p(1 \times 1)$ cell, the stoichiometric surface has one coordinatively unsaturated (*cus*) site on top of a five-fold coordinated Ru atom ($\text{Ru}_{\text{cus}}^{5f}$), as well as one bridge (*br*) site occupied by the bridge oxygen (O_{br}). Middle panel: Surface phase diagram for $\text{RuO}_2(100)$ for different terminations and coverages of CO and O. Right panel: Top views of each corresponding surface with numbering.

Following Eq. 3.12, $\Delta\mu_{\text{CO}}$ can be finally represented as the temperature and CO partial pressure dependent function as follows:

$$\Delta\mu_{\text{CO}}(T, p_{\text{CO}}) = \mu_{\text{CO}}(T, p_{\text{CO}}) - E_{\text{CO}} = \tilde{\mu}_{\text{CO}}(T, p^\circ) + k_{\text{B}}T \ln \left(\frac{p_{\text{CO}}}{p^\circ} \right) . \quad (3.19)$$

Combining Eqs. 3.18, 3.12, and 3.19 finally yields the surface free energy:

$$\begin{aligned} \gamma_{\text{surf}}^{(hkl),\sigma} &= \frac{1}{A^{(hkl)}} \left[G_{\text{surf}}^{(hkl),\sigma} - \nu_{\text{Ru}}^{(hkl),\sigma} G_{\text{RuO}_2,\text{bulk}} \right] \\ &\quad - \frac{1}{A^{(hkl)}} \left[\left(\nu_{\text{O}}^{(hkl),\sigma} - \nu_{\text{CO}}^{(hkl),\sigma} - 2\nu_{\text{Ru}}^{(hkl),\sigma} \right) \left(\Delta\mu_{\text{O}} + \frac{1}{2}E_{\text{O}_2} \right) \right] \\ &\quad - \frac{1}{A^{(hkl)}} \left[\nu_{\text{CO}}^{(hkl),\sigma} (\Delta\mu_{\text{CO}} + E_{\text{CO}}) \right] . \end{aligned} \quad (3.20)$$

Eq. 3.20 allows a three-dimensional surface phase diagram to be plotted, as depicted in Fig. 3.4. Surface free energies for different coverages of O and CO adsorbates on the $\text{RuO}_2(100)$ surface are calculated, and each corresponding surface is presented as a two-dimensional face. In this figure, only the lowest energy surfaces are depicted. Clearly, at the low chemical potential of CO, oxygen-covered surfaces (configurations 5 and 6 in Fig. 3.4) are the most favorable. For instance, at $\Delta\mu_{\text{CO}} = -1.5$ eV, either the stoichiometric or O-rich $\text{RuO}_2(100)$ surface is exposed as $\Delta\mu_{\text{O}}$ changes. On the other hand, at $\Delta\mu_{\text{CO}} = -0.5$ eV, both O and CO competitively adsorb on the adsorption sites. At a very low oxygen chemical potential, two CO molecules occupy one br and one cus site, whereas only one oxygen atom is found at the other br site. When $-1.0 < \Delta\mu_{\text{O}} < -0.5$, structures 2 and 3 may coexist,

where all bridge sites are occupied by O atoms and 50 % or all cus sites by CO molecules. If one increases $\Delta\mu_{\text{O}}$ above -0.5 eV, both O and CO occupy cus sites, which are finally fully covered by oxygen at $\Delta\mu_{\text{O}} > -0.1$ eV.

Notably, $c(2 \times 2)$ -RuO₂(100) reconstructions are not included in the phase diagram. As mentioned, they could not be obtained from the simple DFT geometry optimization due to an inaccurate initial guess, which resulted in local optimization and trapping to the PES local minima. To overcome this, we developed a new workflow to efficiently train a ML interatomic potential, which is a highly flexible and accurate surrogate PES model for ab initio reference data [162]. The searching/sampling processes and results are discussed in the next chapter (Chapter 4) in detail. This discussion includes a brief introduction to Gaussian process regression (GPR), descriptors for the representation of atomic structures, hyperparameter selection, and on-the-fly generation of the ML potential using the surface exploration process.

3.2.2 Surface Free Energy in Aqueous Environments

If the catalyst is in contact with a solution (water), then the chemical reservoir of oxygen is no longer the gas phase oxygen but rather liquid water. Thus, Eq. 3.1 can be written as follows:

$$\begin{aligned} \gamma_{\text{surf}}^{(hkl),\sigma} = & \frac{1}{A^{(hkl)}} \left[G_{\text{surf}}^{(hkl),\sigma} - \nu_{\text{Ru}}^{(hkl),\sigma} G_{\text{RuO}_2,\text{bulk}} \right] \\ & - \frac{1}{A^{(hkl)}} \left[\left(\nu_{\text{O}}^{(hkl),\sigma} - 2\nu_{\text{Ru}}^{(hkl),\sigma} \right) \mu_{\text{H}_2\text{O}} \right] \\ & - \frac{1}{A^{(hkl)}} \left[\left\{ \nu_{\text{H}}^{(hkl),\sigma} - \left(\nu_{\text{O}}^{(hkl),\sigma} - 2\nu_{\text{Ru}}^{(hkl),\sigma} \right) \right\} \left(\mu_{\text{H}^+}^{\text{aq}} + \mu_{e^-} \right) \right] , \end{aligned} \quad (3.21)$$

where liquid H₂O is now the reservoir for oxygen species, and the remaining hydrogens are referenced to sets of one proton and one electron.

Although ab initio thermodynamics can efficiently describe the surface phase diagram in gaseous conditions, as described in Section 3.2.1, describing the surface (interface) of working electrocatalysts in contact with liquid electrolytes is difficult. Specifically, it is extremely challenging to perform an explicit calculation of a solvated proton $\mu_{\text{H}^+}^{\text{aq}}$ and electron μ_{e^-} , as indicated in Eq. 3.21. To avoid this, Nørskov *et al.* proposed the computational hydrogen electrode (CHE) model, which correlates the sum of $\left(\mu_{\text{H}^+}^{\text{aq}} + \mu_{e^-} \right)$ with the applied potential U [89]. Within the CHE model, the chemical potential for $(\text{H}^+ + e^-)$ in solution is related to that of $\frac{1}{2}\text{H}_2$ in the gas phase by designating the reference potential to the standard hydrogen electrode. Under standard conditions (298.15 K, 1 bar, pH 0), the reaction free energy ΔG of $\frac{1}{2}\text{H}_2 \rightarrow \text{H}^+ + e^-$ is zero. Thus, under an applied potential U , it can be obtained as follows:

$$\mu_{\text{H}^+}^{\text{aq}} + \mu_{e^-} = \mu_{\text{H}_2}^{\text{gas}}(298.15 \text{ K}, 1 \text{ bar}, 0 \text{ pH}) + eU \quad . \quad (3.22)$$

The $\mu_{\text{H}_2}^{\text{gas}}$ term is then computed using the sum of a ZPE-corrected DFT total energy of an isolated hydrogen molecule E_{H_2} and the energetic contribution from the temperature and pressure effect under standard conditions. The chemical potential of liquid water is

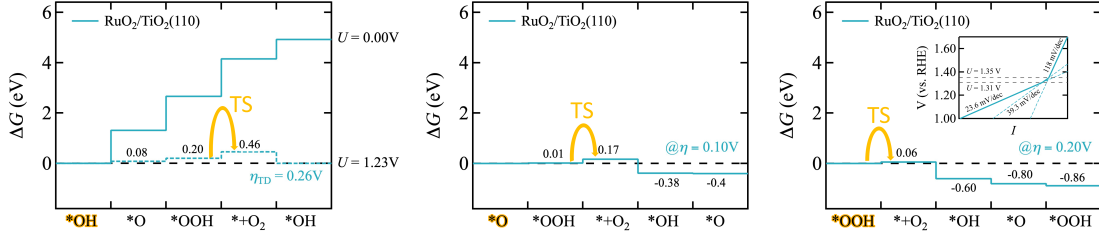


Fig. 3.5: Gibbs free energy change profile ΔG for the oxygen evolution reaction at $\text{RuO}_2/\text{TiO}_2(110)$ after renumbering the electron-transfer steps at $U=1.23$ V ($\eta=0.00$ V; left panel), $U=1.33$ V ($\eta=0.10$ V; middle panel), and $U=1.43$ V ($\eta=0.20$ V; right panel). The ΔG for each reaction intermediate and the thermodynamic overpotential η_{TD} are stated. The catalyst resting states are highlighted in the label of the x-axis as $^*\text{OH}$, $^*\text{O}$, and $^*\text{OOH}$, respectively. The corresponding Tafel slopes (inset of right panel) change three times from 23.6 to 39.3 to 118 mV/dec, and two kinks occur at $U=1.31$ and $U=1.35$ V, respectively. Reproduced from reference [2], under CC-BY.

similarly determined as the sum of a ZPE-corrected $E_{\text{H}_2\text{O}}$, the entropic contribution for a water gas molecule, and the Gibbs free energy difference between water in the gas and liquid phases under standard conditions (heat of vaporization) $\Delta G_{\text{vap}}^\circ$ (≈ 0.09 eV). The following free energy contributions were obtained from empirical thermochemical data [178].

$$\mu_{\text{H}_2}^{\text{gas}} = E_{\text{H}_2} - TS \quad (3.23)$$

$$\mu_{\text{H}_2\text{O}} = E_{\text{H}_2\text{O}} - \Delta G_{\text{vap}}^\circ - TS \quad (3.24)$$

Then, the surface free energy is represented solely as a function of applied potential U . Here, U refers to a reversible hydrogen electrode (RHE), a subtype of the standard hydrogen electrodes that implicitly account for the pH dependence. The last missing component is the effect of acidity on the surface free energy due to the concentration of protons in electrolytes. This term in CHE is taken as $\Delta G_{\text{pH}} = k_{\text{B}}T \cdot [\text{pH}] \cdot \ln 10$ and added to the surface free energy. It allows one to construct a theoretical Pourbaix diagram that depicts the most stable surface phases depending on pH and applied potential U (vs. 1 RHE). In this thesis, however, I assume that the acidic OER occurs under very low and constant pH conditions ($\text{pH} \approx 0$), and thus, this term is neglected.

3.3 Case Studies

3.3.1 OER and Tafel Slope at Core-Shell Surfaces

Based on the concepts presented in the previous section, one can directly calculate the reaction free energy of each elementary step in Table 2.1 (IV; page 9) by comparing the Gibbs free energies of reactants and products. For an ideal catalyst, the reaction free energy of each step becomes 1.23 eV, which is the standard electrode potential of water electrolysis, where the total free energy difference of the four-electron process is 4.92 eV. Realistic catalysts require larger reaction free energies for some steps and lower ones for others, leading to a higher minimum applied potential $U_{\text{min}} > 1.23$ V to make all steps exergonic.

The difference between U_{\min} and the ideal potential of 1.23 eV is called a thermodynamic overpotential η_{TD} .

For example, the Gibbs free energy profile ΔG is illustrated in the left panel of Fig. 3.5 for the OER at the RuO₂/TiO₂(110) core-shell surface [2]. Here, the steplike profile (solid line) depicts the complete reaction energetics at an open-circuit voltage (OCV) where $U = 0$ V. The dashed line represents the same pathway at the ideal potential. The reaction cycle is set to start from the OH adsorbed surface. In many past studies [73, 79, 90, 92, 179], the OER peroxide pathway has been considered to be initiated from the catalytically active site (*) without any adsorbates. However, the most stable intermediate termination varies at the given applied bias, and the OER should be initiated from that intermediate, which is called the catalyst resting state. For the core-shell surfaces, the most stable surface configuration at $U = 1.23$ V is the OH-covered surface; thus, it becomes the resting state. As a result, the PDS of the entire reaction is the third—the oxygen evolution step—and the thermodynamic overpotential η_{TD} is 0.26 V in our results, as presented in Fig. 3.5. As mentioned in Section 2.1.2, the PDS (thermodynamics) is not guaranteed to be identical to the RDS (kinetics), and further employing kinetic calculations is inevitable for achieving more accurate descriptions. This problem is, however, circumvented by assuming that it follows the BEP relation here, and the PDS is temporarily considered as a step where the highest transition state (TS) is located.

To obtain insights into kinetic descriptors without further demanding calculations, the theoretical Tafel slope is computed through renumbering the electron-transfer steps [101]. The transfer coefficient α_{rds} in Eq. 2.8 ranges from 0.20 to 0.76 in experiments, and it is presumed to be 0.5 here [101, 106]. Consequently, at the overpotential $\eta = 0$ V, the highest TS is after the second electron transfer step, and the corresponding Tafel slope is computed at approximately 23.6 mV/dec using Eq. 2.8. When the η is higher than 0.08 V, the resting state switches from the OH to the O-covered surface, which again requires the steps to be renumbered. The middle panel of Fig. 3.5 illustrates the Gibbs free energy profile at $\eta = 0.10$ V and the shift of the highest TS to after the first electron transfer step. When η is increased to > 0.12 V, the resting state finally changes from the O- to the OOH-covered surface, as illustrated in the right panel of Fig. 3.5. Along with these TS shifts, the Tafel slope increases stepwise from 23.6 to 39.3 to 118 mV/dec (see the inset of Fig. 3.5).

The full background, motivations, and results regarding the acidic OER on RuO₂, IrO₂, and core-shell surfaces are described and discussed in detail in my previous publication [2].

3.3.2 CO Oxidation at $c(2 \times 2)$ -RuO₂(100) Reconstruction

As briefly introduced above, we developed a new workflow for efficiently training a ML interatomic potential, which allowed us to determine the unknown global minimum surface structures during on-the-fly generation of the potential [162]. Many possible $c(2 \times 2)$ -RuO₂(100) candidates have emerged from the training protocol, many of which have lower surface energies than the conventional $p(1 \times 1)$ surfaces. This subsection introduces the adsorption behavior of O and CO at one of the most plausible $c(2 \times 2)$ candidates to rationalize why it loses catalytic activity for CO oxidation. The entire training/search procedure is discussed later in Section 4.4.

The detailed atomic configuration of the candidate is depicted in the left panel of Fig. 3.6. In a primitive $(\sqrt{2} \times \sqrt{2})R45^\circ$ cell, there are two surface Ru atoms. Prior to the

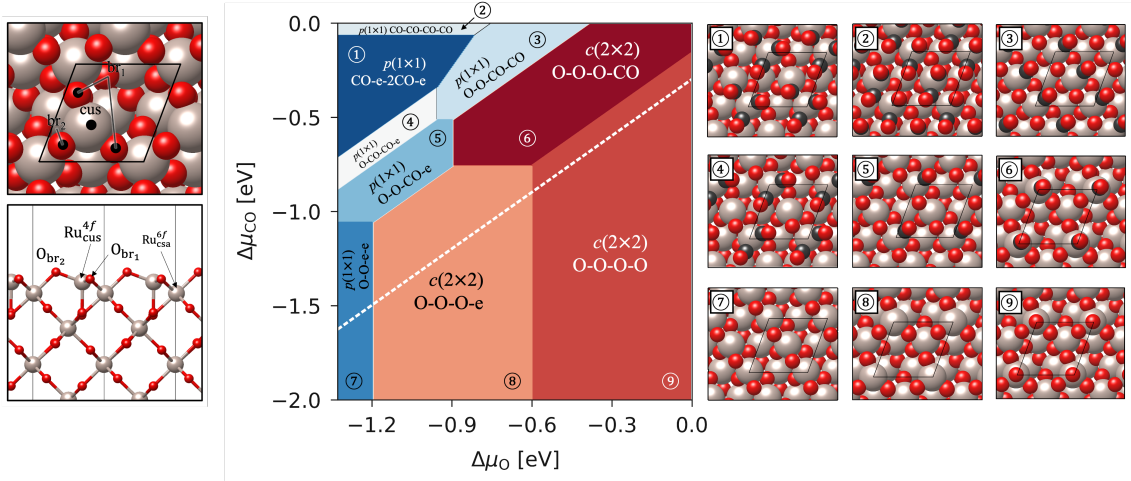


Fig. 3.6: This figure is the same as Fig. 3.4, except now it includes $c(2 \times 2)$ reconstructions. Left panel: Top (top left) and side (bottom left) views of oxygen-rich $c(2 \times 2)$ - $\text{RuO}_2(100)$ surface are illustrated. One cus site atop of a four-fold Ru atom ($\text{Ru}_{\text{cus}}^{4f}$) is depicted along with three bridge sites, where two of them are symmetry inequivalent (denoted as br_1 and br_2) in a $(\sqrt{2} \times \sqrt{2})R45^\circ$ cell. Similar to $p(1 \times 1)$, oxygen atoms in prior occupy all bridge sites (O_{br_1} and O_{br_2}). Middle panel: A full surface phase diagram of $\text{RuO}_2(100)$. The numbering and nomenclature for surface configurations are denoted. In detail, the occupation of two bridge and cus sites is listed for the $p(1 \times 1)$ surface (in $(\sqrt{2} \times \sqrt{2})R45^\circ$ supercell); for example, $p(1 \times 1)$ O-O-CO-e indicates that two bridge sites are occupied by oxygen atoms, one of two cus sites by CO, and the last cus is empty (e). In the case of $c(2 \times 2)$ reconstruction, three bridge sites (two symmetry equivalent br_1 sites are depicted first, followed by br_2) and one cus site are listed, respectively. The white dashed line indicates the stability limit of bulk RuO_2 with respect to CO-induced decomposition; in the upper left part above this line, RuO_2 is only metastable. Right panel: Top views of the total nine corresponding surface structures.

reconstruction, the oxygen coverage θ is 0.75 (O_{br} and one O_{cus} within a $(\sqrt{2} \times \sqrt{2})R45^\circ$ cell). This results in one of two Ru atoms becoming a six-fold coordinatively saturated (csa) $\text{Ru}_{\text{csa}}^{6f}$ atom, which maintains a bulk-like octahedron, while the other Ru atom is a five-fold cus $\text{Ru}_{\text{cus}}^{5f}$. Intriguingly, during the $c(2 \times 2)$ reconstruction, the $\text{Ru}_{\text{cus}}^{5f}$ creates an additional bond with the topmost oxygen atom of $\text{Ru}_{\text{csa}}^{6f}$ by simultaneously losing two subsurface Ru-O bonds. It thus transforms into a four-fold tetragonal $\text{Ru}_{\text{cus}}^{4f}$, which is elevated by 0.73 Å compared with $\text{Ru}_{\text{csa}}^{6f}$ in the (100) direction. The transformation subsequently produces three surface bridge oxygens: two are symmetry inequivalent (two O_{br_1}) and one is O_{br_2} (see Fig. 3.6). The tetragonal RuO_4 -like surface motif is known to be an extremely stable feature under oxidative conditions [180], which makes the $c(2 \times 2)$ reconstruction energetically favorable. This reconstruction results in only half the density of Ru_{cus} compared with the $p(1 \times 1)$ surface. The distance between adjacent Ru_{cus} sites is therefore significantly longer at 5.53 Å, which should inhibit LH-type CO oxidation. When an additional oxygen binds to the top of the $\text{Ru}_{\text{cus}}^{4f}$ site, the oxygen draws out the Ru atom to maintain the four-fold coordination, as opposed to becoming a five-fold geometry. Nonetheless, the oxygen binding energy at the Ru cus site is $E_{\text{O}_{\text{cus}}}^{\text{bind}} = -0.60$ eV (with all three bridge sites occupied by

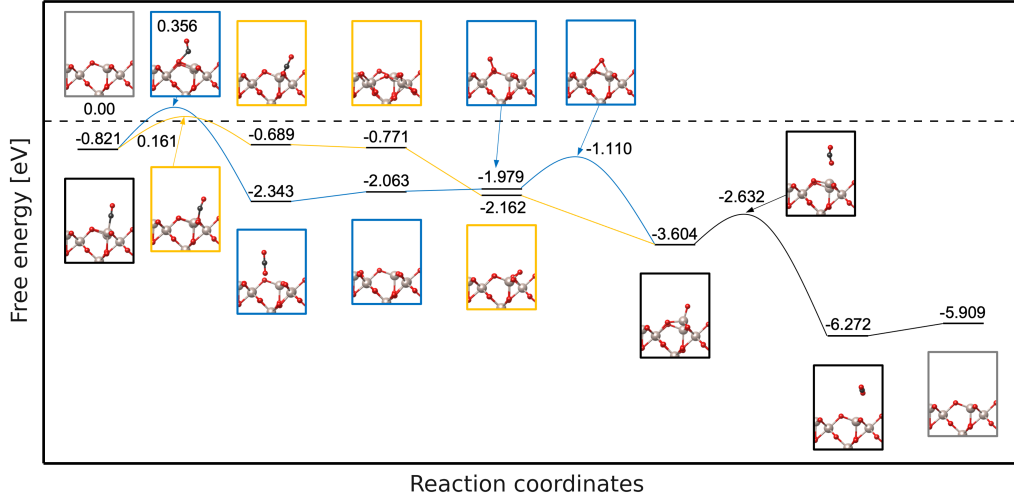


Fig. 3.7: Calculated potential energy profile for CO oxidation on the $c(2 \times 2)$ - $\text{RuO}_2(100)$ surface. The first CO molecule adsorbed at the $\text{Ru}_{\text{cus}}^{\text{Af}}$ site can combine with either O_{br1} or O_{br2} . The two different pathways are depicted in yellow and blue, respectively.

oxygen atoms), which is close to that of -0.55 eV on the $p(1 \times 1)$ within our computational settings.

Based on this $c(2 \times 2)$ structure, all possible combinations and coverages of O and CO adsorbates are generated and optimized through DFT calculations. Similar to Fig. 3.4, the resulting 2D surface phase diagram is presented in the middle panel of Fig. 3.6, which presents the final results, including both $p(1 \times 1)$ and $c(2 \times 2)$ surfaces. Since RuO_2 can be reduced by not only low oxygen chemical potentials but also carbon monoxide [121], the stability limit is depicted as a white dashed line. In a pure CO environment, RuO_2 is only stable under the condition of $G_{\text{RuO}_2, \text{bulk}} + 2\mu_{\text{CO}} < G_{\text{Ru}, \text{bulk}} + 2\mu_{\text{CO}_2}$. This can be written as follows:

$$\Delta\mu_{\text{CO}} \leq -\frac{1}{2} \left[G_{\text{RuO}_2, \text{bulk}} - G_{\text{Ru}, \text{bulk}} - E_{\text{O}_2} \right] - \frac{1}{2} E_{\text{O}_2} - E_{\text{CO}} + E_{\text{CO}_2} \quad . \quad (3.25)$$

Therefore, RuO_2 is only metastable in the upper-left part above the stability line. Intriguingly, this indicates that $c(2 \times 2)$ surfaces are the most stable for a vast range of chemical potentials (see the reddish areas in the phase diagram). This correlates well with experiments that have observed the evolution of $c(2 \times 2)$ under oxidative conditions [122, 126]. Specifically, the reconstruction already occurs at $\Delta\mu_{\text{O}} = -1.2$ eV from the $p(1 \times 1)$ stoichiometric to the $c(2 \times 2)$ O-rich surface under CO lean conditions. Other $p(1 \times 1)$ surfaces may be found at higher CO partial pressure, but only through kinetic hindrance. Therefore, the most relevant structures would be three $c(2 \times 2)$ structures—namely O-O-O-e, O-O-O-O, and O-O-O-CO.

Additionally, I investigated the kinetic barriers of possible reaction pathways for CO oxidation. The activation energies of intermediate reaction steps were calculated with the ML-accelerated NEB method AIDNEB [181–183], which drastically reduces the computational cost of highly demanding NEB calculations within DFT. The barriers were computed with a maximum uncertainty of the surrogate model of 0.02 eV until the convergence of

forces on the climbing image dropped below $0.03 \text{ eV}/\text{\AA}$. As expected, the LH-type reaction $\text{CO}_{\text{cus}} + \text{O}_{\text{cus}} \rightarrow \text{CO}_{2,\text{cus}}$ indicated an exceptionally high activation barrier of 3.96 eV . Oxygen diffusion to the adjacent cus site is unfavorable due to strong binding with bridge oxygens in the diffusion pathway. For the same reason, dissociative oxygen adsorption cannot occur on two adjacent cus sites. This only allows the initial adsorption of a CO molecule at the $\text{Ru}_{\text{cus}}^{4f}$ site since the O_2 molecule is weakly bound to the cus site. The first CO oxidation could occur within the regime of a Mars-van Krevelen (MvK) mechanism as $\text{CO}_{\text{cus}} + \text{O}_{\text{br}} \rightarrow \text{CO}_{2,\text{br}}$. Due to two inequivalent bridge oxygens, two possible MvK CO oxidation pathways exist. First, combining CO with $\text{O}_{\text{br}1}$ (yellow lines in Fig. 3.7) yields a relatively low reaction barrier of 0.98 eV , which is comparable to that on a $\text{RuO}_2(110)$ surface [127]. This step is slightly endergonic by 0.13 eV ; however, the following CO_2 desorption and barrierless dissociative O_2 adsorption at br_1 are spontaneous. Second, CO combined with $\text{O}_{\text{br}2}$ (blue lines in Fig. 3.7) is strongly exergonic by -1.52 eV but has a higher activation barrier of 1.18 eV . The consumption of $\text{O}_{\text{br}2}$ also causes partial reconstruction back to stoichiometric $p(1 \times 1)$. Thus, the following dissociative O_2 adsorption has a barrier of 0.87 eV . Both pathways result in an oxygen superrich surface, which is $c(2 \times 2)$ O-O-O-O in the phase diagram. Since the LH mechanism is inaccessible, the cus oxygen on top should be consumed by a different mechanism (i.e., the Eley-Rideal [ER] mechanism). The calculated barrier for the ER process is 0.96 eV , which is comparable to MvK processes. These results imply that the $c(2 \times 2)$ - $\text{RuO}_2(100)$ can be active for CO oxidation, but only within a narrow chemical potentials range, where all three phases of $c(2 \times 2)$ O-O-O-e, O-O-O-O, and O-O-O-CO coexist (roughly $\Delta\mu_{\text{O}} \simeq -0.60 \text{ eV}$ and $\Delta\mu_{\text{CO}} \simeq -0.75 \text{ eV}$). In addition, the whole model for adsorption underlying the approach of Reuter *et al.* is not yet considered here [127]. Sticking coefficients are required to determine the adsorption rate constants given by the fraction of all impinging molecules that eventually adsorb at the corresponding sites.

4 Machine-Learning Gaussian Approximation Potentials

Machine-learning interatomic potentials have recently evolved as a powerful class of surrogate models for computationally demanding first-principles calculations [173, 184–192]. They have facilitated large advances for the modeling and simulation of materials at a large scale with significantly reduced computational costs compared with first-principles calculations. Although classical force fields with a fixed functional form are more cost-efficient, ML potentials are fully flexible with a comparable cost and can be improved by the addition of more training data [193]. This versatility of well-trained ML potentials bridges the gap between accuracy and computational cost and allows multiscale modeling. This not only applies to larger length scales but also enables an excessive speed-up at a fixed scale, allowing for improved sampling, among other advantages.

ML potentials reproduce target properties y as \tilde{y} , which is a function of input features ξ , by optimizing parameters to minimize a loss function l , such as the sum of squared error (SSE) loss function:

$$l = \sum_N |y_N - \tilde{y}(\xi_N)|^2 \quad , \quad (4.1)$$

where N is a set of structures included in the training data. Here, \tilde{y} is determined by which ML potential model is chosen, and the computational price of the model depends on its flexibility [161]. ML potential models can be categorized by way of regression, ordered by their flexibility as follows: linear regression < polynomial regression < kernel regression < deep learning methods [160]. Less flexible models require less data and are more robust to overfitting, but they require outstanding descriptors and have limited accuracy. On the other hand, more flexible models can learn good features with optimal accuracy; however, a more extensive database is mandatory, and the models often suffer overfitting. The most successful methods in computational chemistry are based on either a Gaussian process regression (GPR) or an artificial neural network [194–201].

In this thesis, the Gaussian approximation potential (GAP) framework is used as one of the GPR schemes for generating ML-based interatomic potentials [160, 184, 202]. Along with structure exploration techniques, it enables us to examine the potential energy surface of interest with a hitherto unforeseen combination of physical accuracy and computational efficiency. It also allows us to achieve global surface structure determination for increasingly complex systems. This further facilitates the discovery of novel surface motifs, which are critical for understanding the living state of heterogeneous catalysts under dynamic conditions. In our previous study, this versatility was leveraged using a general and data-efficient iterative training protocol that allows the on-the-fly generation of GAPs through the surface exploration process [162]. This identifies plenty of unknown low-energy terminations of RuO₂, even within the restricted subspace of (1 × 1) surfaces. Moreover,

by extending it to larger supercells, new surface structures have been discovered, such as $c(2 \times 2)$ reconstructions, providing solutions to longstanding questions regarding RuO₂ catalysts.

In this chapter, I introduce the basic formalism underlying the GPR/GAP method, how the GAP model handles descriptors and representations of chemical spaces, and an outline of the hyperparameter selection. Lastly, an on-the-fly training workflow of a RuO₂ GAP and surface exploration results are presented.

4.1 Gaussian Process Regression

In practice, the GPR is a nonparametric, Bayesian regression tool that is advantageous for interpolating between data points in a high-dimensional space [202, 203]. Since GPR is nonparametric (i.e., it is not limited by a functional form), it determines the probability distribution for each valid function that can be used to fit the data. This allows us to fit a large amount of data to a flexible function, such as the surrogate model for the PES.

Let us assume a smooth, regular function y that takes a d -dimensional descriptor vector as input and produces a scalar value in the feature space:

$$y : \mathbb{R}^d \rightarrow \mathbb{R} \quad . \quad (4.2)$$

Although the functional form of y is not known, we have N observations y_n at the positions \mathbf{x}_n in the input space. The set of input-output pairs is collected as a dataset (generally called a training set):

$$D = \{(\mathbf{x}_n, y_n) | n = 1, \dots, N\} \quad . \quad (4.3)$$

With the dataset D , we aim to create a predictive distribution that can estimate the unknown continuous function y at unseen points of interest \mathbf{x} as well as quantify the uncertainty of the prediction.

The y is approximated by predicting \tilde{y} in the form of a linear combination of M basis functions:

$$\tilde{y}(\mathbf{x}) = \sum_{m=1}^M c_m k(\mathbf{x}, \mathbf{x}_m) \quad , \quad (4.4)$$

taken from a kernel space with similarity kernel k and weights c_m . Within the GPR approach, a squared exponential Gaussian kernel is used as a similarity measure,

$$k(\mathbf{x}, \mathbf{x}_m) = \exp\left(-\frac{|\mathbf{x} - \mathbf{x}_m|^2}{2\sigma^2}\right) \quad , \quad (4.5)$$

where σ is a length-scale hyperparameter called the Gaussian kernel width.

As in Eq. 4.1, the fitting of a GPR model aims to determine the weights c_m , which minimize the loss function l :

$$l = \sum_{n=1}^N \frac{|y_n - \tilde{y}(\mathbf{x}_n)|^2}{\sigma_n^2} + R \quad . \quad (4.6)$$

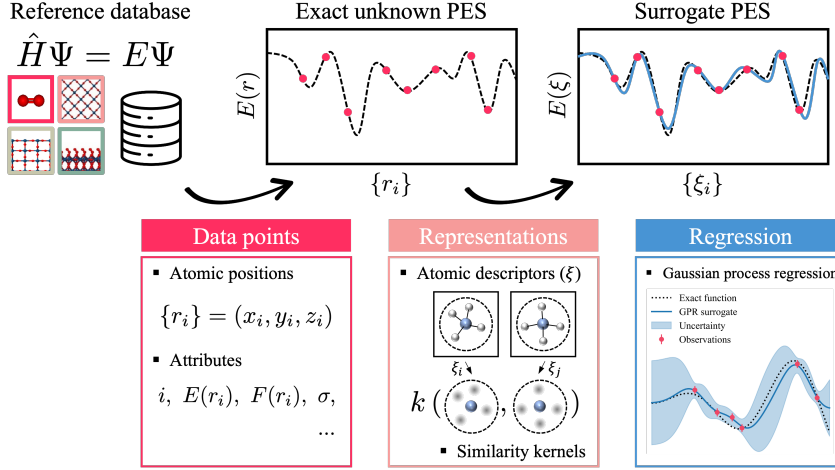


Fig. 4.1: Overview of the key ingredients for Gaussian process regression (GPR) and the Gaussian approximation potential (GAP) framework.

Within the GAP framework, R is a Tikhonov regularization term [202] and σ_n is an inverse weighting factor for a given data point. The regularization term R penalizes large regression coefficients σ_n , which would cause overfitting. Stronger regularization is achieved by increasing the relative contribution of R to the loss function. Eq. 4.6 is often written as follows:

$$l = \sum_{n=1}^N |y_n - \tilde{y}(x_n)|^2 + \sigma^2 R \quad , \quad (4.7)$$

when using a single $\sigma_n = \sigma$ parameter for all data points. The σ_n might be understood as the degree of uncertainty surrounding a specific data point or the expected accuracy of the GAP. Larger values of σ_n result in a smoother potential, whereas smaller values enable a more precise fit of the training set. One can use different values of σ_n for function values and derivatives to adjust the weight of each property in the loss function [202].

If the total number of basis functions is the same as the number of observations in the input data set (i.e., $M = N$), then the model is called a full GPR. However, a full GPR becomes increasingly computationally expensive as the training set grows since the training cost (in computational time) scales as $\mathcal{O}(N^3)$ and the memory requirement as $\mathcal{O}(N^2)$ (i.e., the prediction cost increases linearly). All GAP models use the regime of sparse GPR, which still uses the entire training data in the loss function but fewer representative points (i.e., $N \ll M$). Using the sparse model brings considerable savings in training costs compared with the full GPR, and the energy prediction cost becomes independent of the size of the training set [202]. To disperse the representative set with sufficient diversity, a uniform grid between zero and the cutoff length is sufficient for low-dimensional descriptors, such as the two-body (2B) potential (see Section 4.2.1 for details). However, for the high-dimensional representations, such as the many-body (MB) potential (see Section 4.2.2), such a strategy is extremely inefficient. Instead, the leverage-score CUR decomposition is used to select the most diverse representations of each species [204].

Fig. 4.1 displays an overview of the principal concepts of how the GPR/GAP framework

operates. It first requires a reference database of (usually) ab initio quantum-mechanical data for well-chosen structural models. The data include atomic positions as well as other attributes, such as DFT total energies E , atomic forces F , and virial stresses σ . These input data are assigned to points in the high-dimensional input space. At this point, the representation of each atomic structure is a list of Cartesian coordinates $\{r_i\}$, which is unsuitable for measuring similarities between different configurations due to its dependence on the absolute position and orientation in space as well as the order of the atoms. To overcome this problem, the data should be transformed into a well-adapted mathematical representation ξ , such as the mutual distances from center atom i to atoms j or the smooth overlap of atomic positions (SOAP) [205]. The kernel function k can be used to evaluate the similarity of two atomic environments using these representations of atomic descriptors ξ . Lastly, the surrogate PES model is obtained by GPR fitting with a limited number of input observations, with the quality of the resulting PES function assessed by quantifying the uncertainty [202].

In the next section, mathematical representations of atomic environment are introduced that are used in the GAP framework as well as I discuss the specific model used in this thesis.

4.2 Representation of Atomic Environments

As briefly mentioned, transforming the Cartesian coordinates of atoms into a suitable representation is necessary for constructing a data-driven regression model [206]. The mapping between high-dimensional atomic structures and low-dimensional feature space should follow several physically informed requirements. First, it should be complete and smooth (i.e., different structures should be mapped to discrete features); moreover, continuous deformations of a structure should map to a smooth regular behavior of representations so that it is interpolatable and differentiable. Second, the mapping should be equivalent under basic symmetries—translationally, permutationally, and rotationally invariant—so that symmetry equivalent structures have an identical representation. Third, it should reflect additivity so that a structure can be represented by the sum of local (atomic) environments.

The GAP model is developed to enable the following three representation levels to be used: the two-body (2B), three-body, and MB SOAP descriptors. In the following subsections, only the 2B and SOAP descriptors are introduced as they are used in the model herein.

4.2.1 Two-Body Descriptor

The simplest example of such a representation is the 2B descriptor, which transforms the relative positions of two atoms i and j into their atomic distances $r_{ij} = |\vec{r}_i - \vec{r}_j|$. It converts the vectorial data to a scalar quantity and guarantees translational, permutational, and rotational invariance. A squared exponential Gaussian kernel for the 2B descriptor is defined as follows:

$$k_{2B}(r_{ij}, r_m) = \exp\left(-\frac{|r_{ij} - r_m|^2}{2\sigma_{2B}^2}\right), \quad (4.8)$$

where σ_{2B} is a 2B kernel width for regulating the smoothness of the kernel. The 2B kernel provides a similarity measure of the input distance r_{ij} and the known data r_m . Consequently,

reformulating Eq. 4.4 makes it calculate the total energy of a system E_{2B} through a pairwise potential, which consists of M_{2B} number of Gaussian basis functions centered at sparse points r_m :

$$E_{2B}(\{r_{ij}\}) = \sum_{i,j} \varepsilon_{2B,ij} = \sum_{i,j} \sum_{m=1}^{M_{2B}} c_{m,2B} k_{2B}(r_{ij}, r_m) \quad , \quad (4.9)$$

where $\{r_{ij}\}$ includes all atomic distances of atoms i and j within the kernel-specific cutoff radius $r_{\text{cut},2B}$. The $r_{\text{cut},2B}$ constrains the 2B potential to be short-ranged to ensure additivity and appropriate computational scaling.

4.2.2 Many Body Descriptor: Smooth Overlap of Atomic Positions

The internal energy approximation cannot be perfectly described by the 2B descriptor and corresponding pair potentials; rather, higher-body order representations are required. However, simple higher-order terms with order $n > 2$ are not permutationally invariant and require other physics-inspired structural representations. One approach is to not approximate the total energy of a system by body order but instead to produce it as a sum of local atomic contributions ε_i , where each local contribution relies on the MB descriptors of atomic environments:

$$E_{\text{MB}}(\mathbf{X}_{\mathbf{n}}) = \sum_i \varepsilon_i = \sum_i \sum_{m=1}^{M_{\text{MB}}} c_{m,\text{MB}} k_{\text{MB}}(\xi_i, \xi_m) \quad , \quad (4.10)$$

where $\mathbf{X}_{\mathbf{n}}$ is the atomic coordinates of the system, $c_{m,\text{MB}}$ is the MB regression coefficients, and k_{MB} is the MB kernel function for measuring the similarities between two descriptors ξ_i and ξ_m , which are computed from $\mathbf{X}_{\mathbf{n}}$. As previously mentioned, multidimensional descriptors ξ_i within the GAP framework are vectorial representations of the atomic environment based on the SOAP [160, 184, 205]. The MB SOAP representation is invariant to permutation as it depends on spherical harmonic spectra, originally the bispectrum and later the power spectrum [205].

To obtain the SOAP representation of an atomic environment around an atom i , a set of smooth neighbor densities with respect to each chemical species a must be defined as follows:

$$\rho^{i,a}(\mathbf{r}) = \sum_j \delta_{a,a_j} \exp \left[\frac{-|r - r_{ij}|^2}{2\sigma_{\text{MB},a}^2} \right] f_{\text{cut}}(r_{ij}) \quad , \quad (4.11)$$

where j runs over neighbors of atom i within the cutoff radius r_{cut} , δ_{a,a_j} is a unique weight factor assigned according to the atomic species a , and $f_{\text{cut}}(r_{ij})$ is a cutoff function that smoothly approaches zero at r_{cut} . Furthermore, $\sigma_{\text{MB},a}$ is an element-specific length-scale hyperparameter for determining the regularity of the representation.

Each elemental neighbor density $\rho^{i,a}(\mathbf{r})$ is permutationally invariant for that element. It should be expanded on the basis of orthogonal radial functions $R_n(r)$ and spherical harmonics $Y_l^m(\mathbf{r})$ to achieve rotational invariance as follows:

$$\rho^{i,a}(\mathbf{r}) = \sum_{nlm} c_{nlm}^{i,a} R_n(r) Y_l^m(\mathbf{r}) \quad , \quad (4.12)$$

where the expansion coefficients $c_{nlm}^{i,a}$ are given by the following equation:

$$c_{nlm}^{i,a} = \int d\mathbf{r} R_n(r) Y_l^m(\mathbf{r}) \rho^{i,a}(\mathbf{r}) \quad . \quad (4.13)$$

A summation over m of the symmetrized combinations of these expansion coefficients with fixed l and i yields a rotationally invariant power spectrum $p_{nn'l}^{i,aa'}$:

$$p_{nn'l}^{i,aa'} = \frac{1}{\sqrt{2l+1}} \sum_m (c_{nlm}^{i,a})^* c_{n'lm}^{i,a'} \quad . \quad (4.14)$$

For the MB kernel, GAP uses low-order polynomial kernels instead of a standard Gaussian kernel,

$$k_{\text{MB}}(\xi_i, \xi_m) = (\xi_i \cdot \xi_m)^\zeta \quad , \quad (4.15)$$

where the SOAP representation of the local atomic environment ξ_i corresponds to the normalized power spectrum vector as follows:

$$\xi_i = \frac{\mathbf{p}_i}{|\mathbf{p}_i|} \quad , \quad (4.16)$$

where $\mathbf{p}_i = \{p_{nn'l}^{i,aa'}\}$.

By using a linear kernel $\zeta = 1$, the rotationally integrated squared overlap of the respective neighbor densities of two atoms is equivalent to the dot product of the power spectra. A kernel model from the linear kernel becomes a three-body term, which only depends on the Cartesian coordinates of triplets of atoms. When $\zeta = 2$, the model counts on four neighbors and results in five-body terms $(2\zeta + 1)$ [202]. Notably, although the increase of the body order does not contribute to extra computational costs in the kernel framework, it is rational to not choose a higher-body order than necessary for the target features, since in that case the model would converge much slower, requiring more reference input data.

4.2.3 Model in the Thesis

In this thesis, the GAP model is based on a combination of 2B and MB contributions. By combining Eqs. 4.9 and 4.10, I calculate the total energy E_{GAP} of a system as follows:

$$E_{\text{GAP}}(\mathbf{X}_{\mathbf{n}}) = \sum_{i,j} \delta_{2\text{B}}^2 \sum_{m=1}^{M_{2\text{B}}} c_{m,2\text{B}} k_{2\text{B}}(r_{ij}, r_m) + \sum_i \delta_{\text{MB}}^2 \sum_{m=1}^{M_{\text{MB}}} c_{m,\text{MB}} k_{\text{MB}}(\xi_i, \xi_m) \quad , \quad (4.17)$$

where $\delta_{2\text{B}}$ and δ_{MB} are hyperparameters that specify the expected relative weight of the 2B and MB energy contributions, respectively.

In principle, a pure MB description is achievable. However, the explicit incorporation of the 2B contribution was found to result in a significantly more stable and data-efficient potential [207]. Generally speaking, a simple 2B potential extrapolates much more effectively than a highly flexible high-dimensional representation of the MB contribution. The δ -weights for each term can therefore be used to balance between the flexibility and robustness of the potential. How we selected δ hyperparameters from heuristics is discussed in Section 4.3.2.

4.3 Hyperparameter Selection in a Nutshell

The GPR is parameter-free as the function estimator is obtained by specifying the priors, such as observations and Gaussian kernels. However, to obtain a good fit, appropriately setting the kernel and adjusting the observation noise are crucial. A global parameter for controlling such behavior of the fit is called a hyperparameter, and a set of hyperparameters should be carefully selected to specify the regression problem precisely [202].

Unfortunately, the set of hyperparameters cannot be optimized before the regression fit. Instead, an estimated set is first chosen to fit the model, and then the fitting error is measured afterwards. The primary goal is to find a set of hyperparameters that minimizes errors. The problem is that a risk of overfitting the training data always exists, since the number of degrees of freedom is large (i.e., the coefficients of representative points). Such overfitting causes unexpected large errors on the test data, which are not included in the training data [202].

In the GPR model, which is a Bayesian approach regression, the hyperparameters can be optimized by maximizing the marginal likelihood [208] and N -fold cross-validation, which are generally established techniques [202]. However, it is also possible to select satisfactory hyperparameters heuristically by using physiochemical principles and knowledge about the system without perfect optimization. This circumvents the high computational cost of accurate hyperparameter optimization, which is inefficient and unnecessary when the training set is transient (as it is iteratively updated) and can be more robust (i.e., a physics-inspired prior).

In this section, I briefly introduce how a set of hyperparameters was selected to train a RuO₂ GAP. As previously discussed, the total energy of a system is estimated by the δ -weighted contributions of 2B and MB terms and the regularization parameters σ in the loss function. We evaluate regularization differently for energies and forces and use the separate parameters σ_ϵ and σ_f , respectively. In addition, the number of sparse points M_{2B} and M_{MB} is required for sparse kernel models. More hyperparameters are related to the choice of representations and kernels, such as the cutoff radius ($r_{\text{cut},2B}$ and $r_{\text{cut},MB}$), kernel widths (σ_{2B} and σ_{MB}), and number of radial and angular basis functions for SOAP kernels (n_{max} and l_{max} , respectively). In this thesis, technical hyperparameters for the RuO₂ GAP are selected primarily from heuristics and the rest through four-fold cross-validation.

4.3.1 Locality Test

As discussed in Section 4.2, the GAP estimates the total energy of the system by the sum of local contributions, which result from the choice of an applied cutoff radius r_{cut} . Hence, it neglects any long-range interactions originating from electrostatics or dispersion outside of the cutoff region. To minimize such errors, force locality [207] was tested for symmetry inequivalent atoms $\{s\}$ on the oxygen-rich RuO₂(101) surface. Based on the ground-state surface supercell \mathbf{X} with all atomic forces relaxed, we generated a set of perturbed configurations $\{\mathbf{X}'\}$, for which all atom positions outside of r_{cut} from $\{s\}$ were randomly displaced. The induced force at the center atom s was then measured as the force difference of the ground-state and the perturbed configurations $\Delta\mathbf{f}_s = |\mathbf{f}_s^{\mathbf{X}'} - \mathbf{f}_s^{\mathbf{X}}|$ as a function of r_{cut} . In detail, the Gaussian random perturbations were applied uniformly with a standard deviation of 0.05 Å and limited to a maximum displacement of individual

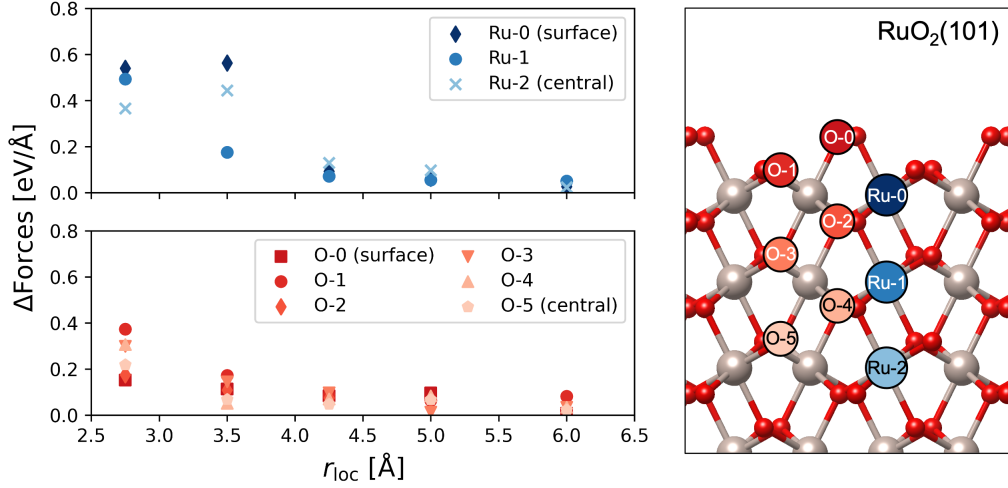


Fig. 4.2: Locality test for a $\text{RuO}_2(101)$ oxygen-rich surface, which illustrates that induced force on a given central atom upon displacement of atoms outside of a radius r_{loc} . To provide some statistics, three and six different central atoms for Ru and O, respectively, are considered from the outermost to the inner atomic layers in the slab, as illustrated in the right panel.

atoms below 0.2 \AA . As a result, Δf_s was converged for all atoms $\{s\}$ at $r_{\text{cut}} > 4.25 \text{ \AA}$ (see Fig. 4.2); thus, $r_{\text{cut},2\text{B}} = r_{\text{cut},\text{MB}} = 5.0 \text{ \AA}$ was used.

4.3.2 Hyperparameters from Physics-Inspired Heuristics

The 2B scaling factor $\delta_{2\text{B}}$ scales the atomic pair potential contribution to the total energy, and it should reflect the cohesive energies E^{coh} of systems in the bootstrapping training set. The $\delta_{2\text{B}}$ herein is set as related to the standard deviation of E^{coh} as follows:

$$\delta_{2\text{B}} = \frac{1}{b_{2\text{B}}} \sum_n \frac{\left(E_n^{\text{coh}} - \overline{E_n^{\text{coh}}}\right)^2}{N}, \quad (4.18)$$

where $b_{2\text{B}}$ is an average number of bonds, normalizing the cohesive energy to atomic pairwise contributions for the 2B descriptor. The δ -weight parameters used herein were designed to enable the resulting GAP to obtain a strong 2B character and flexible MB contributions, thereby narrowing the gap between the exact and surrogate potential energy surfaces. Accordingly, the MB scaling factor δ_{MB} is relevant for the difference between 2B only GAP-based cohesive energies and their DFT references $\Delta E^{\text{coh}} = |E^{\text{DFT,coh}} - E^{\text{GAP}^{2\text{B},\text{coh}}}|$ in the initial training set:

$$\delta_{\text{MB}} = \sum_n \frac{\left(\Delta E_n^{\text{coh}} - \overline{\Delta E_n^{\text{coh}}}\right)^2}{N}. \quad (4.19)$$

Furthermore, the regularization factors $\sigma_\varepsilon/\sigma_f$ are strongly correlated to the weight for

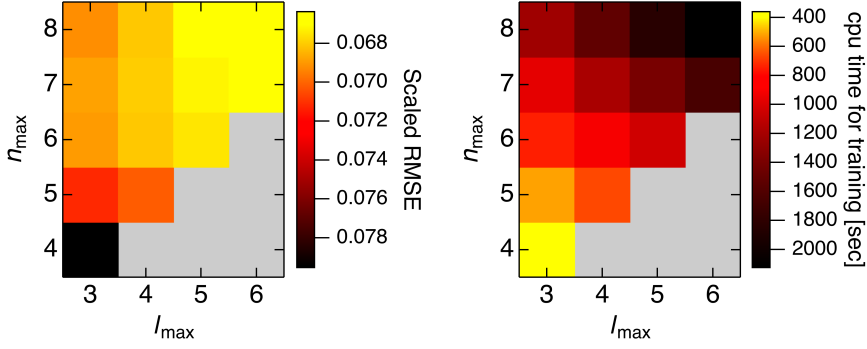


Fig. 4.3: Four-fold cross-validation results of the number of radial and angular basis functions (n_{\max} and l_{\max} , respectively) in SOAP kernels. Left: The color map indicates the scaled sum of the root mean square error (RMSE) for energies and forces and (right) average computational costs in CPU time for training. The RMSE of forces is scaled by 0.1 to make it comparable to that of energies.

the 2B term δ_{2B} , and there are similar high-performing sets of parameters from heuristics:

$$\sigma_\varepsilon = 10^{-3} \cdot \frac{1}{b_{2B}} \sum_n^N \frac{(E_n^{\text{coh}} - \overline{E_n^{\text{coh}}})^2}{N} , \quad (4.20)$$

$$\sigma_f = \sqrt{\sigma_\varepsilon} .$$

The scaling factor 10^{-3} is selected according to harmonic estimation and the type of materials (in this case solid), for which a lower absolute error is preferred for different configurations close to the local minima than, for example, liquid [202].

4.3.3 Hyperparameters from Four-Fold Crossvalidation

The remaining hyperparameters were selected through four-fold cross-validation [162]. For this, the initial training set without a set of atomic information $\{x\}$ was randomly divided into four subsets $\{\mathbf{a}, \mathbf{b}, \mathbf{c}, \mathbf{d}\}$. Three of the four subsets plus $\{x\}$ became a training set, and the remaining subset was used for validation. Thus, a total of four sets of training and validation data were obtained for the accuracy evaluation of the GAP trained with one set of hyperparameters. Various sets of hyperparameters were tested, one of which minimized the RMSE and was selected.

As an example, the results of a test for finding an appropriate set of n_{\max} and l_{\max} are presented in Fig. 4.3. Here, only sets of n_{\max} and l_{\max} where n_{\max} is larger than l_{\max} were tested as it is empirically known that such a choice generally leads to higher accuracy [202]; n_{\max} and l_{\max} were set as 8 and 4, respectively, to ensure a relatively smaller RMSE for reasonable computational costs.

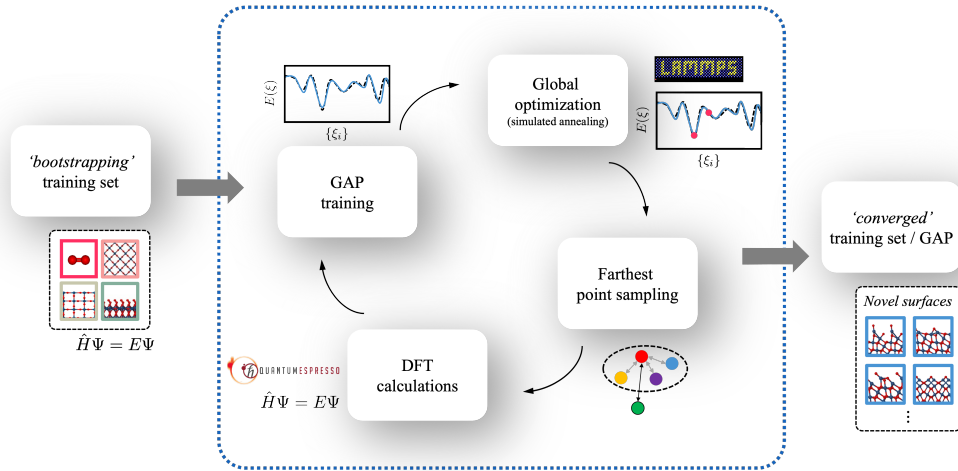


Fig. 4.4: Schematic workflow of the iterative GAP training protocol.

4.3.4 UniversalSOAP

For the RuO_2 GAP, length-scale hyperparameters for the SOAP descriptor (i.e., a cutoff radius r_{cut} and a kernel width σ_{MB}) were chosen based on the results of a locality test and four-fold cross-validation. However, GAP provides a tool—named UniversalSOAP—to suggest these SOAP hyperparameters for arbitrary elements and their combinations from heuristics [209]. In detail, UniversalSOAP provides the relevant length scales based on the characteristic bond lengths in each single-element system. For an atom species Z , a typical bond length r_{typ}^Z is computed by comparing energies of six structures (dimer, graphite, diamond, β -Sn, body-centered cubic, and face-centered cubic). The bond length of the lowest-energy structure among them is defined as r_{typ}^Z . For each species, cutoff transition widths r_{trans} and a cutoff radius r_{cut} for short- and long-range are then selected based on the r_{typ}^Z . The kernel width σ_{MB} is maintained proportional to the cutoff radius $r_{\text{cut,MB}}$ by $\sigma = r_{\text{cut}}/8$.

4.4 Case Study: $c(2 \times 2)$ $\text{RuO}_2(100)$ Reconstruction

To obtain a well-defined RuO_2 GAP, we developed a general and data-efficient iterative training protocol that allows for the on-the-fly generation of GAPs through a surface exploration process [162]. A schematic workflow for the protocol is illustrated in Fig. 4.4. In this section, I briefly introduce the process and results of surface structure determination for unknown $c(2 \times 2)$ - $\text{RuO}_2(100)$.

The training protocol started with an initial training set, which included minimalistic reference data to establish a preliminary potential. Since the first GAP V_0 should accomplish a baseline to describe the target system, it was necessary to select reference structures that can represent the chemistry of the system and eliminate nonphysical behavior in pairwise potentials. Therefore, the initial training set contained atomic information, data

for O₂ dimers with varying O-O distances, and rutile RuO₂ bulk structures at compressed, optimized, and decompressed DFT lattice parameters as well as with displaced internal coordinates. In a purpose-driven approach to surface structure exploration, different (1 × 1) terminations of all five low-index surfaces of rutile RuO₂ were included, both in the bulk-truncated geometry (as depicted in Fig. 3.2) and in the DFT optimized geometry.

The initial GAP V_0 was trained based on this initial training set with a heuristically selected set of hyperparameters [162]. This GAP V_0 was, of course, not perfect and needed to be refined in an iterative process. The inclusion of surface geometries already allowed access to the respective surrogate PES at this point, although the PES was not yet reliable. Using specific global optimization and PES exploration techniques (simulated annealing in this thesis), new metastable surface structures (GAP PES basins) were exclusively identified. Farthest point sampling (FPS), which refers to measuring the kernel distance κ between all previously identified basins and new GAP basin candidates, was performed to efficiently sample unknown structures for further DFT optimizations (for more details, see our publication [162]). The FPS drastically reduced the number of DFT calculations, which would otherwise consume a large portion of the total CPU hours. The finally sampled basin structures were added to the training set to refine the GAP. We iteratively repeated this protocol until the FPS found no more unknown basins. The final pool of known basins contained an additional (1 × 1) surface structures for RuO₂.

We then extended the search space to the larger supercell of $c(2 \times 2)$ for RuO₂(100) by including bulk-truncated and DFT geometry relaxed $c(2 \times 2)$ slabs into the training set. In this second stage, the iterative refinement of RuO₂ GAP proceeded only for $c(2 \times 2)$ supercell surfaces. Consequently, 21 $c(2 \times 2)$ structures were additionally present in the final training data.

Through this on-the-fly generation of RuO₂ GAP, a total of 17 unknown $c(2 \times 2)$ reconstructions were newly identified. In Fig. 4.5, their computed surface free energies $\gamma_{\text{surf}}^{(hkl),\sigma}$ are presented as a function of the oxygen chemical potential change $\Delta\mu_{\text{O}}$. Specifically, in the stable range of $\Delta\mu_{\text{O}}$ according to Eq. 3.10, the two lowest energy surfaces for O-rich and O-superrich terminations (i.e., $c(2 \times 2)$ -* and $c(2 \times 2)$ -O, respectively), were finally determined. Due to the exceptionally low surface free energy of $c(2 \times 2)$ -O—only 3 meV/Å² at the O-rich limit ($\Delta\mu_{\text{O}} = 0$ eV)—the lowest surface free energy of the (100) facet under oxidative conditions became lower than that of the (110) facet (see the right panel of Fig. 4.5). As discussed in Section 3.1, the equilibrium shape of a crystal follows the shape given by the Wulff construction, which has the minimum surface energy. Thus, the experimentally observed evolution of the (100) microfacets on the (110) surface can be interpreted simply by comparing surface free energies [126]. Ideally, the angle between (100) and (110) facets is 45° and (100) facets can restrain (110), where their surface free energies fulfill the following equation:

$$2A^{(100)} \cdot \gamma_{\text{surf}}^{(100)} < 2A^{(100)} \cos \frac{\pi}{4} \cdot \gamma_{\text{surf}}^{(110)} \quad \Rightarrow \quad \sqrt{2}\gamma_{\text{surf}}^{(110)} - 2\gamma_{\text{surf}}^{(100)} > 0 \quad . \quad (4.21)$$

Consequently, the chemical potential range $\Delta\mu_{\text{O}} \geq -0.325$ eV, where Eq. 4.21 is fulfilled, is marked by the red shaded area in the right panel of Fig. 4.5. As indicated there, Wulff crystals corresponding to the lower chemical potential ($\Delta\mu_{\text{O}} = -0.820$) and at $\Delta\mu_{\text{O}} = -0.325$ eV also represent a reduction and eventual disappearance of the (110) contribution (yellow facet). Above $\Delta\mu_{\text{O}} = -0.325$ eV (the right vertical gray dashed line), all (110) facets are

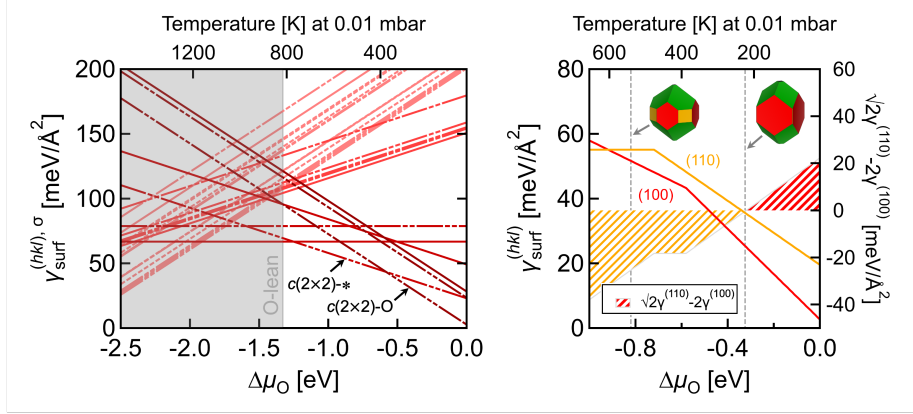


Fig. 4.5: Left: Computed surface free energy of $\text{RuO}_2(100)$ facet $\gamma_{\text{surf}}^{(100),\sigma}$ in an oxygen environment. The five solid lines correspond to the conventional, DFT relaxed (100) surfaces with different oxygen coverages and all other newly found PES basins from the GAP training protocol. Among them, the dashed lines indicate $p(1 \times 1)$ surfaces, whereas dash-dotted lines indicate $c(2 \times 2)$ reconstructions. Right: Comparison between surface free energies of (100) (red line) and (110) (yellow line) facets under oxidative conditions. The red and yellow shaded area indicates a thermodynamic descriptor of $\sqrt{2}\gamma_{\text{surf}}^{(110)} - 2\gamma_{\text{surf}}^{(100)}$ that indicates whether (100) facets can restrain (110) (see text). Corresponding Wulff crystals at $\Delta\mu_{\text{O}} = -0.820$ and -0.325 eV are presented as insets.

thermodynamically unstable and replaced by oxygen-terminated $c(2 \times 2)$ - $\text{RuO}_2(100)$, which rationalizes the earlier experimental finding of (100) microfacets on the (110) surface [126].

5 Publications

This chapter provides an overview of the relevant publications by me and co-authors during my PhD period. Each overview includes a brief summary of each article and my detailed contributions. The corresponding original articles are attached in the appendix of the thesis.

5.1 Ruthenium Oxide Nanosheets for Enhanced Oxygen Evolution Catalysis in Acidic Medium

Sourav Laha, Yonghyuk Lee, Filip Podjaski, Daniel Weber, Viola Duppel, Leslie M. Schoop, Florian Pielhofer, Christoph Scheurer, Kathrin Müller, Ulrich Starke, Karsten Reuter and Bettina V. Lotsch
Adv. Energy Mater. **9**, 1803795 (2019)
DOI: [10.1002/aenm.201803795](https://doi.org/10.1002/aenm.201803795)

Summary: With the motivation to reduce the mass load of precious iridium in water electrolysis catalyst, our experimental collaborators from the Max-Planck-Institut für Festkörperforschung successfully synthesized highly active and robust hexagonal ruthenium oxide nanosheets for the electrocatalytic oxygen evolution reaction in acidic media. In detail, the nanosheets were prepared by exfoliation of proton exchanged α -NaRuO₂. These nanosheets exhibited the best OER activity of all acidic medium electrocatalysts reported before. The experimentally observed current density was reaching 10 mA cm⁻² at an overpotential of only 255 mV. In order to understand the origin of the exceptionally high activity, theoretical analysis, including ab initio thermodynamics combined with the computational hydrogen electrode approach, was performed. We first investigated all possible coverages of intermediate species, i.e. O*, OH*, OOH*, and OO* at sheet surfaces and interfaces between adjacent sheets. However, all oxygens at the sheet surface are threefold-coordinated and consequently bind strongly to Ru atoms. These oxygens are much less reactive than the twofold bridging oxygens or onefold terminal oxygens present in active rutile RuO₂. Furthermore, this strong Ru-O binding feature inversely weakens the additional O-H and O-OH bonds forming on top. Especially highly oxidized species such as adsorbed hydroperoxo (OOH*) and superoxo (OO*) groups are unstable under OER operating conditions, which is in contrast to the situation at rutile RuO₂ surfaces. This leads to high overpotentials for any oxide path that involves the O₂ evolution out of such oxygen species. We concluded that the surface of nanosheets is unlikely the reason for the experimentally measured high OER activity. Alternatively, we investigated vacancies or defects in the sheets or at the edges of the sheets, which could be the origin of the high activity. Especially, the edges naturally have Ru_{cus} and bridging or terminal oxygens. Under OER conditions, the partially hydroxylated (OH*) edge becomes the most stable, however, higher oxidized structures such as O* and OOH* are quickly stabilized at potentials around 1.5 V. We computed a minimum thermodynamic overpotential η_{TD} of only 0.43 V to make all steps of the DFT peroxide pathway (mechanism IV in Table 2.1) exergonic and confirmed the sheet edge as a highly active OER zone.

Individual Contributions: Following the initial experimental observations from Prof. Bettina Lotsch's group, I carried out all DFT-based theoretical calculations in the presented article under the guidance of Christoph Scheurer and Karsten Reuter. I designed all structural models for RuO₂ nanosheets with varying morphologies and adsorbates. All theory part of the final manuscript was then jointly written by Christoph Scheurer, Karsten Reuter, and myself. The first author Dr. Sourav Laha was performing experiments and was not involved in the theory part.

5.2 Epitaxial Core-Shell Oxide Nanoparticles: First-Principles Evidence for Increased Activity and Stability of Rutile Catalysts for Acidic Oxygen Evolution

Yonghyuk Lee, Christoph Scheurer and Karsten Reuter
ChemSusChem **15**, e202200015 (2022)
DOI: [10.1002/cssc.202200015](https://doi.org/10.1002/cssc.202200015)

Summary: We continued model studies with the motivation of lowering the price of IrO₂-based catalysts while maintaining or even improving the OER activity for future applications on an industrial scale. A common approach to reducing the content of iridium is to exploit the property of IrO₂ to form solid solutions with other transition metal oxides that crystallize in rutile structures such as titanium oxide. Preceding experimental work demonstrated that IrO₂ is diluted by cheaper materials, either as a solid solution or core-shell structure, without sacrificing desirable properties, including electrical conductivity and catalytic activity. Here, we focused on core-shell nanostructures, which have been widely investigated due to their high efficiency and flexibility in tuning their morphology. In order to build core-shell heterostructures, it is indispensable to minimize the lattice mismatch at the interface, which causes strain effects and potentially physical instability of a material. In this respect, rutile oxides have a considerable advantage since the highly oxidized metal ions (4+) are relatively small for most elements, hence limiting the lattice mismatch between many rutile oxides. We systematically considered all possible low Miller-index interface structures for IrO₂/TiO₂ and RuO₂/TiO₂ to assess the lattice mismatch and their stability. By using stability descriptors, e.g. interface formation energy and work of adhesion, these interfaces were found to be stable enough and feasible to encapsulate a cheap rutile TiO₂ core with coherent thin IrO₂ and RuO₂ films. I created all low-index facets, i.e. (001), (010), (011), (110), and (111), while varying not only the coverage of oxygen but also different OER intermediate adsorbates. This study was highly demanding since there are a large number of degrees of freedom for these intermediates at rutile surfaces, and we should consider all of them to determine the most stable configurations. Based on our analysis via ab initio thermodynamics, we pointed out better wetted core-shell particles should grow under oxidizing conditions, as, for example, achievable by electrodeposition. Our calculations further demonstrated increased stability of core-shell particles at OER operation conditions since the exposure of TiO₂ penalizes a dewetting or strain-relieving formation of defects.

Individual Contributions: Working within the Kopernikus/P2X¹ consortium, I initiated this project following the idea of Karsten Reuter. I also participated in the summer of simulation program by Leibniz Supercomputing Centre to obtain the computational resources for initial calculations. I extended the structure generating python code for rutile surfaces to enable to consider all OER adsorbates with different initial configurations and generated interface and surface models. All included DFT calculations were performed by myself. The manuscript was jointly written and edited by all authors.

¹<https://www.kopernikus-projekte.de/projekte/p2x>

5.3 Further works

The following articles have been published during my doctorate at the Chair of Theoretical Chemistry or are in preparation. The first two articles are topically related to ML-based surface structure determination of RuO₂, containing a general training workflow for ML GAPs as well as novel discoveries for both RuO₂ and IrO₂ via correlated methodology. The third manuscript contains the hidden mechanisms for CO oxidation at $c(2 \times 2)$ -RuO₂ that is explained in detail in chapter 3.3.2 of this thesis. Others have no direct relation to this specific topic but include results of computational chemistry studies by myself and co-authors.

- 1. IrO₂ Surface Complexions Identified through Machine-Learning and Surface Investigations**
Jakob Timmermann, Florian Kraushofer, Nikolaus Resch, Peigang Li, Yu Wang, Zhiqiang Mao, Michele Riva, Yonghyuk Lee, Carsten Staacke, Michael Schmid, Christoph Scheurer, Gareth S. Parkinson, Ulrike Diebold, and Karsten Reuter
Phys. Rev. Lett. **125**, 206101 (2020)
- 2. Data-Efficient Iterative Training of Gaussian Approximation Potentials: Application to Surface Structure Determination of Rutile IrO₂ and RuO₂**
Jakob Timmermann, Yonghyuk Lee, Carsten G. Staacke, Johannes T. Margraf, Christoph Scheurer, and Karsten Reuter
J. Chem. Phys. **155**, 244107 (2021)
- 3. Hidden Mechanism of CO Oxidation Deactivation on $c(2 \times 2)$ -RuO₂(100) Reconstruction**
Yonghyuk Lee, Jakob Timmermann, Chiara Panosetti, Christoph Scheurer, and Karsten Reuter
in preparation
- 4. Layered Honeycomb Iridates for the Oxygen Evolution Reaction: A Structure-Activity Study**
Sourav Laha, Yonghyuk Lee, Sebastian Bette, Lorenz Falling, Tomohiro Takayama, Igor Moudrarkovski, Peter Schützendübe, Hidenori Takagi, Robert Dinnebier, Christoph Scheurer, Karsten Reuter, Nella M. Vargas-Barbosa, and Bettina V. Lotsch
in preparation
- 5. Separating Gas Phase Induced Kinetic and Thermodynamic Structural Changes in an Open Oxide by Identical Location Imaging**
Liudmyla Masliuk, Kyeonghyeon Nam, Annette Trunschke, Travis Jones, Di Wang, Yonghyuk Lee, Christoph Scheurer, Karsten Reuter, Robert Schlögl, and Thomas Lunkenbein
in preparation

6 Summary, Conclusions, and Outlook

The production of green hydrogen is one of the central energy conversion techniques for a sustainable future, and boosting concomitant water electrolysis with adequately designed heterogeneous catalysts is indispensable. As discussed throughout this thesis, PEM water electrolyzers are a promising device with high potential in industrial applications for replacing current CO₂-producing steam reforming approaches. Improving the rate-limiting acidic OER will play a pivotal role in boosting the use of PEMELs. Over the last few decades, TMOs have been focused on as highly efficient electrocatalysts due to their exceptional physiochemical properties for many target chemical reactions. Specifically, RuO₂ and IrO₂ are the best-known OER catalysts with high stabilities in acidic environments. While RuO₂ exhibits higher OER activity, IrO₂ is more robust. Therefore, IrO₂ has been used for most commercial acidic OER catalysts. However, an industrial-scale problem originates from the low abundance and insufficient annual production of iridium to meet demands, resulting in cost-inefficient PEM cells. Therefore, a major challenge for a future large-scale application is to reduce the cost of IrO₂-based catalysts while maintaining or perhaps increasing OER activity.

A common approach for reducing the content of iridium is to exploit the properties of IrO₂ to form solid solutions with other TMOs that crystallize in rutile structures, such as ruthenium, tin, manganese, and titanium oxides. A second approach is to find a suitable method of using RuO₂ by stabilizing it through structural modifications, such as nanostructuring or phase transformation. Although several successful attempts through experiments have been made, both approaches require an in-depth microscopic and mechanistic understanding of the interfaces of the target systems, especially under dynamic and technologically relevant conditions. Thus, computational materials science and technology have become some of the most successful and widely used methods in the field, providing a broad range of information. For instance, the information ranges from a fundamental understanding of physical and chemical phenomena and the arising material properties to a structure-performance-process continuum, which can be further exploited to design and discover novel materials. Following this approach, this thesis has presented applications of the concepts of phase transformation and core-shell nanostructuring to RuO₂ and IrO₂ catalysts. The first study, motivated by our experimental collaborators, demonstrated the effectiveness of computation at revealing active sites of ruthenate nanosheets and the hidden underlying OER mechanism [1]. It also led to valuable experience in cross-disciplinary collaboration, which is necessary for resolving the many remaining open questions at a rather vague boundary of the field. The second study employed computational screening to assess the stabilities and activities of core-shell systems [2]. High-throughput computational methods were required to sample relevant surface configurations among all conceivable terminations of surfaces and arrangements of OER intermediates with many degrees of freedom. Such a systematic procedure was indeed highly demanding; however, it was necessary to reliably identify a thermodynamic descriptor for assessing the stability of surfaces of OER catalysts and to provide a perspective for ideal

synthesis conditions of such core-shell nanoparticles.

Besides these studies, more state-of-the-art ML methods have been applied for the surface structure determination of working catalysts under dynamic conditions. Recent advances in ML interatomic potentials have greatly accelerated the momentum in exploring the complex potential energy surface of target systems. My research colleague Jakob Timmermann and I developed a general and data-efficient training workflow to produce GAPs as a powerful application of such ML potentials [162]. With a fully automatized, on-the-fly generation of GAPs, novel surface structures of RuO₂ and IrO₂ were unveiled through a parallel surface exploration process. Extending the search space of the workflow to a larger supercell of RuO₂(100), we effectively sampled unique $c(2 \times 2)$ reconstructions, which exhibited remarkably low surface free energies. Although many uncertainties still remain for the clear demonstration of these structural models to explain all experimental observations, our work has already paved the way toward the ultimate solution to the longstanding questions in RuO₂ catalysis. Furthermore, it has provided a methodological guideline for analogous future research objectives.

As a closing remark, I wish to stress the aesthetics of research in the pursuit of a doctorate. Obviously, not every moment of the research was bliss, and I encountered frustrations as well as thorny, winding paths to reach my goals. Even at this final stage, I am not aware of all of the magnificent knowledge in the field of theoretical chemistry. However, many short but delightful moments both in research and social activities with group members have filled my PhD period with happiness, and my experiences—even the failures—have taught me a great deal. Like a poem by Cavafy, wealth is already gained along the way. Lastly, I hope that all of my endeavors in the field thus far push the boundaries of science to any extent.

Acknowledgments / Danksagung

I first would like to thank my supervisor Prof. Dr. Karsten Reuter, for giving me the opportunity to carry out projects and pursue a PhD. I genuinely appreciate his idea, insight, guidance, and passion for research, and for letting me acquire experience in many international conferences. I still remember his warm welcome to the group at the first meeting at "Karsten's cantina". I was greatly relieved at my first challenge to start living and studying in a foreign country.

Right afterward, I want to thank Dr. Christoph Scheurer, who has worked most closely with me as a group leader, for all the academic guidance, scientific discussions, and considerations. His amazing knowledge in literally every field inspires me all the time. His understanding and kind suggestions were conducive whenever I felt anxious about my progress. I also would like to thank Hannes and Chiara for their considerate advice.

Moreover, I give special thanks to the entire group for the incredible moments during my stay. My dearest colleague and the first officemate Dr. Jakob Timmermann, I always respect his decisiveness and admire a perfect work-life balance. All chats and discussions we had were delightful. In the aspect of music and arts, Simiam Ghan led me deeper into such confidential fields by attending an amazing outdoor classic concert in Wien and many museums in Berlin. Also, big thanks to Hendrik, Wenbin, Sina Stocker, and Thorben for creating a unique atmosphere in our office. I am especially grateful for the senior group members who spent most of my PhD together: Martin, Christian, Cristina, David, Jakob F., Simon, Simeon. I want to thank our small Korean cluster, Nam and Hyunwook. Lastly, I send my appreciation to other group members that I cannot list all names here.

Some good friends made life in Berlin more delightful. Thanks, Woosun, for making my settlement in Berlin smooth by introducing all the friends. Thank you, Sooseok, for being a host for fabulous techno parties during Corona, and Jaehee, for fascinating us again into Berlin fashion and clubs. Daniel and Yerin deserve big gratitude for taking care of Dajeong and me with full of affection. Greeting all other friends for their warm hearts: Inho, Suyoung, Minyoung, Dani, Sungkyu, Cheoljung, Dobi, Hyoseung, Sophie, Taekwon, Kisung, and Suhyun. Also, I truly appreciate friends who have always sent their love and advice despite a far distance: Taehun, Luke, Youngjun, Sungrae, Kyeongsoon, Yongbeom, Jaewon, Chiho, Jaekun, and Kitae.

I sincerely thank my great parents and Yongsuk, who always give me love and support without condition. I also want to thank my grandparents, who consistently care for and encourage me with wise advice. I appreciate Dajeong's family for their assistance and prayer. Finally, I want to thank and send love to Dajeong for her love, patience, and support.

München, September, 2022

이 용 필

Bibliography

- [1] S. Laha, Y. Lee, F. Podjaski, D. Weber, V. Duppel, L. M. Schoop, F. Pielnhofer, C. Scheurer, K. Müller, U. Starke, K. Reuter, and B. V. Lotsch, *Adv. Energy Mater.* **9**, 1803795 (2019) (cit. on pp. [1](#), [2](#), [5](#), [6](#), [49](#)).
- [2] Y. Lee, C. Scheurer, and K. Reuter, *ChemSusChem* **15**, e202200015 (2022) (cit. on pp. [1](#), [2](#), [9](#), [11](#), [13](#), [22](#), [24](#), [27](#), [28](#), [49](#)).
- [3] H.-O. Pörtner, D. C. Roberts, H. Adams, C. Adler, P. Aldunce, E. Ali, R. A. Begum, R. Betts, R. B. Kerr, R. Biesbroek, et al., *IPCC Sixth Assessment Report* (2022) (cit. on p. [1](#)).
- [4] H. Ritchie, M. Roser, and P. Rosado, *OWID* (2020) (cit. on p. [1](#)).
- [5] M. Carmo, D. L. Fritz, J. Mergel, and D. Stolten, *Int. J. Hydrog. Energy* **38**, 4901 (2013) (cit. on pp. [1](#), [5–7](#)).
- [6] Y. Sun, Z. Zhao, M. Yang, D. Jia, W. Pei, and B. Xu, *CSEE J. Power Energy Syst.* **6**, 160 (2019) (cit. on p. [1](#)).
- [7] A. Buttler and H. Spliethoff, *J. Renew. Sustain. Energy* **82**, 2440 (2018) (cit. on pp. [1](#), [6](#)).
- [8] D. Bessarabov, H. Wang, H. Li, and N. Zhao, *PEM electrolysis for hydrogen production: principles and applications* (CRC press, 2016) (cit. on p. [1](#)).
- [9] A. G. Olabi, A. A. Abdelghafar, A. Baroutaji, E. T. Sayed, A. H. Alami, H. Rezk, and M. A. Abdelkareem, *Int. J. Hydrog. Energy* **46**, 23498 (2021) (cit. on p. [1](#)).
- [10] M. F. Ahmad Kamaroddin, N. Sabli, T. A. Tuan Abdullah, S. I. Siajam, L. C. Abdullah, A. Abdul Jalil, and A. Ahmad, *Membranes* **11**, 810 (2021) (cit. on p. [1](#)).
- [11] L. D. Burke and T. O. O'Meara, *J. Chem. Soc. Faraday Trans. 1* **68**, 839 (1972) (cit. on pp. [1](#), [7](#)).
- [12] J. H. Russell, L. J. Nuttall, and A. P. Fickett, *Am. Chem. Soc. Div. Fuel Chem. Prepr* **18**, 24 (1973) (cit. on pp. [1](#), [7](#)).
- [13] T. Reier, H. N. Nong, D. Teschner, R. Schlögl, and P. Strasser, *Adv. Energy Mater.* **7**, 1601275 (2017) (cit. on pp. [1](#), [7](#)).
- [14] S. S. Kumar and V. Himabindu, *Mater. Sci. Energy Technol.* **2**, 442 (2019) (cit. on pp. [1](#), [7](#)).
- [15] L. Li, P. Wang, Q. Shao, and X. Huang, *Adv. Mater.* **33**, 2004243 (2021) (cit. on pp. [1](#), [7](#)).
- [16] S. Trasatti, *J. Electroanal. Chem.* **111**, 125 (1980) (cit. on pp. [1](#), [2](#), [19](#)).
- [17] T. Reier, M. Oezaslan, and P. Strasser, *ACS Catal.* **2**, 1765 (2012) (cit. on pp. [1](#), [2](#)).

- [18] Y. Lee, J. Suntivich, K. J. May, E. E. Perry, and Y. Shao-Horn, *J. Phys. Chem. Lett.* **3**, 399 (2012) (cit. on pp. **2**, **6**, **22**).
- [19] N. Danilovic, R. Subbaraman, K.-C. Chang, S.-H. Chang, Y. Kang, J. Snyder, A. P. Paulikas, D. Strmcnik, Y.-T. Kim, D. Myers, V. R. Stamenkovic, and N. M. Markovic, *Angew. Chem. Int. Ed.* **53**, 14016 (2014) (cit. on p. **2**).
- [20] H. Over, *ACS Catal.* **11**, 8848 (2021) (cit. on pp. **2**, **5**, **10**, **12–14**).
- [21] O. Diaz-Morales, S. Raaijman, R. Kortlever, P. J. Kooyman, T. Wezendonk, J. Gascon, W. T. Fu, and M. Koper, *Nat. Commun.* **7**, 1 (2016) (cit. on p. **2**).
- [22] L. C. Seitz, C. F. Dickens, K. Nishio, Y. Hikita, J. Montoya, A. Doyle, C. Kirk, A. Vojvodic, H. Y. Hwang, J. K. Nørskov, and T. F. Jaramillo, *Science* **353**, 1011 (2016) (cit. on pp. **2**, **9**).
- [23] V. A. Saveleva, L. Wang, W. Luo, S. Zafeiratos, C. Ulhaq-Bouillet, A. S. Gago, K. A. Friedrich, and E. R. Savinova, *J. Phys. Chem. Lett.* **7**, 3240 (2016) (cit. on p. **2**).
- [24] D. Lebedev, M. Povia, K. Waltar, P. M. Abdala, I. E. Castelli, E. Fabbri, M. V. Blanco, A. Fedorov, C. Copéret, N. Marzari, and T. J. Schmidt, *Chem. Mater.* **29**, 5182 (2017) (cit. on p. **2**).
- [25] J. Park, M. Park, G. Nam, M. G. Kim, and J. Cho, *Nano Lett.* **17**, 3974 (2017) (cit. on p. **2**).
- [26] J. Kim, P.-C. Shih, K.-C. Tsao, Y.-T. Pan, X. Yin, C.-J. Sun, and H. Yang, *J. Am. Chem. Soc.* **139**, 12076 (2017) (cit. on p. **2**).
- [27] K. A. Stoerzinger, O. Diaz-Morales, M. Kolb, R. R. Rao, R. Frydendal, L. Qiao, X. R. Wang, N. B. Halck, J. Rossmeisl, H. A. Hansen, T. Vegge, I. E. L. Stephens, M. T. M. Koper, and Y. Shao-Horn, *ACS Energy Lett.* **2**, 876 (2017) (cit. on pp. **2**, **11**, **13**).
- [28] S. Siracusano, V. Baglio, C. D’Urso, V. Antonucci, and A. S. Aricò, *Electrochim. Acta* **54**, 6292 (2009) (cit. on p. **2**).
- [29] P. Mazúr, J. Polonský, M. Paidar, and K. Bouzek, *Int. J. Hydrogen Energy* **37**, 12081 (2012) (cit. on p. **2**).
- [30] T. Audichon, T. W. Napporn, C. Canaff, C. Morais, C. Comminges, and K. B. Kokoh, *J. Phys. Chem. C* **120**, 2562 (2016) (cit. on pp. **2**, **9**).
- [31] E. Oakton, D. Lebedev, M. Povia, D. F. Abbott, E. Fabbri, A. Fedorov, M. Nachtegaal, C. Copéret, and T. J. Schmidt, *ACS Catal.* **7**, 2346 (2017) (cit. on pp. **2**, **9**).
- [32] S. M. Alia, B. Rasimick, C. Ngo, K. C. Neyerlin, S. S. Kocha, S. Pylypenko, H. Xu, and B. S. Pivovar, *J. Electrochem. Soc.* **163**, F3105 (2016) (cit. on p. **2**).
- [33] M. Bernt and H. A. Gasteiger, *J. Electrochem. Soc.* **163**, F3179 (2016) (cit. on pp. **2**, **9**).
- [34] P. Lettenmeier, J. Majchel, L. Wang, V. A. Saveleva, S. Zafeiratos, E. R. Savinova, J.-J. Gallet, F. Bournel, A. S. Gago, and K. A. Friedrich, *Chem. Sci.* **9**, 3570 (2018) (cit. on p. **2**).

- [35] <https://pmc.unicore.com/en/products/elyst-ir75-0480>, Umicore AG & Co. (cit. on p. 2).
- [36] W. D. Ryden, A. W. Lawson, and C. C. Sartain, *Phys. Rev. B* **1**, 1494 (1970) (cit. on p. 5).
- [37] K. Reuter and M. Scheffler, *Phys. Rev. B* **65**, 035406 (2001) (cit. on pp. 5, 12, 17, 23).
- [38] Y. Ping, G. Galli, and W. A. Goddard III, *J Phys. Chem. C* **119**, 11570 (2015) (cit. on p. 5).
- [39] P. I. Sorantin and K. Schwarz, *Inorg. Chem.* **31**, 567 (1992) (cit. on p. 5).
- [40] S. Cherevko, S. Geiger, O. Kasian, N. Kulyk, J.-P. Grote, A. Savan, B. R. Shrestha, S. Merzlikin, B. Breitbach, A. Ludwig, and K. J. J. Mayrhofer, *Catal. Today* **262**, 170 (2016) (cit. on p. 5).
- [41] R. Kötz, H. J. Lewerenz, and S. Stucki, *J. Electrochem. Soc.* **130**, 825 (1983) (cit. on p. 5).
- [42] E. Fabbri, A. Habereeder, K. Waltar, R. Kötz, and T. J. Schmidt, *Catal. Sci. Technol.* **4**, 3800 (2014) (cit. on p. 5).
- [43] C.-S. Hsieh, D.-S. Tsai, R.-S. Chen, and Y.-S. Huang, *Appl. Phys. Lett.* **85**, 3860 (2004) (cit. on p. 6).
- [44] S.-W. Lee, B. M. Gallant, H.-R. Byon, P. T. Hammond, and Y. Shao-Horn, *Energy Environ. Sci.* **4**, 1972 (2011) (cit. on p. 6).
- [45] M. Min, K. Machida, J.-H. Jang, and K. Naoi, *J. Electrochem. Soc.* **153**, A334 (2005) (cit. on p. 6).
- [46] R.-R. Bi, X.-L. Wu, F.-F. Cao, L.-Y. Jiang, Y.-G. Guo, and L.-J. Wan, *J. Phys. Chem. C* **114**, 2448 (2010) (cit. on p. 6).
- [47] M. Yagi, E. Tomita, and T. Kuwabara, *J. Electroanal. Chem.* **579**, 83 (2005) (cit. on p. 6).
- [48] P. G. Hoertz, Y.-I. Kim, W. J. Youngblood, and T. E. Mallouk, *J. Phys. Chem. B* **111**, 6845 (2007) (cit. on p. 6).
- [49] T. Nakagawa, C. A. Beasley, and R. W. Murray, *J. Phys. Chem. C* **113**, 12958 (2009) (cit. on p. 6).
- [50] Y. Zhao, E. A. Hernandez-Pagan, N. M. Vargas-Barbosa, J. L. Dysart, and T. E. Mallouk, *J. Phys. Chem. Lett.* **2**, 402 (2011) (cit. on p. 6).
- [51] K. Biswas and C. N. R. Rao, *J. Nanosci. Nanotechnol.* **7**, 1969 (2007) (cit. on p. 6).
- [52] D. Weber, L. M. Schoop, D. Wurmbrand, S. Laha, F. Podjaski, V. Duppel, K. Müller, U. Starke, and B. V. Lotsch, *J. Mater. Chem. A* **6**, 21558 (2018) (cit. on p. 6).
- [53] B. Zakeri and S. Syri, *Renew. Sust. Energ. Rev.* **42**, 569 (2015) (cit. on p. 6).
- [54] M. C. Argyrou, P. Christodoulides, and S. A. Kalogirou, *Renew. Sust. Energ. Rev.* **94**, 804 (2018) (cit. on p. 6).
- [55] V. Schröder, B. Emonts, H. Janßen, and H.-P. Schulze, *Chem. Eng. Technol.* **27**, 847 (2004) (cit. on p. 7).

- [56] Q. Shi, C. Zhu, D. Du, and Y. Lin, *Chem. Soc. Rev.* **48**, 3181 (2019) (cit. on p. 7).
- [57] J. Ahn and R. Holze, *J. Appl. Electrochem.* **22**, 1167 (1992) (cit. on p. 7).
- [58] K. E. Ayers, J. N. Renner, N. Danilovic, J. X. Wang, Y. Zhang, R. Maric, and H. Yu, *Catal. Today* **262**, 121 (2016) (cit. on p. 7).
- [59] T. Smolinka, M. Günther, and J. Garche, *Kurzfassung des Abschlussberichtes NOW-Studie, Freiburg im Breisgau* (2011) (cit. on p. 7).
- [60] F. Scheepers, M. Stähler, A. Stähler, E. Rauls, M. Müller, M. Carmo, and W. Lehnert, *Appl. Energy* **283**, 116270 (2021) (cit. on p. 7).
- [61] P. Medina and M. Santarelli, *Int. J. Hydrog. Energy* **35**, 5173 (2010) (cit. on p. 8).
- [62] S. A. Grigoriev, A. A. Kalinnikov, P. Millet, V. I. Porembsky, and V. N. Fateev, *J. Appl. Electrochem.* **40**, 921 (2010) (cit. on p. 8).
- [63] J. Yu, Q. He, G. Yang, W. Zhou, Z. Shao, and M. Ni, *ACS Catal.* **9**, 9973 (2019) (cit. on p. 9).
- [64] A. R. Zeradjanin, A. A. Topalov, Q. Van Overmeere, S. Cherevko, X. Chen, E. Ventosa, W. Schuhmann, and K. J. J. Mayrhofer, *RSC Adv.* **4**, 9579 (2014) (cit. on p. 9).
- [65] S. Trasatti, *Electrochim. Acta* **29**, 1503 (1984) (cit. on p. 9).
- [66] S. Trasatti, *Electrochim. Acta* **36**, 225 (1991) (cit. on p. 9).
- [67] R. Kötz and S. Stucki, *Electrochim. Acta* **31**, 1311 (1986) (cit. on p. 9).
- [68] M. Escudero-Escribano, A. F. Pedersen, E. A. Paoli, R. Frydendal, D. Friebel, P. Malacrida, J. Rossmeisl, I. E. L. Stephens, and I. B. Chorkendorff, *J. Phys. Chem. B* **122**, 947 (2017) (cit. on p. 9).
- [69] J. Tong, Y. Liu, Q. Peng, W. Hu, and Q. Wu, *J. Mater. Sci.* **52**, 13427 (2017) (cit. on p. 9).
- [70] M. Yuan, Y. Zhu, L. Deng, R. Ming, A. Zhang, W. Li, B. Chai, and Z. Ren, *New J. Chem.* **41**, 6152 (2017) (cit. on p. 9).
- [71] B. M. Tackett, W. Sheng, S. Kattel, S. Yao, B. Yan, K. A. Kuttiyiel, Q. Wu, and J. G. Chen, *ACS Catal.* **8**, 2615 (2018) (cit. on p. 9).
- [72] J. O. Bockris, *J. Chem. Phys.* **24**, 817 (1956) (cit. on pp. 9, 10).
- [73] J. Rossmeisl, Z.-W. Qu, H. Zhu, G.-J. Kroes, and J. K. Nørskov, *J. Electroanal. Chem.* **607**, 83 (2007) (cit. on pp. 9, 11–13, 28).
- [74] J.-M. Hu, J.-Q. Zhang, and C.-N. Cao, *Int. J. Hydrog. Energy* **29**, 791 (2004) (cit. on p. 9).
- [75] T. Shinagawa, A. T. Garcia-Esparza, and K. Takanaabe, *Sci. Rep.* **5**, 1 (2015) (cit. on p. 9).
- [76] A. J. Bard, L. R. Faulkner, and H. S. White, *Electrochemical Methods: Fundamentals and Applications* (John Wiley & Sons, 2022) (cit. on p. 9).
- [77] P. Castelli, S. Trasatti, F. H. Pollak, and W. E. O’Grady, *J. Electroanal. Chem. Interf. Electrochem.* **210**, 189 (1986) (cit. on pp. 10, 11).

- [78] J. Rossmeisl, A. Logadottir, and J. K. Nørskov, *Chem. Phys.* **319**, 178 (2005) (cit. on pp. [11](#), [12](#)).
- [79] I. C. Man, H.-Y. Su, F. Calle-Vallejo, H. A. Hansen, J. I. Martinez, N. G. Inoglu, J. Kitchin, T. F. Jaramillo, J. K. Nørskov, and J. Rossmeisl, *ChemCatChem* **3**, 1159 (2011) (cit. on pp. [11](#), [28](#)).
- [80] Y. Ping, R. J. Nielsen, and W. A. Goddard III, *J. Am. Chem. Soc.* **139**, 149 (2017) (cit. on pp. [11–13](#)).
- [81] Z. W. Seh, J. Kibsgaard, C. F. Dickens, I. Chorkendorff, J. K. Nørskov, and T. F. Jaramillo, *Science* **355**, 146 (2017) (cit. on pp. [11](#), [17](#)).
- [82] Z.-J. Zhao, S. Liu, S. Zha, D. Cheng, F. Studt, G. Henkelman, and J. Gong, *Nat. Rev. Mater.* **4**, 792 (2019) (cit. on p. [11](#)).
- [83] D. Opalka, C. Scheurer, and K. Reuter, *ACS Catal.* **9**, 4944 (2019) (cit. on pp. [11](#), [13](#)).
- [84] R. R. Rao, M. J. Kolb, N. B. Halck, A. F. Pedersen, A. Mehta, H. You, K. A. Stoerzinger, Z. Feng, H. A. Hansen, H. Zhou, L. Giordano, J. Rossmeisl, T. Vegge, I. Chorkendorff, I. E. L. Stephens, and Y. Shao-Horn, *Energy Environ. Sci.* **10**, 2626 (2017) (cit. on p. [11](#)).
- [85] T. Binninger and M.-L. Doublet, *Energy Environ. Sci.* **15**, 2519 (2022) (cit. on p. [11](#)).
- [86] K. A. Stoerzinger, L. Qiao, M. D. Biegalski, and Y. Shao-Horn, *J. Phys. Chem. Lett.* **5**, 1636 (2014) (cit. on pp. [11](#), [13](#)).
- [87] R. R. Rao, M. J. Kolb, L. Giordano, A. F. Pedersen, Y. Katayama, J. wang, A. Mehta, H. You, J. R. Lunger, H. Zhou, N. B. Halck, T. Vegge, I. Chorkendorff, I. E. L. Stephens, and Y. Shao-Horn, *Nat. Catal.* **3**, 516 (2020) (cit. on p. [11](#)).
- [88] K. Reuter, *Catal. Lett.* **146**, 541 (2016) (cit. on pp. [12](#), [17](#), [21](#)).
- [89] J. K. Nørskov, J. Rossmeisl, A. Logadottir, L. R. K. J. Lindqvist, J. R. Kitchin, T. Bligaard, and H. Jonsson, *J. Phys. Chem. B* **108**, 17886 (2004) (cit. on pp. [12](#), [17](#), [26](#)).
- [90] N. B. Halck, V. Petrykin, P. Krtil, and J. Rossmeisl, *Phys. Chem. Chem. Phys.* **16**, 13682 (2014) (cit. on pp. [12](#), [28](#)).
- [91] Y.-H. Fang and Z.-P. Liu, *J. Am. Chem. Soc.* **132**, 18214 (2010) (cit. on pp. [12](#), [13](#)).
- [92] J. A. Gauthier, C. F. Dickens, L. D. Chen, A. D. Doyle, and J. K. Nørskov, *J. Phys. Chem. C* **121**, 11455 (2017) (cit. on pp. [12](#), [13](#), [28](#)).
- [93] J. A. Gauthier, S. Ringe, C. F. Dickens, A. J. Garza, A. T. Bell, M. Head-Gordon, J. K. Nørskov, and K. Chan, *ACS Catal.* **9**, 920 (2019) (cit. on p. [12](#)).
- [94] G. Henkelman, B. P. Uberuaga, and H. Jónsson, *J. Chem. Phys.* **113**, 9901 (2000) (cit. on pp. [12](#), [17](#)).
- [95] A. H. Motagamwala and J. A. Dumesic, *Chem. Rev.* **121**, 1049 (2020) (cit. on p. [12](#)).
- [96] C. F. Dickens, C. Kirk, and J. K. Nørskov, *J. Phys. Chem. C* **123**, 18960 (2019) (cit. on pp. [12](#), [13](#)).

- [97] N. Govindarajan, J. M. Garcia-Lastra, E. J. Meijer, and F. Calle-Vallejo, *Curr. Opin. Electrochem.* **8**, 110 (2018) (cit. on p. 12).
- [98] K. S. Exner, *J. Phys. Chem. C* **124**, 822 (2019) (cit. on p. 12).
- [99] K. S. Exner, *ACS Catal.* **9**, 5320 (2019) (cit. on p. 12).
- [100] O. Piqué, F. Illas, and F. Calle-Vallejo, *Phys. Chem. Chem. Phys.* **22**, 6797 (2020) (cit. on p. 12).
- [101] K. S. Exner, *Electrochim. Acta* **375**, 137975 (2021) (cit. on pp. 12, 28).
- [102] S. Ringe, N. G. Hormann, H. Oberhofer, and K. Reuter, *Chem. Rev.* (2021) (cit. on p. 12).
- [103] E. Watanabe, J. Rossmeisl, M. E. Björketun, H. Ushiyama, and K. Yamashita, *J. Phys. Chem. C* **120**, 8096 (2016) (cit. on p. 12).
- [104] L. G. V. Briquet, M. Sarwar, J. Mugo, G. Jones, and F. Calle-Vallejo, *ChemCatChem* **9**, 1261 (2017) (cit. on p. 12).
- [105] D.-Y. Kuo, J. K. Kawasaki, J. N. Nelson, J. Kloppenburg, G. Hautier, K. M. Shen, D. G. Schlom, and J. Suntivich, *J. Am. Chem. Soc.* **139**, 3473 (2017) (cit. on p. 13).
- [106] K. S. Exner and H. Over, *ACS Catal.* **9**, 6755 (2019) (cit. on pp. 13, 28).
- [107] K. S. Exner, I. Sohrabnejad-Eskan, and H. Over, *ACS Catal.* **8**, 1864 (2018) (cit. on p. 13).
- [108] T. Wang, J. Jelic, D. Rosenthal, and K. Reuter, *ChemCatChem* **5**, 3398 (2013) (cit. on pp. 13, 14, 19, 22).
- [109] O. Matz and M. Calatayud, *J. Phys. Chem. C* **121**, 13135 (2017) (cit. on p. 13).
- [110] C. Roy, R. R. Rao, K. A. Stoerzinger, J. Hwang, J. Rossmeisl, I. Chorkendorff, Y. Shao-Horn, and I. E. L. Stephens, *ACS Energy Lett.* **3**, 2045 (2018) (cit. on p. 13).
- [111] G. Ertl, *Reactions at Solid Surfaces* (John Wiley & Sons, 2010) (cit. on p. 13).
- [112] H. Over, *Chem. Rev.* **112**, 3356 (2012) (cit. on p. 13).
- [113] Y. D. Kim, H. Over, G. Krabbes, and G. Ertl, *Top. Catal.* **14**, 95 (2000) (cit. on p. 13).
- [114] H. Over, Y. D. Kim, A. P. Seitsonen, S. Wendt, E. Lundgren, M. Schmid, P. Varga, A. Morgante, and G. Ertl, *Science* **287**, 1474 (2000) (cit. on p. 13).
- [115] Z.-P. Liu, P. Hu, and A. Alavi, *J. Chem. Phys.* **114**, 5956 (2001) (cit. on p. 13).
- [116] H. Over, A. P. Seitsonen, E. Lundgren, M. Schmid, and P. Varga, *J. Am. Chem. Soc.* **123**, 11807 (2001) (cit. on p. 13).
- [117] A. P. Seitsonen, Y. D. Kim, M. Knapp, S. Wendt, and H. Over, *Phys. Rev. B* **65**, 035413 (2001) (cit. on p. 13).
- [118] J. Wang, C. Y. Fan, K. Jacobi, and G. Ertl, *J. Phys. Chem. B* **106**, 3422 (2002) (cit. on p. 13).
- [119] J. Aßmann, E. Löffler, A. Birkner, and M. Muhler, *Catal. Today* **85**, 235 (2003) (cit. on p. 13).

- [120] K. Reuter and M. Scheffler, Phys. Rev. Lett **90**, 046103 (2003) (cit. on pp. [13](#), [14](#)).
- [121] K. Reuter and M. Scheffler, Phys. Rev. B **68**, 045407 (2003) (cit. on pp. [13](#), [14](#), [22](#), [24](#), [30](#)).
- [122] M. Knapp, A. P. Seitsonen, Y. D. Kim, and H. Over, J. Phys. Chem. B **108**, 14392 (2004) (cit. on pp. [13](#), [30](#)).
- [123] H. Over, M. Knapp, E. Lundgren, A. P. Seitsonen, M. Schmid, and P. Varga, ChemPhysChem **5**, 167 (2004) (cit. on p. [13](#)).
- [124] K. Reuter, D. Frenkel, and M. Scheffler, Phys. Rev. Lett. **93**, 116105 (2004) (cit. on p. [13](#)).
- [125] S. Wendt, M. Knapp, and H. Over, J. Am. Chem. Soc. **126**, 1537 (2004) (cit. on p. [13](#)).
- [126] J. Aßmann, D. Crihan, M. Knapp, E. Lundgren, E. Löffler, M. Muhler, V. Narkhede, H. Over, M. Schmid, A. P. Seitsonen, and P. Varga, Angew. Chem. Int. Ed. **44**, 917 (2005) (cit. on pp. [13](#), [14](#), [30](#), [43](#), [44](#)).
- [127] K. Reuter and M. Scheffler, Phys. Rev. B **73**, 045433 (2006) (cit. on pp. [13](#), [14](#), [31](#)).
- [128] M. Rieger, J. Rogal, and K. Reuter, Phys. Rev. Lett. **100**, 016105 (2008) (cit. on p. [13](#)).
- [129] S. Matera and K. Reuter, Phys. Rev. B **82**, 085446 (2010) (cit. on p. [13](#)).
- [130] A. Farkas, F. Hess, and H. Over, J. Phys. Chem. C **116**, 581 (2012) (cit. on p. [13](#)).
- [131] S. Matera, H. Meskine, and K. Reuter, J. Chem. Phys. **134**, 064713 (2011) (cit. on p. [13](#)).
- [132] F. Hess, A. Farkas, A. P. Seitsonen, and H. Over, J. Comput. Chem. **33**, 757 (2012) (cit. on p. [13](#)).
- [133] T. Wang and K. Reuter, J. Chem. Phys. **143**, 204702 (2015) (cit. on p. [13](#)).
- [134] J. I. Flege, J. Lachnitt, D. Mazur, P. Sutter, and J. Falta, Phys. Chem. Chem. Phys. **18**, 213 (2016) (cit. on p. [13](#)).
- [135] J. E. Sutton, J. M. Lorenzi, J. T. Krogel, Q. Xiong, S. Pannala, S. Matera, and A. Savara, ACS Catal. **8**, 5002 (2018) (cit. on p. [13](#)).
- [136] L.-H. Luo, S.-D. Huang, C. Shang, and Z.-P. Liu, ACS Catal. **12**, 6265 (2022) (cit. on p. [13](#)).
- [137] N. W. Cant, P. C. Hicks, and B. S. Lennon, J. Catal. **54**, 372 (1978) (cit. on p. [13](#)).
- [138] H.-I. Lee and J. M. White, J. Catal. **63**, 261 (1980) (cit. on p. [13](#)).
- [139] J. T. Kiss and R. D. Gonzalez, J. Phys. Chem. **88**, 892 (1984) (cit. on p. [13](#)).
- [140] C. H. F. Peden and D. W. Goodman, J. Phys. Chem. **90**, 1360 (1986) (cit. on p. [13](#)).
- [141] C. Stampfl, S. Schwegmann, H. Over, M. Scheffler, and G. Ertl, Phys. Rev. Lett. **77**, 3371 (1996) (cit. on p. [13](#)).
- [142] K. Reuter, C. Stampfl, M. V. Ganduglia-Pirovano, and M. Scheffler, Chem. Phys. Lett. **352**, 311 (2002) (cit. on p. [13](#)).

- [143] H. Over and M. Muhler, *Prog. Surf. Sci.* **72**, 3 (2003) (cit. on p. 14).
- [144] D. Rosenthal, F. Girgsdies, O. Timpe, R. Blume, G. Weinberg, D. Teschner, and R. Schlögl, *Z. Phys. Chem.* **223**, 183 (2009) (cit. on p. 14).
- [145] D. Rosenthal, F. Girgsdies, O. Timpe, G. Weinberg, and R. Schlögl, *Z. Phys. Chem.* **225**, 57 (2011) (cit. on p. 14).
- [146] V. Narkhede, J. Aßmann, and M. Muhler, *Z. Phys. Chem.* **219**, 979 (2005) (cit. on p. 14).
- [147] F. Hess, S. Rohrlack, M. Knapp, and H. Over, *J. Phys. Chem. C* **126**, 946 (2022) (cit. on p. 15).
- [148] R. Schlögl, *Angew. Chem. Int. Ed.* **54**, 3465 (2015) (cit. on p. 17).
- [149] B. W. J. Chen, L. Xu, and M. Mavrikakis, *Chem. Rev.* **121**, 1007 (2020) (cit. on p. 17).
- [150] J. Tersoff and D. R. Hamann, *Phys. Rev. B* **31**, 805 (1985) (cit. on p. 17).
- [151] B. Hammer and J. K. Nørskov, in *Adv. catal.* Vol. 45 (Elsevier, 2000), pp. 71–129 (cit. on p. 17).
- [152] J. Rogal and K. Reuter, *Ab Initio Atomistic Thermodynamics for Surfaces: A Primer*, tech. rep. (2006) (cit. on pp. 17, 24).
- [153] G. Mándi and K. Palotás, *Phys. Rev. B* **91**, 165406 (2015) (cit. on p. 17).
- [154] G. S. Michelitsch and K. Reuter, *J. Chem. Phys.* **150**, 074104 (2019) (cit. on p. 17).
- [155] H. B. Schlegel, *J. Comput. Chem.* **24**, 1514 (2003) (cit. on p. 17).
- [156] D. J. Wales and J. P. K. Doye, *J. Phys. Chem. A* **101**, 5111 (1997) (cit. on p. 17).
- [157] D. J. Wales and H. A. Scheraga, *Science* **285**, 1368 (1999) (cit. on p. 17).
- [158] S. Goedecker, *J. Chem. Phys.* **120**, 9911 (2004) (cit. on p. 17).
- [159] F. Calvo, D. Schebarchov, and D. J. Wales, *J. Chem. Theory Comput.* **12**, 902 (2016) (cit. on p. 17).
- [160] V. L. Deringer, M. A. Caro, and G. Csányi, *Adv. Mater.* **31**, 1902765 (2019) (cit. on pp. 17, 33, 37).
- [161] Y. Zuo, C. Chen, X. Li, Z. Deng, Y. Chen, J. Behler, G. Csányi, A. V. Shapeev, A. P. Thompson, M. A. Wood, and S. P. Ong, *J. Phys. Chem. A* **124**, 731 (2020) (cit. on pp. 17, 33).
- [162] J. Timmermann, Y. Lee, C. G. Staacke, J. T. Margraf, C. Scheurer, and K. Reuter, *J. Chem. Phys.* **155**, 244107 (2021) (cit. on pp. 17, 22, 26, 28, 33, 41–43, 50).
- [163] C. Kittel and P. McEuen, *Introduction to Solid State Physics*, Vol. 8 (Wiley New York, 1996) (cit. on p. 19).
- [164] Z. Łodziana, N.-Y. Topsøe, and J. K. Nørskov, *Nat. Mater.* **3**, 289 (2004) (cit. on p. 20).
- [165] G. Wulff, *Z. Krystallog.* **34**, 449 (1901) (cit. on p. 20).
- [166] Z. Quan, Y. Wang, and J. Fang, *Acc. Chem. Res.* **46**, 191 (2013) (cit. on p. 20).

- [167] J. Su, R. Ge, K. Jiang, Y. Dong, F. Hao, Z. Tian, G. Chen, and L. Chen, *Adv. Mater.* **30**, 1801351 (2018) (cit. on p. 20).
- [168] J. K. Mackenzie, A. J. W. Moore, and J. F. Nicholas, *J. Phys. Chem. Solids* **23**, 185 (1962) (cit. on p. 20).
- [169] S.-H. Yoo, J.-H. Lee, Y.-K. Jung, and A. Soon, *Phys. Rev. B* **93**, 035434 (2016) (cit. on p. 20).
- [170] G. Liu, H. G. Yang, J. Pan, Y. Q. Yang, G. Q. Lu, and H.-M. Cheng, *Chem. Rev.* **114**, 9559 (2014) (cit. on p. 20).
- [171] R. Reske, H. Mistry, F. Behafarid, B. R. Cuenya, and P. Strasser, *J. Am. Chem. Soc.* **136**, 6978 (2014) (cit. on p. 20).
- [172] H. Mistry, R. Reske, Z. Zeng, Z.-J. Zhao, J. Greeley, P. Strasser, and B. R. Cuenya, *J. Am. Chem. Soc.* **136**, 16473 (2014) (cit. on p. 20).
- [173] J. Timmermann, F. Kraushofer, N. Resch, P. Li, Y. Wang, Z. Mao, M. Riva, Y. Lee, C. Staacke, M. Schmid, C. Scheurer, G. S. Parkinson, U. Diebold, and K. Reuter, *Phys. Rev. Lett.* **125**, 206101 (2020) (cit. on pp. 22, 33).
- [174] M. W. Chase, J. F. L. Curnutt, A. T. Hu, H. Prophet, A. N. Syverud, and L. C. Walker, *J. Phys. Chem. Ref. Data* **3**, 311 (1974) (cit. on p. 23).
- [175] K. K. Irikura, *J. Phys. Chem. Ref. Data* **36**, 389 (2007) (cit. on p. 23).
- [176] G. Herzberg, *Molecular Spectra and Molecular Structure* (D. van Nostrand, 1945) (cit. on p. 23).
- [177] Q. Sun, K. Reuter, and M. Scheffler, *Phys. Rev. B* **67**, 205424 (2003) (cit. on p. 24).
- [178] M. Chase, *NIST-JANAF Thermochemical Tables* (American Institute of Physics, 1998) (cit. on p. 27).
- [179] A. F. Pedersen, M. Escudero-Escribano, B. Sebok, A. Bodin, E. Paoli, R. Frydendal, D. Friebel, I. E. L. Stephens, J. Rossmeisl, I. Chorkendorff, and A. Nilsson, *J. Phys. Chem. B* **122**, 878 (2018) (cit. on p. 28).
- [180] R. Kötz, S. Stucki, D. Scherson, and D. M. Kolb, *J. Electroanal. Chem. Interf. Electrochem.* **172**, 211 (1984) (cit. on p. 29).
- [181] J. A. G. Torres, P. C. Jennings, M. H. Hansen, J. R. Boes, and T. Bligaard, *Phys. Rev. Lett.* **122**, 156001 (2019) (cit. on p. 30).
- [182] O.-P. Koistinen, F. B. Dagbjartsdóttir, V. Ásgeirsson, A. Vehtari, and H. Jónsson, *J. Chem. Phys.* **147**, 152720 (2017) (cit. on p. 30).
- [183] E. G. del Río, J. J. Mortensen, and K. W. Jacobsen, *Phys. Rev. B* **100**, 104103 (2019) (cit. on p. 30).
- [184] A. P. Bartók, M. C. Payne, R. Kondor, and G. Csányi, *Phys. Rev. Lett.* **104**, 136403 (2010) (cit. on pp. 33, 37).
- [185] J. Behler, *J. Chem. Phys.* **134**, 074106 (2011) (cit. on p. 33).
- [186] M. Rupp, A. Tkatchenko, K.-R. Müller, and O. A. Von Lilienfeld, *Phys. Rev. Lett.* **108**, 058301 (2012) (cit. on p. 33).

- [187] J. C. Snyder, M. Rupp, K. Hansen, K.-R. Müller, and K. Burke, *Phys. Rev. Lett.* **108**, 253002 (2012) (cit. on p. 33).
- [188] K. Hansen, G. Montavon, F. Biegler, S. Fazli, M. Rupp, M. Scheffler, O. A. Von Lilienfeld, A. Tkatchenko, and K.-R. Müller, *J. Chem. Theory Comput.* **9**, 3404 (2013) (cit. on p. 33).
- [189] F. Brockherde, L. Vogt, L. Li, M. E. Tuckerman, K. Burke, and K.-R. Müller, *Nat. Commun.* **8**, 1 (2017) (cit. on p. 33).
- [190] O. A. Von Lilienfeld, *Angew. Chem. Int. Ed.* **57**, 4164 (2018) (cit. on p. 33).
- [191] J. Schmidt, C. L. Benavides-Riveros, and M. A. L. Marques, *J. Phys. Chem. Lett.* **10**, 6425 (2019) (cit. on p. 33).
- [192] M. Bogojeski, L. Vogt-Maranto, M. E. Tuckerman, K.-R. Müller, and K. Burke, *Nat. Commun.* **11**, 1 (2020) (cit. on p. 33).
- [193] S. Stocker, G. Csányi, K. Reuter, and J. T. Margraf, *Nat. Commun.* **11**, 1 (2020) (cit. on p. 33).
- [194] A. P. Bartók, S. De, C. Poelking, N. Bernstein, J. R. Kermode, G. Csányi, and M. Ceriotti, *Sci. Adv.* **3**, e1701816 (2017) (cit. on p. 33).
- [195] D. Dragoni, T. D. Daff, G. Csányi, and N. Marzari, *Phys. Rev. Mater.* **2**, 013808 (2018) (cit. on p. 33).
- [196] P. Rowe, V. L. Deringer, P. Gasparotto, G. Csányi, and A. Michaelides, *J. Chem. Phys.* **153**, 034702 (2020) (cit. on p. 33).
- [197] R. Jinnouchi, K. Miwa, F. Karsai, G. Kresse, and R. Asahi, *J. Phys. Chem. Lett.* **11**, 6946 (2020) (cit. on p. 33).
- [198] J. Vandermause, S. B. Torrisi, S. Batzner, Y. Xie, L. Sun, A. M. Kolpak, and B. Kozinsky, *npj Comput. Mater.* **6**, 1 (2020) (cit. on p. 33).
- [199] M. K. Bisbo and B. Hammer, *Phys. Rev. Lett.* **124**, 086102 (2020) (cit. on p. 33).
- [200] C. Verdi, F. Karsai, P. Liu, R. Jinnouchi, and G. Kresse, *npj Comput. Mater.* **7**, 1 (2021) (cit. on p. 33).
- [201] S. Kaappa, E. G. del Rio, and K. W. Jacobsen, *Phys. Rev. B* **103**, 174114 (2021) (cit. on p. 33).
- [202] V. L. Deringer, A. P. Bartók, N. Bernstein, D. M. Wilkins, M. Ceriotti, and G. Csányi, *Chem. Rev.* **121**, 10073 (2021) (cit. on pp. 33–36, 38, 39, 41).
- [203] E. Schulz, M. Speekenbrink, and A. Krause, *J. Math. Psychol.* **85**, 1 (2018) (cit. on p. 34).
- [204] M. W. Mahoney and P. Drineas, *Proc. Natl. Acad. Sci. U. S. A.* **106**, 697 (2009) (cit. on p. 35).
- [205] A. P. Bartók, R. Kondor, and G. Csányi, *Phys. Rev. B* **87**, 184115 (2013) (cit. on pp. 36, 37).
- [206] F. Musil, A. Grisafi, A. P. Bartók, C. Ortner, G. Csányi, and M. Ceriotti, *Chem. Rev.* **121**, 9759 (2021) (cit. on p. 36).

- [207] V. L. Deringer and G. Csányi, Phys. Rev. B **95**, 094203 (2017) (cit. on pp. 38, 39).
- [208] D. J. C. MacKay, *Information Theory, Inference and Learning Algorithms* (Cambridge university press, 2003) (cit. on p. 39).
- [209] <https://github.com/libAtoms/universalSOAP>, UniversalSOAP (cit. on p. 42).

Appendices

A Publications	67
A.1 Ruthenium Oxide Nanosheets for Enhanced Oxygen Evolution Catalysis in Acidic Medium	67
A.2 Epitaxial Core-Shell Oxide Nanoparticles: First-Principles Evidence for Increased Activity and Stability of Rutile Catalysts for Acidic Oxygen Evolution	76

A Publications

A.1 Ruthenium Oxide Nanosheets for Enhanced Oxygen Evolution Catalysis in Acidic Medium

Sourav Laha, Yonghyuk Lee, Filip Podjaski, Daniel Weber, Viola Duppel, Leslie M. Schoop, Florian Pielhofer, Christoph Scheurer, Kathrin Müller, Ulrich Starke, Karsten Reuter and Bettina V. Lotsch
Adv. Energy Mater. 9, 1803795 (2019)
DOI: [10.1002/aenm.201803795](https://doi.org/10.1002/aenm.201803795)

Ruthenium Oxide Nanosheets for Enhanced Oxygen Evolution Catalysis in Acidic Medium

Sourav Laha, Yonghyuk Lee, Filip Podjaski, Daniel Weber, Viola Duppel, Leslie M. Schoop, Florian Pielhofer, Christoph Scheurer, Kathrin Müller, Ulrich Starke, Karsten Reuter, and Bettina V. Lotsch*

The fabrication of highly active and robust hexagonal ruthenium oxide nanosheets for the electrocatalytic oxygen evolution reaction (OER) in an acidic environment is reported. The ruthenate nanosheets exhibit the best OER activity of all solution-processed acid medium electrocatalysts reported to date, reaching 10 mA cm^{-2} at an overpotential of only $\approx 255 \text{ mV}$. The nanosheets also demonstrate robustness under harsh oxidizing conditions. Theoretical calculations give insights into the OER mechanism and reveal that the edges are the origin of the high OER activity of the nanosheets. Moreover, the post OER analyses indicate, apart from coarsening, no observable change in the morphology of the nanosheets or oxidation states of ruthenium during the electrocatalytic process. Therefore, the present investigation suggests that ruthenate nanosheets are a promising acid medium OER catalyst with application potential in proton exchange membrane electrolyzers and beyond.

1. Introduction

Sunlight-driven electrochemical splitting of water into hydrogen and oxygen is considered to be one of the most promising approaches to realize a clean and renewable energy economy while taking advantage of already existing infrastructure.^[1] The electrochemical water splitting reaction ($2\text{H}_2\text{O} + \Delta E \rightarrow 2\text{H}_2 + \text{O}_2$) evolves molecular hydrogen and oxygen at the cathode and anode, respectively.^[2] The process is limited by the slow reaction kinetics and large overpotential of the oxygen evolution reaction (OER). H_2 can be evolved relatively efficiently, but full water splitting applications are currently not economically feasible due to the difficulties within the OER process. Unlike hydrogen evolution, which involves transfer of two electrons, it

requires four electrons, under high oxidative potential, to evolve oxygen.^[1b,2,3]

An increasingly large number of oxides, hydroxides, layered double hydroxides (LDHs), chalcogenides, pnictides, organometallics, and nonmetals have been reported as promising candidates for catalyzing OER in alkaline medium.^[4] However, the alkaline electrolytes have relatively low ionic conductivity^[5] and are susceptible to accumulate carbonate as a contaminant by the reaction with carbon dioxide.^[6] Therefore, due to the higher ionic conductivity and fewer side reactions, proton exchange membranes (PEM) and acid solutions have been considered as electrolytes for application in various energy conversion devices such as PEM electrolyzers and reversible fuel cells.^[6,7] In an acidic environment, however, only a limited number of OER catalysts are known to operate in a stable way.^[4a,b]

Ruthenium and iridium metals and their oxides are the best OER catalysts that show good stabilities in acidic environments.^[8] While iridium oxides are more robust, ruthenium oxides exhibit better performance.^[8,9] Therefore, there have been ongoing efforts to discover new iridium and ruthenium-based OER catalysts with similar or improved catalytic activities, yet at reduced precious metal content. This has already led to the development of several single-phase and multiphase oxides such as double perovskites $\text{Ba}_2\text{M}\text{IrO}_6$ ($M = \text{Y}, \text{La}, \text{Ce}, \text{Pr}, \text{Nd}, \text{and Tb}$),^[10] pyrochloros $\text{Y}_2\text{Ir}_2\text{O}_7$,^[11] $\text{Y}_2[\text{Y}_x\text{Ru}_{2-x}]\text{O}_{7-y}$,^[12]

Dr. S. Laha, F. Podjaski, Dr. D. Weber,^[†] V. Duppel, Prof. L. M. Schoop,^[††] Dr. F. Pielhofer,^[†††] Dr. K. Müller, Prof. U. Starke, Prof. B. V. Lotsch
Max Planck Institute for Solid State Research
Heisenbergstrasse 1, 70569 Stuttgart, Germany
E-mail: b.lotsch@fkf.mpg.de

Y. Lee, Dr. C. Scheurer, Prof. K. Reuter
Department of Chemistry
Chair of Theoretical Chemistry and Catalysis Research Center
Technische Universität München
Lichtenbergstraße 4, 85748 Garching, Germany

F. Podjaski
Ecole Polytechnique Fédérale de Lausanne
Station 12, 1015 Lausanne, Switzerland
Dr. D. Weber,^[†] Prof. B. V. Lotsch
Ludwig-Maximilians-Universität München
Butenandtstraße 5-13, 81377 Munich, Germany

Prof. B. V. Lotsch
Nanosystems Initiative Munich (NIM), e-conversion and
Center for Nanoscience (CeNS)
Schellingstraße 4, 80799 Munich, Germany

 The ORCID identification number(s) for the author(s) of this article can be found under <https://doi.org/10.1002/aenm.201803795>.

^[†]Present address: Ohio State University, Columbus, OH 43210, USA

^[††]Present address: Department of Chemistry, Princeton University, Princeton, New Jersey 08540, USA

^[†††]Present address: Institute of Inorganic Chemistry, University of Regensburg, Universitätsstraße 31, 93040 Regensburg, Germany

DOI: 10.1002/aenm.201803795

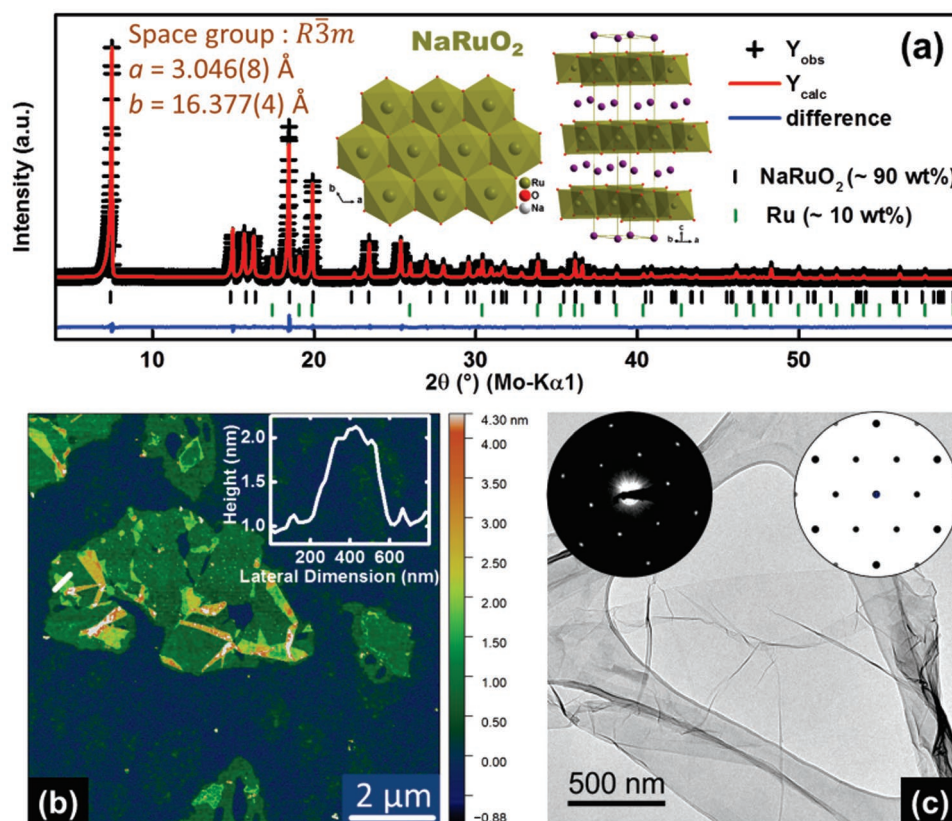


Figure 1. a) Rietveld refinement on the PXRD (Mo-K α 1) data of NaRuO₂; the crystal structure of NaRuO₂ is also shown in the inset. b) AFM image and height profile taken along the white line of the exfoliated nanosheets. c) TEM image and (in inset) the experimental (left) and simulated (right) SAED patterns of a nanosheet along the [001] zone axis.

Y₂Ru₂O_{7- δ} ,^[13] and IrO_x/SrIrO₃.^[14] Several strategies such as the synthesis of bimetallic oxides (Ir_{0.7}Ru_{0.3}O₂),^[15] the investigation of catalytic activities of different crystallographic orientations,^[16] or activity enhancement and precious metal content reduction through exploiting nanostructures with a high degree of surface or edge sites and strains have been investigated to increase the OER catalytic activities.^[8b,9a,17] Mass selected rutile RuO₂ nanoparticles, which are prepared by magnetron sputtering with well-defined shapes and small sizes (2–9 nm in diameter), exhibit one order of magnitude higher catalytic (mass) activity than RuO₂ nanoparticles prepared by chemical methods.^[18] However, it is difficult to obtain such nanoparticles on a large scale.

2D nanosheets of LDHs and hybrid films such as composites of graphitic-C₃N₄ and Ti₃C₂ have been explored for enhanced OER catalysis in basic medium.^[19] So far, the investigation of 2D nanosheets as OER catalysts in acidic medium is limited to iridium oxide and rutile type ruthenium oxide nanosheets.^[20] Toward this end, we have explored the OER catalytic activities of exfoliated hexagonal ruthenate nanosheets, which are reported for the first time. The exfoliated nanosheets were deposited on etched Ti plates in a dimensionally stable anode (DSA) setup that is similar to the electrodes applied in industrial applications. The OER catalytic activities were studied by cyclic voltammetry (CV) as well as chronopotentiometry.

2. Results and Discussion

2.1. Structure and Morphology

The nanosheets were prepared by exfoliation of proton exchanged NaRuO₂ as described in the literature (see Supporting Information for detail).^[21] In brief, a mixture of Na₂CO₃:Ru:RuO₂ = 2:1:3 was heated at 900 °C for 12 h under the constant flow of Ar to obtain NaRuO₂ with a small amount of unreacted Ru (Figure 1a and Figure S1, Supporting Information). NaRuO₂ crystallizes in the α -NaFeO₂ structure with space group $R\bar{3}m$ (no. 166) ($a = 3.046(8)$ Å, $c = 16.377(4)$ Å). The resulting mixture was directly treated with 1 M HCl solution for five days to obtain a mixture of H_xRuO₂· γ H₂O and Ru (Figures S2 and S3, Supporting Information). The proton exchanged sample was then shaken in 0.05 M tetrabutylammonium hydroxide (TBAOH) solution (H:TBAOH = 1:5) for 10 days to obtain a stable dark green colored colloidal suspension of nanosheets. The unexfoliated residues, unreacted Ru, and excess TBAOH were separated by repeated centrifugations. Atomic force microscopy (AFM) on the nanosheets (Figure 1b) indicated the thickness of the nanosheets to be around 1.0 nm, which agrees well with the literature.^[21] As increasing oxidation states of ruthenium lead to decreased OER activity^[5] and fast chemical degradation,^[22] the oxidative deintercalation of sodium with aqueous Na₂S₂O₈ was skipped

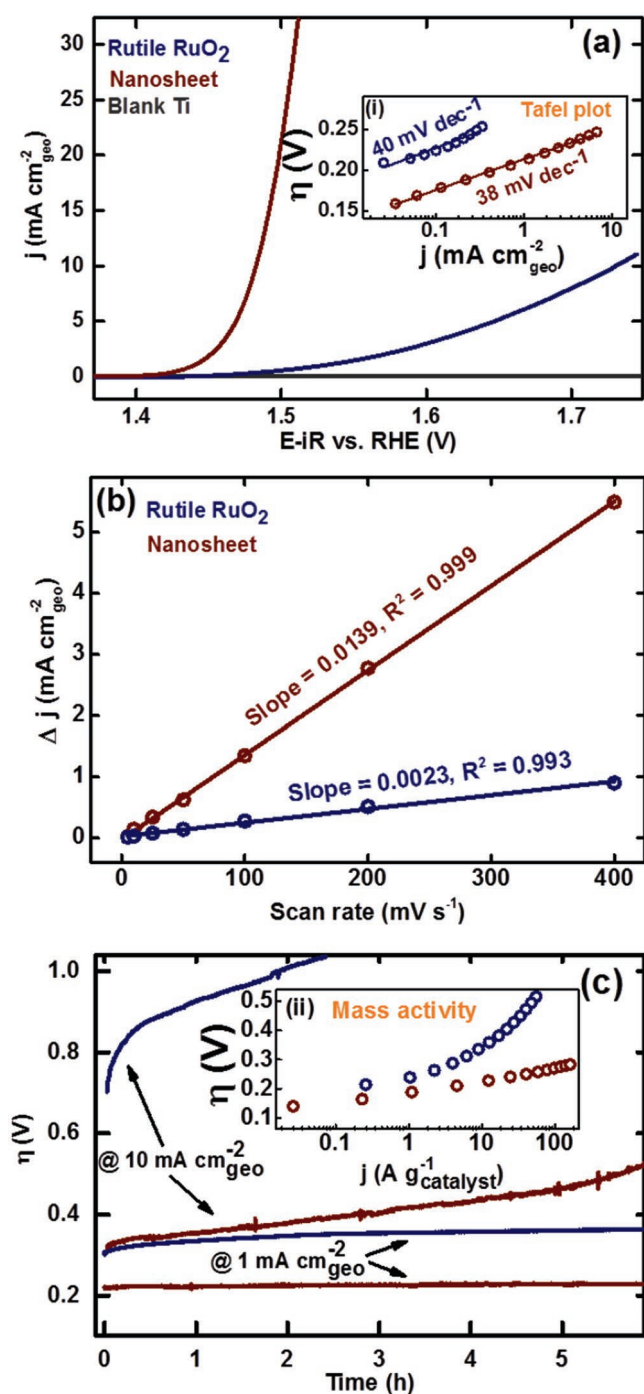


Figure 2. OER catalytic performance of the ruthenate nanosheets and reference rutile RuO₂ on etched Ti-plates in 0.1 M HClO₄. a) Current density (j) versus potential curve @ 10 mV sec⁻¹; inset (i) Tafel plot extracted from (a). b) The difference of charging current densities ($\Delta j = j_a - j_c$) versus scan rates and c) the chronopotentiometric stability; inset (ii) mass activity.

to avoid substantial oxidation of Ru(III) to Ru(IV). However, X-ray photoelectron spectroscopy (XPS) on the nanosheets reveals (Figure S4, Supporting Information) partial oxidation of Ru(III) to Ru(IV) during the proton exchange or/and exfoliation process.

The nanosheets could be observed directly by transmission electron microscopy (TEM). A representative TEM image of the exfoliated ruthenate nanosheets is presented in Figure 1c. The nanosheets are translucent toward the electron beam, indicating the thin nature of the sample.^[19a] The in-plane hexagonal structure of the RuO₂-layers of NaRuO₂ (space group $R\bar{3}m$, $a = 3.046$ Å) is retained in the proton-bearing nanosheets, but the stacking order changes. Based on density functional theory (DFT), three different stacking types were probed. A model based on the bulk crystal structure of IrOOH (space group $P\bar{3}m1$, no. 164)^[23] with AA stacking rather than ABC stacking as in NaRuO₂ yields excellent agreement between the experimental and simulated selected area electron diffraction (SAED) patterns of a few-layer sheet, viewed along the [001] zone axis (Figure 1c).

2.2. OER Catalytic Activity

The electrochemical OER catalytic activities of the nanosheets were investigated by depositing the exfoliated nanosheets on Ti-plates in the DSAs (see Supporting Information for detail). Three different sets of nanosheet loadings (≈ 0.07 , ≈ 0.2 , and ≈ 0.5 mg cm⁻²) were tested initially (Figure S5, Supporting Information). As 0.2 mg cm⁻² of nanosheet loading exhibited the best catalytic activity, further investigations were performed with this optimum loading. Commercial rutile RuO₂ powder was employed as the reference electrocatalyst and tested under the same (0.2 mg cm⁻²) conditions (Figure 2).

Figure 2a shows the current density (j) versus potential curve (@ 10 mV s⁻¹, current density is based on geometric area of the electrode). The corresponding Tafel plot and mass activity are also presented in the insets. To achieve current densities of 1 and 10 mA cm⁻², which represent the current density region required for an efficient solar water splitting device,^[24] the nanosheets have an overpotential of ≈ 215 and ≈ 255 mV, respectively. These values are significantly lower than that of rutile RuO₂. The current density at $\eta = 250$ mV for the nanosheets is ≈ 9.5 mA cm⁻². These low overpotential values for the nanosheets compared to other noble metal-based catalysts (Table S1, Supporting Information), coupled with small Tafel slopes of 38 mV decade⁻¹, are promising for efficient OER applications.

The electrochemical results illustrate that ruthenate nanosheets exhibit an almost three orders of magnitude improved current density (≈ 9.5 mA cm⁻²; 0.2 mg cm⁻² loading, etched Ti plate DSA electrode) at $\eta = 250$ mV compared to the rutile RuO₂ nanoparticles (≈ 10 μ A cm⁻²; 0.05 mg cm⁻² loading, glassy carbon rotating disc electrode) in the same electrolyte.^[9a] The significantly lower charge transfer resistance of the ruthenate nanosheets in the electrochemical impedance spectra (Figure S6, Supporting Information) indicates that the nanosheets have better catalytic charge transfer properties than rutile RuO₂.

Next, the iR -corrected catalytic currents were normalized to the amount of deposited nanosheets to obtain mass activities (inset (ii) of Figure 2). To reach 10 A g⁻¹ (mass activity), the nanosheets require an overpotential η of 225 mV (343 mV for rutile RuO₂). At $\eta = 250$ mV, the electrode reaches ≈ 42 A g⁻¹, which is almost four times that of rutile RuO₂ nanoparticles (11 A g⁻¹) and more than 20 times higher than the mass

normalized current density of rutile RuO₂ (1.8 A g⁻¹). These are among the best values reported in the literature.^[9a,25] These enhanced activities, most probably, arise from an increased number of active sites in a sheet structure or a significantly reduced overpotential at the active sites of the nanosheets compared to bulk material. The large number of surface and edge sites is known to contribute to higher OER activities in N-doped and Ar-etched CoFe LDH nanosheets in basic medium.^[19c,d] In addition, recent studies on Ir-Ni mixed oxide OER catalysts point to the important mechanistic role of surface hydroxyl groups in the water oxidation process, the number of which is significantly increased in the ruthenate nanosheets as compared to RuO₂ nanoparticles (*vide infra*).^[26]

The OER activities of the ruthenate nanosheets and rutile RuO₂ were compared also by investigating the electrochemical surface areas (ECSA). The ECSA was determined from the electrochemical double layer capacitance (C_{dl}) (Figure 2b). The slope of the capacitive current versus scan rate (Figures S7 and S8, Supporting Information), equivalent to twice the C_{dl}, was used to compare the ECSA.^[19a] These data suggest that the ECSA, which is six times higher for the ruthenate nanosheets than rutile RuO₂, is one of the contributors to the enhanced activity of the nanosheets.

2.3. Long-term Stability and Post-catalytic Characterization

The long-term stability (Figure 2c and Figure S9, Supporting Information) of the nanosheets was investigated by means of chronopotentiometry and cycling stability. The chronopotentiometry (Figure 2c) at constant current densities of 1 and 10 mA cm⁻² are recorded for more than 6 h. While the overpotential @ 1 mA cm⁻² for rutile RuO₂ is ≈300 mV, it is ≈220 mV in the case of the nanosheets. For a current density of 10 mA cm⁻², the value increases from ≈260 to ≈520 mV for the nanosheets within the measurement time, whereas the value for rutile RuO₂ increases from ≈700 to more than 1000 mV in less than 2 h. The observed decay is caused by the physical detachment of the nanosheets from the electrode surface due to the high rate of oxygen bubble formation at the DSAs, along with partial dissolution of ruthenium into the electrolyte which leads to coarsening of the nanosheets (see below). These observations are supported by inductively coupled plasma optical emission spectroscopy (ICP-OES) on the post-chronopotentiometric electrolyte (at 10 mA cm⁻² for 6 h) (Table S2, Supporting Information). The cycling stability (Figure S9, Supporting Information) was tested with a scan rate of 25 mV sec⁻¹ for the 1st and 1000th cycles and with 100 mV sec⁻¹ for the intermediate cycles. The high activity of the ruthenate nanosheets changes only marginally (η @10 mA cm⁻² increases from 260 to 266 mV from the 1st to 1000th cycle) compared to rutile RuO₂ during the process. Note that fast decay in the OER performance is a common problem observed in ruthenium-based catalysts, but alleviated here to a large extent by the robustness of the deposited nanosheet film.^[9b,27]

To monitor the chemical stability of the nanosheets during OER in more detail, XPS (Figure 3 and Figure S4, Supporting Information) was performed on the ruthenate nanosheets (as-exfoliated, pre- and post-catalysis (after 1000 cycle CVs)). The Ru 3d_{5/2} spectra of the pre- and post-catalysis samples (Figure 3)

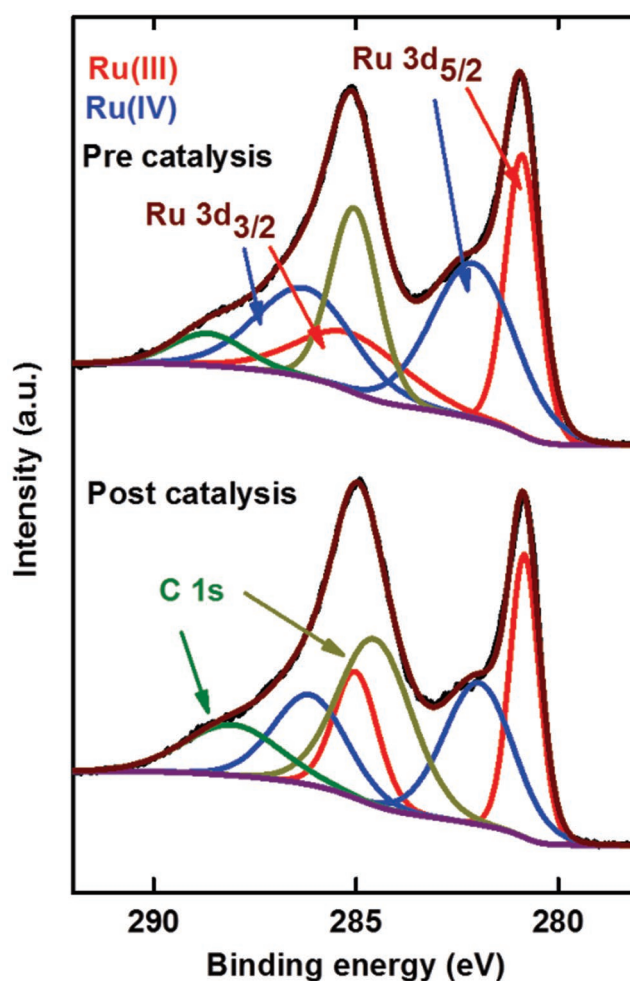


Figure 3. Ru 3d and C 1s core level XPS spectra of pre-catalysis (top) and post-catalysis (after 1000 cycle CVs) (bottom) ruthenate nanosheets. The red lines correspond to Ru(III) and blue lines to Ru(IV).

can clearly be resolved into two peaks with binding energies around 281 and 282 eV, respectively. The peak at around 282 eV can be assigned to Ru(IV),^[28] whereas the lower binding energy peak (≈281 eV) most likely arises from the presence of lower valent Ru(III) in the samples. The coexistence of Ru(III) and Ru(IV) agrees well with the earlier report where the ruthenate nanosheets were formulated as [Ru^{3.8+}O₂]^{0.2-}.^[21] The fact that we do not observe significant changes in the Ru 3d peaks before and after catalysis suggests that a similar chemical and structural environment is retained. The Ru 3d_{3/2} spectra overlap with the C 1s region. The lower binding energy peak of the C (≈285 eV) is likely due to C–C and C–H compounds, whereas the higher binding energy peak (≈289 eV) is due to C–O compounds. These peaks can be assigned to the adventitious carbon adsorbed on the samples during electrode preparation.

To further probe possible changes in morphology or phase transformations during electrode preparation or catalysis, TEM and scanning electron microscopy (SEM) images were recorded on the pre-catalysis and post-catalysis (after 1000 cycle CVs and chronopotentiometry @10 mA cm⁻² for 6 h) electrodes (Figure 4 and Figures S10, S11, and S12, Supporting

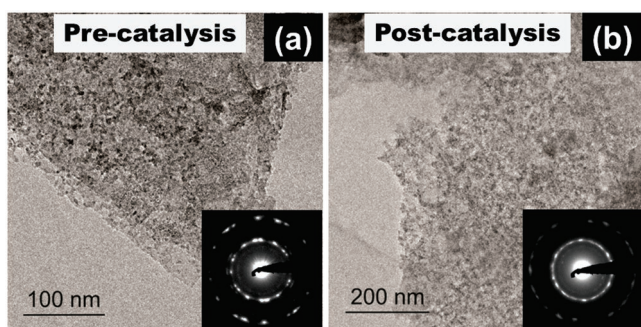


Figure 4. TEM image and SAED pattern of the particles scratched off a) the pre-catalysis electrode and b) the post-catalysis electrode (after 1000 cycle CVs).

Information). The SEM images of the pre-catalysis electrodes (Figure S10, Supporting Information) show a film formed by a random distribution of the restacked nanosheets on the Ti-plates (as expected from the drop casting method). The SEM images obtained from the post-catalysis electrodes (Figures S11 and S12, Supporting Information) indicate that the nanosheets retain their morphology during the electrocatalytic processes though some signatures of cracks are observed. The TEM

images on the scratched-off particles obtained from the pre-catalysis electrodes (Figure 4a) are similar to the post-catalysis (Figure 4b) electrodes. Apart from the rings which appear from the randomly restacked nanosheets, the SAED patterns of the pre- and post-catalysis samples are both consistent with that of the ruthenate nanosheets and the simulated SAED pattern shown in Figure 1c. These results suggest that besides partial detachment/dissolution, the nanosheets retain their local and long-range structure as well as their nanosheet character without undergoing significant transformation during OER in 0.1 M HClO₄.

2.4. Theoretical Analysis and Mechanism

Ab initio thermodynamics on the basis of DFT calculations was applied to first determine the most stable termination of the surface of the ruthenate nanosheets as a function of the applied potential. On the planar surface, H atoms adsorb preferentially atop of the threefold-coordinated oxygen atoms (O^{3f}). A symmetric two-nanosheet model (Figure 5c) allows us to investigate both the stability of hydrogen at the outer surface and at the interface between the sheets. Within the employed (2 × 2) supercells, there are four O^{3f} atoms at the outer surface

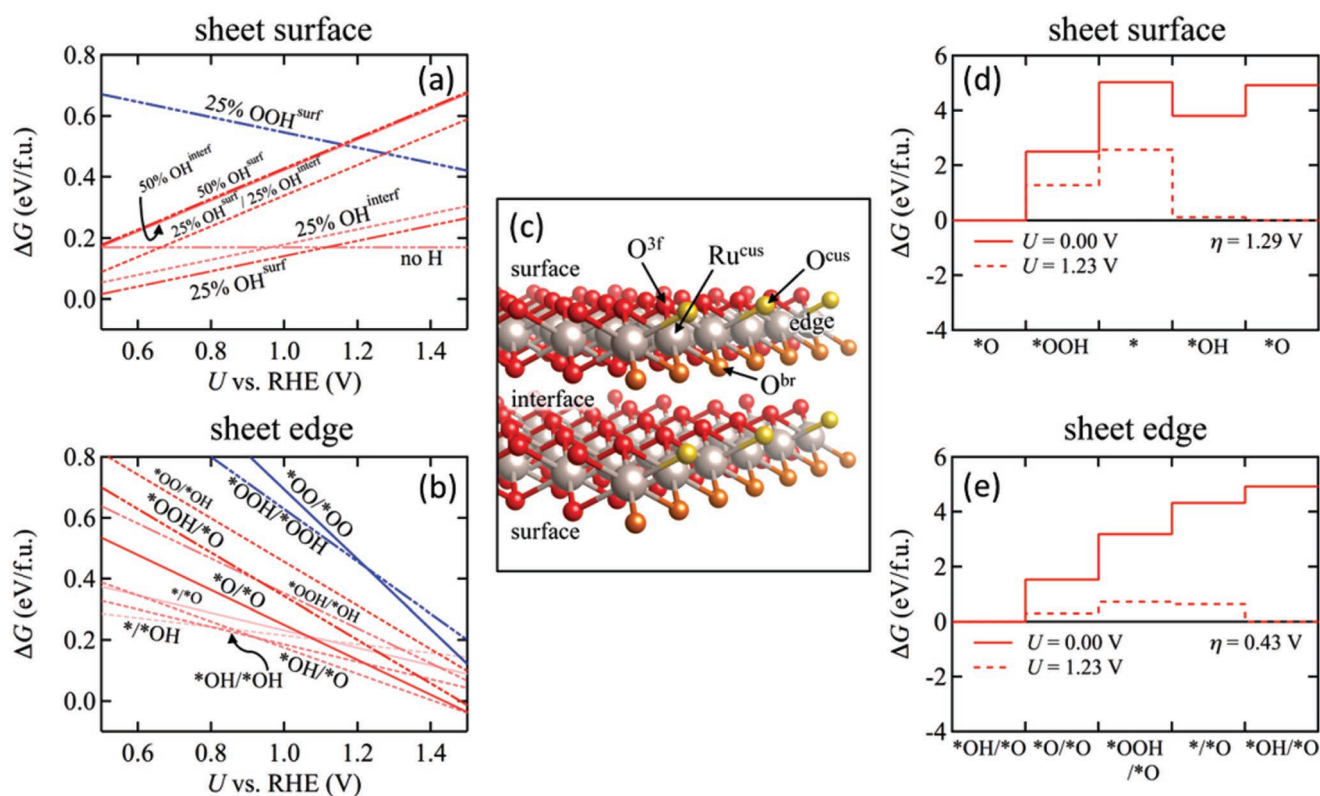
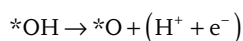
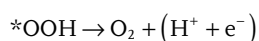


Figure 5. a) Phase diagrams showing the stability of different terminations of the sheet surface and b) of the sheet edge as a function of the applied potential U (vs RHE). See text for the employed nomenclature to describe the different coverages and surface species. c) Perspective view of the two-nanosheet system employed in the calculations. Highlighted are the threefold-coordinated O^{3f} atoms on the sheet surface, as well as the twofold-coordinated bridging O^{br} and onefold-coordinated terminal O^{cus} species that exist at the sheet edge. d) Free energy change along the classic DFT OER pathway for the 3f site at the sheet surface and e) for the Ru^{cus} site at the sheet edge. See text for the four subsequent proton-coupled electron transfer steps involved in this pathway. Shown is the energy profile at open-circuit conditions ($U = 0$ V, solid line) and at the OER equilibrium potential ($U = 1.23$ V, dashed line). Additionally indicated is the minimum overpotential (η) required to make all four steps exergonic.

and four O^{3f} atoms at the inner face between the sheets, which allows assessing H coverages in 25% steps at both O^{3f} types. All possible combinations from 0% to 100% H coverages both at surface and interface regions, corresponding to RuOOH_x with $x = 0, 0.5, 1.0,$ and $2,$ have been explored. The determined relative stabilities of the energetically most preferable terminations are plotted in Figure 5a. As expected, hydrogen-containing terminations, corresponding to lower valence states of Ru, become less favorable with increasing potential. Above a potential of 1.12 V versus RHE, i.e., already below the OER equilibrium potential of 1.23 V, the purely O termination without any hydroxyl groups becomes most stable. Intriguingly, higher oxidized surface terminations with adsorbed hydroperoxo (OOH) or superoxo (OO) groups are very unfavorable at the nanosheet surface, cf. the blue line depicting the 25% OOH covered sheet in Figure 5a. This is in strong contrast to the situation at rutile RuO₂ surfaces, where such higher oxidation intermediates at the surface are much more stable and correspondingly dominate the resting state of the surface even in the OER regime.^[29] We attribute this qualitative difference to the different crystallographic structure of the nanosheet surface and the low-index facets of rutile, in particular to the much studied (110) facet. At the nanosheet surface all O atoms are threefold coordinated and therefore much less reactive than the twofold-coordinated bridging O^{br} or onefold-coordinated terminal O^{cus} oxygen species present in rutile. In addition, in particular at the rutile (110) surface the trenchlike structure with protruding O^{br} rows allows to further stabilize OOH and OO groups adsorbed at the lower so-called coordinatively unsaturated (cus) sites through hydrogen-bridge bonds.^[29]

The low stability of the peroxo species disfavors any OER mechanism at the nanosheet surface involving this species. Figure 5d illustrates this with the reaction energetics along the classic DFT peroxide pathway suggested by Rossmeisl et al.^{[30]:}



Here, we considered the oxygen-terminated sheet as the initial resting state of the surface as this was determined as most stable termination at OER potentials in the phase diagram above. The minimum overpotential η required to make all four proton-coupled electron transfer steps in this mechanism at least exergonic is 1.29 V and therefore much too high to rationalize the experimental observations. Similarly, the very high binding energy of the threefold-coordinated O^{3f} atoms at the ideal surface of the sheet leads to equally high overpotentials for any kind of oxide path that involves the O₂ evolution out of such oxygen species. We therefore conclude that the actual surface of the sheets itself is unlikely the reason for the measured high OER activity. Alternatively, either vacancies or defects in

the sheets or the edges of the sheets could constitute the true active centers, as has recently also been pointed out for single-layer MnO₂.^[31]

We explore this direction by particularly considering edge sites as these offer both lower coordinated bridging (br) and terminal (cus) oxygen adsorption sites similar to rutile as illustrated in Figure 5c. Analogous to the procedure for the nanosheet surface, we first determine the most stable edge termination as a function of applied potential. For this, we use a periodic supercell in which the edges of repeating ribbons representing the ruthenate nanosheets are separated by a 20 Å spacing. Each ribbon is 21 rows wide to decouple its two edges, while a doubled periodicity along the sheet edge allows assessing the stability of OER reaction intermediates at 0%, 50%, and 100% coverages. The nomenclature employed in Figure 5b thus indicates the occupation of the two Ru^{cus} edge sites in the various terminations tested. As apparent, the most stable termination in the OER potential range corresponds to a partially hydroxylated *OH/*O edge structure. However, higher oxidized structures such as *O/*O and *OOH/*O quickly gain stability with increasing potential and start to become most stable at potentials around $U \approx 1.5$ V. As expected from the lower coordination of the edge sites, this is now much more similar to results obtained for the rutile (110) surface by Rao et al.^[29] Nevertheless, highly oxidized edge terminations like fully covered hydroperoxo (*OOH/*OOH) and superoxo (*OO/*OO) are still unfavorable (see blue lines in Figure 5a,b), clearly distinguishing the nanosheet edge from the low-index rutile surfaces. If we thus consider a partially hydroxylated *OH/*O termination as the resting state, we compute a minimum overpotential of only 0.43 V to make all steps of the above described DFT peroxide pathway exergonic, cf. Figure 5e. This is significantly lower than the value found before for the sheet surface and indicates the much higher reactivity in particular of the terminal O^{cus} species at the under coordinated Ru^{cus} edge atoms. The overpotential-determining step in this mechanism is furthermore the second, water-addition step to form surface peroxo, which is fully consistent with the measured Tafel slope of 38 mV decade⁻¹. In contrast, it is important to note that the minimum thermodynamic overpotential determined in the ab initio thermodynamic approach cannot directly be compared to the measured overpotential, but serves only to compare different active site models on a relative scale.^[32] In this respect, the here determined value is at the same level as values determined before for rutile IrO₂(110) and RuO₂(110) models.^[29,33] This confirms the sheet edge as a highly active OER zone, while refined microkinetic studies^[34] are required to quantitatively determine the full mechanism behind the extraordinarily high activity measured for the nanosheets. We speculate that also vacancies or other defects in the surfaces of the sheets are active, likely also partially hydroxylated centers^[26] that further increase the mass activity of the nanosheets.

3. Conclusion

In summary, unprecedented electrocatalytic activity of exfoliated ruthenate nanosheets derived from layered NaRuO₂ is reported for water oxidation in acid medium. The nanosheets exhibit

the highest catalytic activity among all solution-processed state-of-the-art acid medium OER electrocatalysts reported to date, both in terms of specific and mass activities, paired with good cycling and chronopotentiometric stability. Assuming the well-established peroxide pathway, DFT calculations reveal the terminal O^{cus} species at the under coordinated Ru^{cus} edge atoms rather than the threefold-coordinated O^{3f} atoms at the sheet surface as the active sites. In terms of applications, this activity enhancement observed on low loadings of nanosheets goes hand in hand with significant rare metal savings, thus opening new perspectives for a more cost-effective electrode design. XPS analysis in combination with SEM and TEM on the pre- and post-catalysis electrodes/scratched nanosheets exhibits no significant change in oxidation states and structure of the nanosheets, while electrode coarsening during catalysis is observed. The results reported herein thus demonstrate that ruthenate nanosheets are promising candidates for water oxidation in acidic media. The latter is a key requirement for utilization of PEM electrolyzers, which provide higher voltage efficiency and current densities, along with a larger load range and faster system response as compared to alkaline electrolyzers.^[5] Thus, ruthenate nanosheets constitute a new class of OER catalysts combining high activity at minimal mass loadings with good stability under acidic conditions, which are key assets in the design of next-generation electrolyzers for the storage of renewable energy and the production of renewable fuels.

Supporting Information

Supporting Information is available from the Wiley Online Library or from the author

Acknowledgements

The authors thank Marie-Luise Schreiber for inductively coupled plasma optical emission spectroscopy (ICP-OES) measurements and the Computer Service group at MPI-FKF for providing computational facilities. The authors also gratefully acknowledge the financial support by the Max Planck Society, the Nanosystems Initiative Munich (NIM), e-conversion, the Center for Nanoscience (CeNS) and the Kopernikus/P2X programme (Cluster FC-A1) of the German Federal Ministry of Education and Research. Y.L. acknowledges the financial support by Deutscher Akademischer Austauschdienst (DAAD). L.M.S. is grateful to the Minerva Fast Track Fellowship for financial support.

Conflict of Interest

The authors declare no conflict of interest.

Keywords

DFT calculations, electrocatalysis, exfoliation, nanosheets, OER mechanism, oxygen evolution reaction, water splitting

Received: December 8, 2018

Revised: January 6, 2019

Published online:

- [1] a) N. S. Lewis, D. G. Nocera, *Proc. Natl. Acad. Sci. U. S. A.* **2006**, *103*, 15729; b) M. G. Walter, E. L. Warren, J. R. McKone, S. W. Boettcher, Q. Mi, E. A. Santori, N. S. Lewis, *Chem. Rev.* **2010**, *110*, 6446.
- [2] H. Dau, C. Limberg, T. Reier, M. Risch, S. Roggan, P. Strasser, *ChemCatChem* **2010**, *2*, 724.
- [3] Z. W. Seh, J. Kibsgaard, C. F. Dickens, I. Chorkendorff, J. K. Nørskov, T. F. Jaramillo, *Science* **2017**, *355*, eaad4998.
- [4] a) C. C. L. McCrory, S. Jung, I. M. Ferrer, S. M. Chatman, J. C. Peters, T. F. Jaramillo, *J. Am. Chem. Soc.* **2015**, *137*, 4347; b) N.-T. Suen, S.-F. Hung, Q. Quan, N. Zhang, Y.-J. Xu, H. M. Chen, *Chem. Soc. Rev.* **2017**, *46*, 337; c) M. Tahir, L. Pan, F. Idrees, X. Zhang, L. Wang, J.-J. Zou, Z. L. Wang, *Nano Energy* **2017**, *37*, 136.
- [5] T. Reier, H. N. Nong, D. Teschner, R. Schlögl, P. Strasser, *Adv. Energy Mater.* **2017**, *7*, 1601275.
- [6] E. Gülzow, *J. Power Sources* **1996**, *61*, 99.
- [7] K. Sardar, E. Petrucco, C. I. Hiley, J. D. B. Sharman, P. P. Wells, A. E. Russell, R. J. Kashtiban, J. Sloan, R. I. Walton, *Angew. Chem.* **2014**, *126*, 11140.
- [8] a) S. Trasatti, *J. Electroanal. Chem. Interfacial Electrochem.* **1980**, *111*, 125; b) T. Reier, M. Oezaslan, P. Strasser, *ACS Catal.* **2012**, *2*, 1765.
- [9] a) Y. Lee, J. Suntivich, K. J. May, E. E. Perry, Y. Shao-Horn, *J. Phys. Chem. Lett.* **2012**, *3*, 399; b) N. Danilovic, R. Subbaraman, K. C. Chang, S. H. Chang, Y. Kang, J. Snyder, A. P. Paulikas, D. Strmcnik, Y. T. Kim, D. Myers, V. R. Stamenkovic, N. M. Markovic, *Angew. Chem., Int. Ed.* **2014**, *53*, 14016.
- [10] O. Diaz-Morales, S. Raaijman, R. Kortlever, P. J. Kooyman, T. Wezendonk, J. Gascon, W. T. Fu, M. T. M. Koper, *Nat. Commun.* **2016**, *7*, 12363.
- [11] D. Lebedev, M. Povia, K. Waltar, P. M. Abdala, I. E. Castelli, E. Fabbri, M. V. Blanco, A. Fedorov, C. Copéret, N. Marzari, T. J. Schmidt, *Chem. Mater.* **2017**, *29*, 5182.
- [12] J. Park, M. Park, G. Nam, M. G. Kim, J. Cho, *Nano Lett.* **2017**, *17*, 3974.
- [13] J. Kim, P.-C. Shih, K.-C. Tsao, Y.-T. Pan, X. Yin, C.-J. Sun, H. Yang, *J. Am. Chem. Soc.* **2017**, *139*, 12076.
- [14] L. C. Seitz, C. F. Dickens, K. Nishio, Y. Hikita, J. Montoya, A. Doyle, C. Kirk, A. Vojvodic, H. Y. Hwang, J. K. Nørskov, T. F. Jaramillo, *Science* **2016**, *353*, 1011.
- [15] V. A. Saveleva, L. Wang, W. Luo, S. Zafeirotos, C. Ulhaq-Bouillet, A. S. Gago, K. A. Friedrich, E. R. Savinova, *J. Phys. Chem. Lett.* **2016**, *7*, 3240.
- [16] K. A. Stoerzinger, O. Diaz-Morales, M. Kolb, R. R. Rao, R. Frydendal, L. Qiao, X. R. Wang, N. B. Halck, J. Rossmeisl, H. A. Hansen, T. Vegge, I. E. L. Stephens, M. T. M. Koper, Y. Shao-Horn, *ACS Energy Lett.* **2017**, *2*, 876.
- [17] a) D. F. Abbott, D. Lebedev, K. Waltar, M. Povia, M. Nachttegaal, E. Fabbri, C. Copéret, T. J. Schmidt, *Chem. Mater.* **2016**, *28*, 6591; b) D.-Y. Kuo, C. J. Eom, J. K. Kawasaki, G. Petretto, J. N. Nelson, G. Hautier, E. J. Crumlin, K. M. Shen, D. G. Schlom, J. Suntivich, *J. Phys. Chem. C* **2018**, *122*, 4359; c) J. R. Petrie, V. R. Cooper, J. W. Freeland, T. L. Meyer, Z. Zhang, D. A. Lutterman, H. N. Lee, *J. Am. Chem. Soc.* **2016**, *138*, 2488; d) J. R. Petrie, H. Jeon, S. C. Barron, T. L. Meyer, H. N. Lee, *J. Am. Chem. Soc.* **2016**, *138*, 7252; e) J. Hwang, R. R. Rao, L. Giordano, Y. Katayama, Y. Yu, Y. Shao-Horn, *Science* **2017**, *358*, 751.
- [18] E. A. Paoli, F. Masini, R. Frydendal, D. Deiana, C. Schlaup, M. Malizia, T. W. Hansen, S. Horch, I. E. L. Stephens, I. Chorkendorff, *Chem. Sci.* **2015**, *6*, 190.
- [19] a) F. Song, X. Hu, *Nat. Commun.* **2014**, *5*, 4477; b) T. Y. Ma, J. L. Cao, M. Jaroniec, S. Z. Qiao, *Angew. Chem., Int. Ed.* **2016**, *55*, 1138; c) Y. Wang, Y. Zhang, Z. Liu, C. Xie, S. Feng, D. Liu, M. Shao, S. Wang, *Angew. Chem., Int. Ed.* **2017**, *56*, 5867; d) Y. Wang, C. Xie, Z. Zhang, D. Liu, R. Chen, S. Wang, *Adv. Funct. Mater.* **2018**, *28*, 1703363.

- [20] a) D. Takimoto, K. Fukuda, S. Miyasaka, T. Ishida, Y. Ayato, D. Mochizuki, W. Shimizu, W. Sugimoto, *Electrocatalysis* **2017**, *8*, 144; b) D. Takimoto, Y. Ayato, D. Mochizuki, W. Sugimoto, *Electrochemistry* **2017**, *85*, 779; c) D. Weber, L. M. Schoop, D. Wurmbbrand, S. Laha, V. Duppel, F. Podjaski, K. Mueller, U. Starke, B. V. Lotsch, *J. Mater. Chem. A* **2018**, *6*, 21558; d) X. Kong, K. Xu, C. Zhang, J. Dai, S. Norooz Oliae, L. Li, X. Zeng, C. Wu, Z. Peng, *ACS Catal.* **2016**, *6*, 1487.
- [21] K. Fukuda, T. Saida, J. Sato, M. Yonezawa, Y. Takasu, W. Sugimoto, *Inorg. Chem.* **2010**, *49*, 4391.
- [22] H. Over, *Chem. Rev.* **2012**, *112*, 3356.
- [23] D. Weber, L. M. Schoop, D. Wurmbbrand, J. Nuss, E. M. Seibel, F. F. Tafti, H. Ji, R. J. Cava, R. E. Dinnebie, B. V. Lotsch, *Chem. Mater.* **2017**, *29*, 8338.
- [24] S. Haussener, C. Xiang, J. M. Spurgeon, S. Ardo, N. S. Lewis, A. Z. Weber, *Energy Environ. Sci.* **2012**, *5*, 9922.
- [25] a) J. Feng, F. Lv, W. Zhang, P. Li, K. Wang, C. Yang, B. Wang, Y. Yang, J. Zhou, F. Lin, G.-C. Wang, S. Guo, *Adv. Mater.* **2017**, *29*, 1703798; b) T. Kwon, H. Hwang, Y. J. Sa, J. Park, H. Baik, S. H. Joo, K. Lee, *Adv. Funct. Mater.* **2017**, *27*, 1604688; c) Y. Pi, Q. Shao, P. Wang, J. Guo, X. Huang, *Adv. Funct. Mater.* **2017**, *27*, 1700886.
- [26] T. Reier, Z. Pawolek, S. Cherevko, M. Bruns, T. Jones, D. Teschner, S. Selve, A. Bergmann, H. N. Nong, R. Schlögl, K. J. J. Mayrhofer, P. Strasser, *J. Am. Chem. Soc.* **2015**, *137*, 13031.
- [27] N. Hodnik, P. Jovanovič, A. Pavlišič, B. Jozinovič, M. Zorko, M. Bele, V. S. Šelih, M. Šala, S. Hočevar, M. Gaberšček, *J. Phys. Chem. C* **2015**, *119*, 10140.
- [28] D. J. Morgan, *Surf. Interface Anal.* **2015**, *47*, 1072.
- [29] R. R. Rao, M. J. Kolb, N. B. Halck, A. F. Pedersen, A. Mehta, H. You, K. A. Stoerzinger, Z. Feng, H. A. Hansen, H. Zhou, L. Giordano, J. Rossmeisl, T. Vegge, I. Chorkendorff, I. E. L. Stephens, Y. Shao-Horn, *Energy Environ. Sci.* **2017**, *10*, 2626.
- [30] J. Rossmeisl, Z. W. Qu, H. Zhu, G. J. Kroes, J. K. Nørskov, *J. Electroanal. Chem.* **2007**, *607*, 83.
- [31] Y.-F. Li, Z.-P. Liu, *J. Am. Chem. Soc.* **2018**, *140*, 1783.
- [32] J. K. Nørskov, J. Rossmeisl, A. Logadottir, L. Lindqvist, J. R. Kitchin, T. Bligaard, H. Jónsson, *J. Phys. Chem. B* **2004**, *108*, 17886.
- [33] a) Y. Ping, R. J. Nielsen, W. A. Goddard, *J. Am. Chem. Soc.* **2017**, *139*, 149; b) Y.-H. Fang, Z.-P. Liu, *J. Am. Chem. Soc.* **2010**, *132*, 18214.
- [34] a) K. Reuter, M. Scheffler, *Phys. Rev. Lett.* **2003**, *90*, 046103; b) C. P. Plaisance, K. Reuter, R. A. van Santen, *Faraday Discuss.* **2016**, *188*, 199; c) C. P. Plaisance, S. D. Beinlich, K. Reuter, *J. Phys. Chem. C* **2018**, <https://doi.org/10.1021/acs.jpcc.8b08549>.

A.2 Epitaxial Core-Shell Oxide Nanoparticles: First-Principles Evidence for Increased Activity and Stability of Rutile Catalysts for Acidic Oxygen Evolution

Yonghyuk Lee, Christoph Scheurer and Karsten Reuter

ChemSusChem 15, e202200015 (2022)

DOI: [10.1002/cssc.202200015](https://doi.org/10.1002/cssc.202200015)

Epitaxial Core-Shell Oxide Nanoparticles: First-Principles Evidence for Increased Activity and Stability of Rutile Catalysts for Acidic Oxygen Evolution

Yonghyuk Lee,^[a, b] Christoph Scheurer,^{*[a, b]} and Karsten Reuter^[a, b]

Due to their high activity and favorable stability in acidic electrolytes, Ir and Ru oxides are primary catalysts for the oxygen evolution reaction (OER) in proton-exchange membrane (PEM) electrolyzers. For a future large-scale application, core-shell nanoparticles are an appealing route to minimize the demand for these precious oxides. Here, we employ first-principles density-functional theory (DFT) and ab initio thermodynamics to assess the feasibility of encapsulating a cheap rutile-structured TiO₂ core with coherent, monolayer-thin IrO₂ or

RuO₂ films. Resulting from a strong directional dependence of adhesion and strain, a wetting tendency is only obtained for some low-index facets under typical gas-phase synthesis conditions. Thermodynamic stability in particular of lattice-matched RuO₂ films is instead indicated for more oxidizing conditions. Intriguingly, the calculations also predict an enhanced activity and stability of such epitaxial RuO₂/TiO₂ core-shell particles under OER operation.

Introduction

Core-shell nanoparticle morphologies are a powerful and frequently pursued concept in heterogeneous catalysis to reduce the demand of precious active materials. Proton-exchange membrane (PEM) water electrolysis^[1] is an eminent application area for this concept. Oxides containing rare Ir and Ru are currently the primary anode electrocatalysts for the oxygen evolution reaction (OER) that exhibit both a reasonably small overpotential and sufficient stability under the harsh acidic PEM operating conditions.^[2,3] Despite the already high efficiency of current generation catalysts, significant further reduction of Ir or Ru mass loading is required when considering that for a prospective hydrogen economy gigantic amounts of electrolysis power will be required.^[3,4] Within the core-shell concept, large research efforts have therefore been undertaken towards dispersing the precious active oxides on a variety of inexpensive core materials comprising abundant metals, their nitrides, carbides or oxides.^[5–10] Generally, though, these have been massively loaded composites with incoherent thick Ir or Ru oxide films or small nanoparticles that use the core material more like a high surface-area support. As one example we

highlight IrO₂ dispersed on TiO₂,^[11–13] as has also already been commercialized in form of the recent Elyst Ir75 0480 catalyst from Umicore.^[13–17]

Titanium dioxide exhibits a stable rutile modification. This motivates the idea to instead pursue epitaxial core-shell nanoparticles with thin coherent films of the equally rutile-structured IrO₂ or RuO₂ enclosing the cheap core material. In this study we explore this idea with detailed first-principles calculations. Analyzing adhesion, strain and surface energies, we show that prevailing gas-phase synthesis protocols will only be able to stabilize thin films in the few-monolayer regime at some low-index facets of TiO₂ for both IrO₂ and RuO₂. This rationalizes in particular the experimentally observed poor wetting behavior of IrO₂ at the prevalent (110) facet of rutile TiO₂ nanoparticles.^[18,19] Under more oxidizing synthesis conditions, growth of coherent shell films should instead be feasible. Corresponding epitaxial core-shell particles would obviously minimize the precious metal demand. However, most intriguingly, our ab initio thermodynamics based results additionally indicate an increased stability of such particles under OER operation conditions, as well as an increased activity. At enhanced stability, increased activity and minimized precious metal content, this suggests epitaxial rutile IrO₂/TiO₂ or RuO₂/TiO₂ core-shell nanoparticles as a promising target for future synthesis or advanced deposition endeavors.

Results and Discussion

Core-shell interface

As starting point of our investigation we report in Table 1 the computed interface formation energies and work of adhesion for epitaxial and stoichiometric IrO₂/TiO₂ and RuO₂/TiO₂ interfaces for all five symmetry inequivalent low-index orientations

[a] Y. Lee, Dr. C. Scheurer, Prof. K. Reuter
Department of Chemistry, Chair of Theoretical Chemistry and Catalysis
Research Center, Technische Universität München
Lichtenbergstraße, 85747 Garching, Germany

[b] Y. Lee, Dr. C. Scheurer, Prof. K. Reuter
Fritz-Haber-Institut der Max-Planck-Gesellschaft
Faradayweg 4–6, 14195 Berlin, Germany
E-mail: scheurer@fhi.mpg.de

Supporting information for this article is available on the WWW under <https://doi.org/10.1002/cssc.202200015>

© 2022 The Authors. ChemSusChem published by Wiley-VCH GmbH. This is an open access article under the terms of the Creative Commons Attribution License, which permits use, distribution and reproduction in any medium, provided the original work is properly cited.

Table 1. Calculated interface formation energies $\gamma_{\text{interf}}^{(hkl)}$ and work of adhesion $W_{\text{adh}}^{(hkl)}$ for all five symmetry-inequivalent low-index orientations (hkl) of epitaxial stoichiometric $\text{IrO}_2/\text{TiO}_2$ and $\text{RuO}_2/\text{TiO}_2$ interfaces.

Facet	$\gamma_{\text{interf}}^{(hkl)}$ [$\text{meV}\text{\AA}^{-2}$]		$W_{\text{adh}}^{(hkl)}$ [$\text{meV}\text{\AA}^{-2}$]	
	$\text{IrO}_2/\text{TiO}_2$	$\text{RuO}_2/\text{TiO}_2$	$\text{IrO}_2/\text{TiO}_2$	$\text{RuO}_2/\text{TiO}_2$
(100)	18	24	−235	−182
(010)/(100)	20	28	−146	−108
(011)/(100)	15	18	−170	−142
(110)	6	23	−130	−101
(111)-t1	10	16	−253	−216
(111)-t2	10	15	−254	−217

of rutile, namely (001), (010)/(100), (011)/(101), (110) and (111). In the case of the (111) facet, there are two possible stoichiometric interfaces denoted as t1 and t2, see Figure S1 in the Supporting Information for a description of all interfacial geometries. In the calculation of $\gamma_{\text{interf}}^{(hkl)}$ according to equation (6) we consistently use the optimized TiO_2 bulk lattice constants in the directions parallel to the interface for all three solid-state terms which fixes the value of $A^{(hkl)}$. This effectively filters out the increasing strain in a coherent MO_2 film of increasing thickness and allows to arrive at a purely interface specific quantity that reflects the intrinsic cost of creating the interface. Compared to other heterostructures^[20,21] all calculated interface formation energies are very small (about one order of magnitude smaller than the surface free energies discussed below) and consistently below $30 \text{ meV}\text{\AA}^{-2}$. This shows the expected propensity to form such interfaces between the lattice-matched oxides.^[22] Simultaneously, we always obtain positive values. Bonding between the two materials is thus less favorable than the bonding within the pure materials, and there is not energetic driving force for interdiffusion. This is consistent with experiments reporting an (entropically driven) solid solution of IrO_2 in TiO_2 only at temperatures above 900 C .^[23] As complementary key quantities, the negative $W_{\text{adh}}^{(hkl)}$ in Table 1 indicate the energy it would cost to separate the formed interface. Also here, using the optimized TiO_2 bulk lattice constants in the directions parallel to the interface for all terms entering Equation (7) yields an interface specific quantity that is independent of the thickness of the shell layer. The large negative values obtained for both $\text{IrO}_2/\text{TiO}_2$ and $\text{RuO}_2/\text{TiO}_2$ designate a strong intrinsic adhesion, with the same trend over the five low-index orientations found for both materials: (111) toughest to break and (010)/(100) and (110) offering weakest adhesion. This trend can be rationalized with the number of bonds formed per surface area, which is the number of broken bonds in the unit cell to divide the interface model into two separate TiO_2 and MO_2 slabs normalized by the interface area. This trend goes as 0.211, 0.191, 0.160, 0.148 and 0.105\AA^{-2} for (111), (001), (011)/(101), (010)/(100) and (110), respectively. Reformulating $W_{\text{adh}}^{(hkl)}$ from Equation (7) in terms of the interface formation energy and the surface free energies of the stoichiometric TiO_2 and MO_2 terminations forming the interface,

$$W_{\text{adh}}^{(hkl)} = \gamma_{\text{interf}}^{(hkl)} - \gamma_{\text{TiO}_2, \text{surf}}^{(hkl), \text{stoich}} - \gamma_{\text{MO}_2, \text{surf}}^{(hkl), \text{stoich}} \quad (1)$$

also allows to trace the consistently stronger adhesion found for the $\text{IrO}_2/\text{TiO}_2$ interface to the higher respective surface free energies of IrO_2 as compared to RuO_2 (see below). Note that at an almost equal cohesive energy of both oxides (computed as -16.95 and -17.16 eV per MO_2 unit at the present DFT Perdew-Burke-Ernzerhof (PBE) functional^[63] level, respectively), this difference arises predominantly from a higher polarizability of the larger Ir ion.^[24]

Consistently offering smaller interface formation energies and stronger adhesion, the analysis up to now would suggest IrO_2 as preferred shell material. However, the focus on the interface specific quantities $\gamma_{\text{interf}}^{(hkl)}$ and $W_{\text{adh}}^{(hkl)}$ disregards the increasing strain that will build up in pseudomorphic shell layers of increasing thickness. To this end, it is important to realize that the lattice mismatch of $\text{RuO}_2\text{-TiO}_2$ and $\text{IrO}_2\text{-TiO}_2$ is quite different for the two main rutile bulk lattice constants, a and c . Along the longer a axis all three materials exhibit almost identical values. With the employed PBE functional this is $a_{\text{TiO}_2} = 4.578 \text{\AA}$ and shorter lattice constants by only -1.1% for both RuO_2 and IrO_2 . In contrast, along the shorter c axis, this mismatch is larger. Specifically, at PBE level $c_{\text{TiO}_2} = 2.955 \text{\AA}$, while RuO_2 and IrO_2 prefer a longer lattice constant by 5.6% and 7.6% , respectively. As a consequence of this anisotropy, hardly any strain will build up at the three interface orientations (001), (011)/(101) and (111), whereas much higher strain will build up at the two other orientations (110) and (010)/(100), see the Supporting Information for a detailed account of all values. While the larger strain for IrO_2 might (partially) scotch the intrinsic advantage of this material in terms of the afore discussed interface specific quantities, we note that much more problematic is the fact that precisely those two orientations that predominantly suffer from strain are those two that offer the weakest intrinsic adhesion anyway, cf. Table 1. This already indicates a high directional dependence of potential core-shell concepts.

Surface effects

For the actual realization of epitaxial core-shell nanoparticles, not only the interface matters. While growth itself is kinetics, there will always be a thermodynamic driving force to expose the material with the lower surface free energy at the shell. To this end, Figure 1 summarizes the calculated surface free energies of all three oxides, IrO_2 , RuO_2 and TiO_2 , in an oxygen

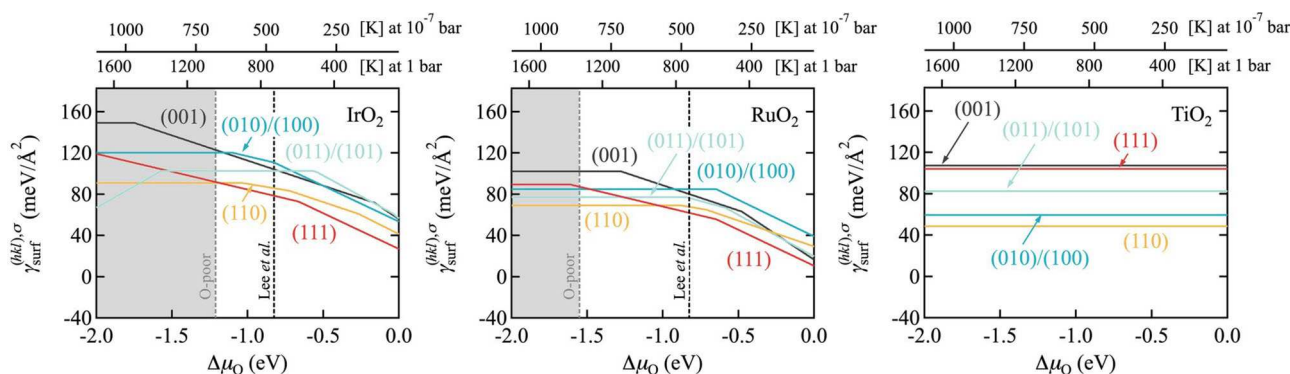


Figure 1. Computed surface free energies $\gamma_{\text{surf}}^{(hkl),\sigma}$ of the five low-index facets of rutile IrO_2 , RuO_2 and TiO_2 in an oxygen environment. Kinks in the individual lines indicate a change of the most stable termination σ , generally going from O-poor terminations (positive slope with respect to oxygen chemical potential $\Delta\mu_{\text{O}}$) over stoichiometric terminations (horizontal lines) to O-rich terminations (negative slope).^[25–27] The vertical gray dotted lines indicate the thermodynamic bulk oxide stability (O-poor limit) as computed from the bulk heat of formation (for TiO_2 this limit is at -3.76 eV outside of the shown range). In the top x axis, the dependence on $\Delta\mu_{\text{O}}$ is translated into a temperature scale at different oxygen pressures. The black vertical dotted line in the phase diagram for IrO_2 and RuO_2 represent the synthesis conditions as employed by Lee et al.^[28]

environment. Equivalent behavior and trends are obtained for the surface free energies in an aqueous environment,^[29] cf. the Supporting Information and below, so that the following analysis conceptually also extends to electrodeposition. Explicitly marked in Figure 1 are the synthesis conditions employed by Lee et al. (1 bar, 500 °C)^[28] to represent typical gas-phase synthesis endeavors. For the corresponding range of O chemical potential, Figure 1 immediately reveals a key bottleneck. The surface free energies of IrO_2 and RuO_2 are generally not smaller than those of TiO_2 , and in particular for the two orientations (010)/(100) and (110) that were already identified as problematic in terms of their interface stability and strain, TiO_2 exhibits

even significantly lower respective $\gamma_{\text{surf}}^{(hkl),\sigma}$ than the intended shell oxides.

All aspects, surface, strain and interface, can be combined in a rough estimate of the wetting tendency. As illustrated in Figure 2, this estimate takes the surface free energy $\gamma_{\text{surf}}^{(hkl),\sigma}$ (1 ML MO_2/TiO_2 , 100%), cf. Equation (9), of a model where a pseudomorphic one monolayer (ML) film of the shell material completely covers the $\text{TiO}_2(hkl)$ surface, and compares it to the surface free energy estimates

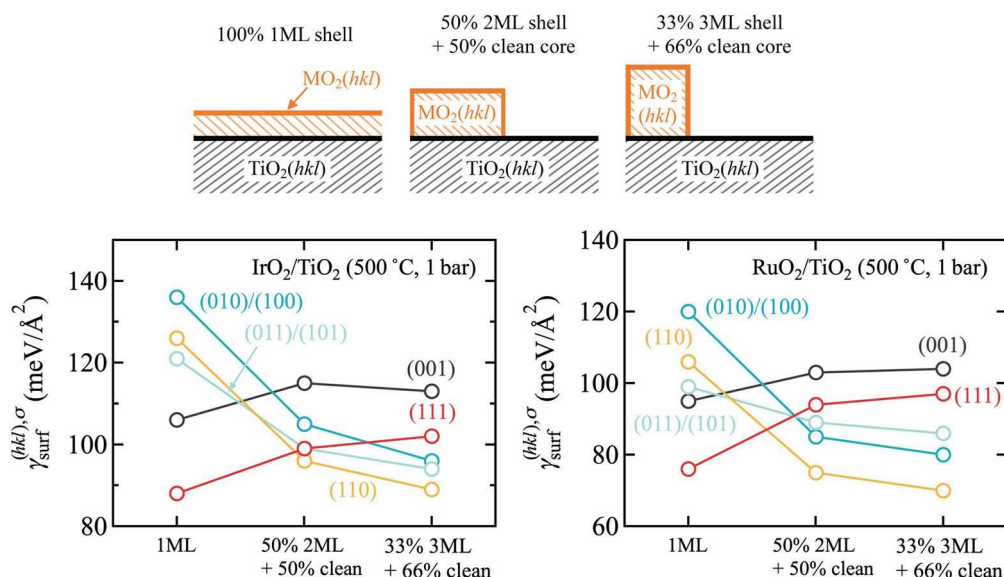


Figure 2. Computed surface free energies $\gamma_{\text{surf}}^{(hkl),\sigma}$ for one monolayer (ML) of shell material pseudomorphically covering the entire $\text{TiO}_2(hkl)$ surface, and for two ML (three ML) islands of shell material covering 50% (33%) of the $\text{TiO}_2(hkl)$ surface with the remaining 50% (66%) of the surface uncovered as illustrated in the top panel. Shown is data for all five symmetry-inequivalent low-index facets and for IrO_2 (left panel) and RuO_2 (right panel) as shell material, respectively. In all cases, the most stable surface terminations σ at the experimental gas-phase synthesis conditions of Lee et al.^[28] were assumed, in accordance with the surface phase diagrams presented in Figure 1.

$$\gamma_{\text{surf}}^{(hkl),\sigma}(2 \text{ ML MO}_2/\text{TiO}_2, 50\%) = \frac{1}{2} \left[\gamma_{\text{surf}}^{(hkl),\sigma}(2 \text{ ML MO}_2/\text{TiO}_2, 100\%) + \gamma_{\text{surf}}^{(hkl),\sigma}(\text{TiO}_2, 100\%) \right] \quad (2)$$

$$\gamma_{\text{surf}}^{(hkl),\sigma}(3 \text{ ML MO}_2/\text{TiO}_2, 33\%) = \frac{1}{3} \left[\gamma_{\text{surf}}^{(hkl),\sigma}(3 \text{ ML MO}_2/\text{TiO}_2, 100\%) + 2\gamma_{\text{surf}}^{(hkl),\sigma}(\text{TiO}_2, 100\%) \right] \quad (3)$$

Here, $\gamma_{\text{surf}}^{(hkl),\sigma}(x\text{ML MO}_2/\text{TiO}_2, 100\%)$ is the surface free energy of a model where x MLs of the shell material pseudo-morphically cover the entire $\text{TiO}_2(hkl)$ surface and $\gamma_{\text{surf}}^{(hkl),\sigma}(\text{TiO}_2, 100\%)$ is the surface free energy of the bare $\text{TiO}_2(hkl)$ surface. What Equations (2) and (3) thus evaluate is the cost, when the same total amount of shell material is not homogeneously dispersed on the entire surface as in $\gamma_{\text{surf}}^{(hkl),\sigma}(1 \text{ ML MO}_2/\text{TiO}_2, 100\%)$, but instead forms 2 or 3 ML high islands, respectively, with the remainder of the TiO_2 surface area uncovered. The simple linear superposition in Equations (2) and (3) thereby disregards any additional costs from the edges of the islands. Hence, $\gamma_{\text{surf}}^{(hkl),\sigma}(2 \text{ ML MO}_2/\text{TiO}_2, 50\%)$ and $\gamma_{\text{surf}}^{(hkl),\sigma}(3 \text{ ML MO}_2/\text{TiO}_2, 33\%)$ represent lower boundaries to the true surface free energies. According to these equations, wetting would require the $\gamma_{\text{surf}}^{(hkl),\sigma}(1 \text{ ML MO}_2/\text{TiO}_2, 100\%)$ of the fully dispersed monolayer to be lower than the surface energies of the two competing island models.

Figure 2 compiles the corresponding data for both IrO_2 and RuO_2 as shell materials and using the most stable surface terminations under the synthesis conditions by Lee et al.,^[28] cf. Figure 1. Not surprisingly, a wetting tendency is only obtained for the (001) and (111) orientation. These are the orientations with strongest adhesion, minimum strain penalty and comparable or lower MO_2 surface energies than TiO_2 . The latter lower surface energies result in fact from a qualitatively different behavior of the intended shell oxides that provides an important lead to future synthesis endeavors. Over the entire range of oxygen chemical potential shown in Figure 1, the stoichiometric termination is the most stable termination for all TiO_2 facets and their surface free energies correspondingly remain constant. In contrast, both shell MO_2 are able to stabilize O-rich terminations so that their surface free

energies decrease with increasing $\Delta\mu_{\text{O}}$. The (001) and (111) facets are able to stabilize such terminations already at lowest oxygen chemical potentials, which is why their surface free energies are already quite low for the synthesis conditions of Lee et al., cf. Figure 1. However, all other facets will eventually also stabilize such terminations, which is why more favorable wetting will generally result for increasingly O-rich conditions where the MO_2 surface free energies will continuously decrease.

Unfortunately, for gas-phase synthesis such conditions are harder to obtain. Most straightforwardly, they would be realized by lowering the temperature, cf. the temperature scales in Figure 1, but then kinetic limitations will increase. Correspondingly, growth has typically been attempted for even less O-rich conditions than the ones by Lee et al.^[28] For instance, in Ref. [19], Abb et al. even used a low oxygen partial pressure of 10^{-7} bar at 700 K. In full agreement with the understanding derived from Figure 1, they found $\text{IrO}_2(110)$ thin films at $\text{TiO}_2(110)$ not to be stable under such conditions. Elevated pressures might instead be a route to achieve more favorable O-rich conditions in gas-phase synthesis. However, in light of our results we believe electro-deposition or advanced atomic layer deposition to be more promising routes with easier access to oxidizing conditions.^[30,31] We illustrate this in Figure 3 with data for the wetting model as in Figure 2, but now computed in an aqueous environment and using the most stable surface terminations in Equation (8) that result at an applied potential corresponding to the OER equilibrium potential (see below). Under these more oxidizing conditions, a much more favorable wetting tendency is obtained. In particular for $\text{RuO}_2/\text{TiO}_2$, all but the (110) orientation now exhibit a clear preference for wetting. While the (110) orientation is thus certainly the most difficult, we stress that the simple estimates for the 2 or 3 ML island models in Figure 3 disregard any additional costs from the island edges. The corresponding surface free energies should thus be seen as lower bounds to the true surface free energies, and a wetting tendency is almost obtained already when comparing against these lower bounds (see the essentially flat orange line for the (110) facet in Figure 3). In this respect, we tentatively

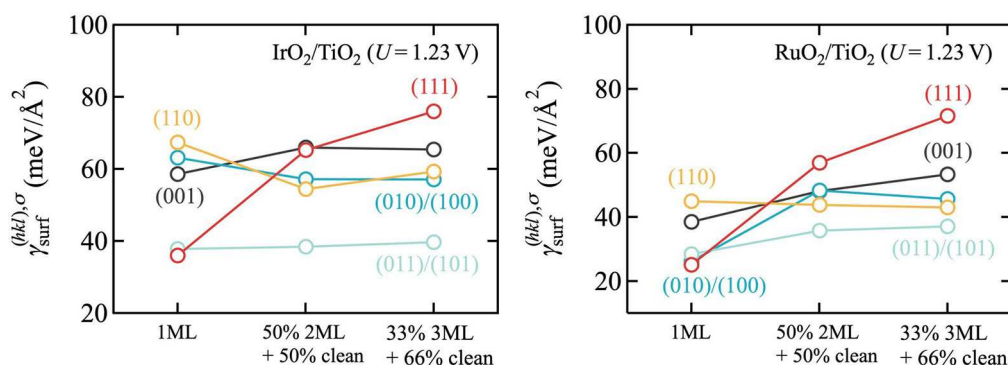


Figure 3. Same as Figure 2, but now computed in an aqueous environment and at the OER equilibrium potential ($U = 1.23 \text{ eV}$), cf. text. A much more favorable wetting tendency is obtained for these more oxidizing conditions, in particular for $\text{RuO}_2/\text{TiO}_2$.

conclude from the present thermodynamic data that growth of epitaxial core-shell particles should be feasible at sufficiently O-rich conditions. Importantly, no band gap opening is found in our calculations even for only 1 ML thick films and for all five low-index facets. This suggests that corresponding particles would also exhibit sufficient electronic conductivity as required for electrocatalytic performance.

Enhanced stability and activity

Ir and Ru oxides are the primary current OER electrocatalysts. However, even they are known to degrade in the harsh acidic PEM operation conditions, involving a hitherto only incompletely characterized transformation to some amorphous hydrous state.^[2,16,32–39] In previous work for IrO₂,^[29] we had established a simple thermodynamic descriptor for this degradation. At applied potentials in the OER regime the surface free energies were found to turn negative, indicating a potential thermodynamic instability of the rutile crystal lattice. We here obtain fully analogous results also for RuO₂ and summarize these findings in Figure 4. As detailed in the Supporting Information, more than 100 terminations σ for all five low-index facets have been computed to systematically consider the different possibilities to adsorb O, H, OH, OH₂, OOH, and OO species in (1×1) and (1×2) surface unit-cells. Figure 4 shows the surface free energies of the resulting most stable terminations as a function of the applied potential from open-circuit (0 V vs. RHE) to conditions relevant for technological PEM operation $U > 1.3$ V. The corresponding values at the OER equilibrium potential $U = 1.23$ V were also used in the wetting model in Figure 3 above. As in the analogous Figure 1 for gas-phase conditions, at each facet different terminations become most stable with increasing potential, reflected in Figure 4 by a changing slope of the $\gamma_{\text{surf}}^{(hkl),\sigma}$ line. Generally, we find the expected sequence from fully hydrated or hydroxylated surfaces at open-circuit conditions to gradually deprotonated terminations at increasing potentials until pure O-terminations and eventually terminations with higher oxidized superoxo species become most stable at OER-relevant potentials. A detailed account of these findings and their very good consistency with

existing theoretical and experimental data in particular for the best characterized (110) facet is provided in Figure S3 in the Supporting Information.

More relevant for the present context is the pronounced decrease of the surface free energies with increasing potentials. As such, it is in particular $\gamma_{\text{surf}}^{(111),\sigma}$ of the (111) facet that first turns negative already at a critical potential $U_{\text{critical}}^{\text{RuO}_2(111)} = 1.27$ V, that is, just at the OER onset. This reflects a potential thermodynamic instability, as the particle could gain energy by decaying and generating more such surfaces. With the current computational settings and pursuing the exact same approach, for IrO₂ this critical potential where $\gamma_{\text{surf}}^{(111),\sigma}$ turns negative is computed as $U_{\text{critical}}^{\text{IrO}_2(111)} = 1.39$ V. The concomitantly indicated thermodynamic stability up to higher applied potentials is fully consistent with the well-established better corrosion resistance of this material^[28,40–44] and further confirms U_{critical} as one of the useful thermodynamic descriptors for evaluating the catalyst stability. Intriguingly, when we compute exactly the same set of surface free energies for a pseudomorphic 2 ML film of RuO₂ on TiO₂, we find the decreasing surface free energies of all facets to be shifted toward higher potentials, and thereby obtain higher U_{critical} where the surface energies turn negative, cf. Figure 4. In particular, for the (111) facet which is still the one turning negative first, the critical potential is now increased to $U_{\text{critical}}^{2\text{ML RuO}_2/\text{TiO}_2(111)} = 1.36$ V, that is, 0.1 V higher than for the pure RuO₂ particle and close to the corresponding facet of pure IrO₂. For other facets, this relative increase is up to 0.2 V as detailed in Table S4 in the Supporting Information. According to this thermodynamic descriptor the core-shell RuO₂/TiO₂ particle thus exhibits trends of an increased stability, which is for all facets now essentially the same or better than for a pure IrO₂ particle.

This striking finding begs the question for its physical origin. Numerically, the shifted U_{critical} values result from increased surface free energies of the core-shell particle compared to those of the native shell oxide, cf. Figure 4. These higher values arise in turn from the additional interface formation energy and strain. Obviously, the shell oxide is not in its optimum state, and if it were for the shell oxide alone, it would be thermodynamically preferable to form a relaxed MO₂ particle. However, for the entire system a corresponding dewetting or other strain

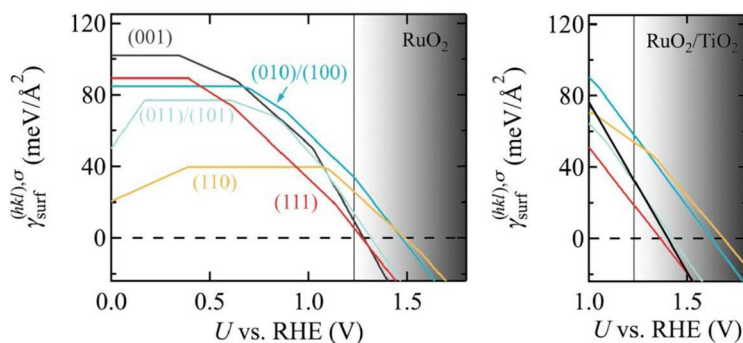


Figure 4. Computed surface free energies $\gamma_{\text{surf}}^{(hkl),\sigma}$, cf. Equation (8), of the most stable surface terminations σ for all five low-index facets of rutile RuO₂ (left panel) and 2 ML RuO₂/TiO₂ (right panel) in aqueous environment and as a function of the applied potential U from open-circuit ($U = 0$ V vs. RHE) to PEM operating conditions (shaded gray area, taken to be $U > 1.3$ V, see text). The vertical black line indicates the OER equilibrium potential $U = 1.23$ V.

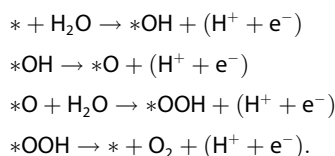
relieving alternatives like extended defects are not competitive as they would necessarily involve the formation of more surface area or expose TiO_2 with its higher surface free energy at these OER operation conditions. For thicker films this will be changed by the accumulating strain. However, for few ML epitaxial films the increased stability of once formed core-shell particles results simply out of lack of alternatives and this is how the thermodynamic descriptor should be read.

This cautious reading extends also to another interesting aspect reflected by the calculated surface free energies in Figure 4. The strong decrease in particular of $\gamma_{\text{surf}}^{(111),\sigma}$ with increasing potential as compared to the surface free energies of the other facets shows that it becomes increasingly favorable to form (111) facets. Indeed, combining the fully analogous results for native IrO_2 within a Wulff construction, we had shown in previous work that the thermodynamically preferred particle shape at OER operation conditions would be one that exclusively exhibits (111) facets.^[29] Here, the data summarized in Figure 4 indicates exactly the same thermodynamic driving force to reshape RuO_2 particles and epitaxial $\text{RuO}_2/\text{TiO}_2$ particles away from the familiar rutile form with its predominant (110) facets.^[29] However, in particular for the core-shell particle it is uncertain in how much such thermodynamics really applies. To one end, the mechanical hardness of the TiO_2 core may lead to a very slow kinetics. Additionally, as long as the shell is intact, the TiO_2 core does not contact the electrolyte and will at least be partially screened from the applied potential. It could thus well be that epitaxial core-shell particles show an increased resistance to the driving force to reshape – and concomitantly against degradation, either in terms of general mass loss or the fraction of exposed (111) facets with their particularly low U_{critical} , cf. Figure 4.

We note in passing that CHE is a simplified theoretical approach and that a negative surface energy resulting from such a treatment is not a sound indicator of what detailed physiochemical processes ensue, but merely one readily available stability descriptor which can be used to gauge trends between similar systems. This descriptor neither accounts for the chemical properties of the decomposition

products nor for mass transport effects as has been pointed out recently.^[39] Such influences can be treated approximately by simple models based on the Poisson-Nernst-Planck equations which, to lowest order, will induce shifts in the phase diagrams.^[45] For the highly similar systems considered here, we assume that these shifts are approximately constant over the range of systems studied and that our current approach delivers an acceptable semi-quantitative estimate of which structural modifications might improve the relative stability of the catalyst within its class.

According to our calculations, epitaxial $\text{RuO}_2\text{-TiO}_2$ core-shell particles would not only exhibit an improved stability, but also catalytic activity. Figure 5 demonstrates this by comparing the computed reaction energetics for the prevalent (110) facet for pristine RuO_2 and for 2 ML $\text{RuO}_2\text{-TiO}_2$, as well as for RuO_2 that is equally strained as in the epitaxial core-shell system. Specifically, this is the reaction energetics along the classic OER peroxide pathway suggested by Rossmel et al.:^[42]



Here, we note that alternative mechanistic pathways, such as the lattice oxygen mechanism, have recently been investigated.^[46,47] However, for a simple estimate of the relative activity of closely related catalyst systems, the energetic comparison of reaction intermediates within the conventional OER mechanism on mechanically (un)strained materials can still serve as a suitable descriptor. Fully consistent with previous work on $\text{RuO}_2(110)$,^[48,49] these energetics reveal the fourth, oxygen evolution step as the potential-determining one, requiring the largest minimum thermodynamic overpotential $\eta_{\text{TD}} = 0.44 \text{ V}$ to make all reaction steps exergonic. In contrast, we compute a much lower overpotential of only $\eta_{\text{TD}} = 0.26 \text{ V}$ for the coherent 2 ML film of RuO_2 on TiO_2 . This reduction results exclusively from the

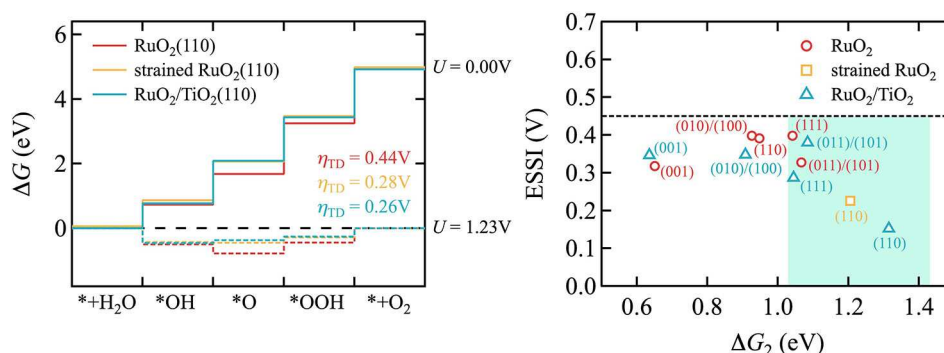


Figure 5. Left panel: Gibbs free energy change along the classic peroxide OER pathway at the (110) surface for pristine RuO_2 (red), strained RuO_2 (yellow) and core-shell 2 ML $\text{RuO}_2/\text{TiO}_2$ (blue). The four subsequent reaction steps in this pathway are described in the main text. The illustrated energy profiles are at open-circuit conditions ($U = 0 \text{ V}$, solid lines) and at the OER equilibrium potential ($U = 1.23 \text{ V}$, dotted lines). In addition, the minimum overpotentials (η_{TD}) required to make all four steps exergonic are listed. Right panel: The ESSl- ΔG_2 activity map for pristine RuO_2 (red), strained $\text{RuO}_2(110)$ (yellow) and core-shell 2 ML $\text{RuO}_2/\text{TiO}_2$ (blue). The most promising electrocatalysts fall into the highlighted area, which $1.03 \text{ eV} < \Delta G_2 < 1.43 \text{ eV}$ in junction with $\text{ESSl} < 0.45 \text{ V}$.

strain imposed on RuO₂ in the core-shell system, as demonstrated by the almost identical overpotential obtained for an equally strained RuO₂(110) surface, cf. Figure 5. This strain effectively weakens the O binding that is too strong for the native RuO₂(110) and that is correspondingly brought closer to the optimum value at the top of the volcano in the epitaxial core-shell system.^[42] Concomitant with this weakening, we also obtain a shift in the potential-determining step to the final O₂ evolution, which would then also affect the Tafel slope for such particles. To demonstrate this, we compute the Tafel slope *b* for pristine RuO₂(110) and the related core-shell system. It is governed by the apparent transfer coefficient β , which specifies the number of electrons transferred counting from the catalyst resting state to the transition state in the free energy diagram^[49,50] (see the Supporting Information for details):

$$b = \frac{59 \text{ mV/dec}}{\beta}. \quad (4)$$

As a result, the computed Tafel slope *b* of RuO₂(110) is 39.3 mVdec⁻¹ at *U* = 1.23 V. However, by increasing *U* beyond 1.57 V, the resting state changes from the surface oxo (*O) to the hydroperoxo (*OOH) intermediate, corresponding to a shift of the transition state from the second to the nearest neighbor position in the free energy profile, resulting in a Tafel slope of 118 mVdec⁻¹ (see Figure S4). This fully coincides with experimental data under OER conditions.^[51] For the core-shell system, the resting state is given by the surface hydroxo (*OH) intermediate at the OER equilibrium potential ($\eta = 0$). The transition state is the third electron transfer step following the (*OH) state. The Tafel slope thus changes twice with increasing *U*, from *b* = 23.6 to 39.3 and finally to 118 mVdec⁻¹ by consecutively moving the transition and resting states closer to each other (see Figure S5). Intriguingly, the transition bias between the two Tafel regimes (39.3 and 118 mVdec⁻¹) has been lowered for the core-shell system by more than 0.2 V from *U* = 1.57 to 1.35 V. This phenomenon of lowering the transition bias may provide a validation and a guiding principle for the successful design of such core-shell systems: the lower the transition bias, the better one achieves the desired core-shell structure. As a further activity descriptor, we adopt the electrochemical-step symmetry index (ESSI), which was proposed as a measure to quantitatively assess how close a catalyst approaches the catalytically ideal free energy profile:^[52–54]

$$\text{ESSI} = \frac{1}{n} \sum_1^n \left(\frac{\Delta G_i^+}{e^-} - E^0 \right). \quad (5)$$

Here, ΔG_i^+ are the reaction energies of those steps in the OER peroxide pathway that are larger than 1.23 eV and $E^0 = 1.23$ V is the OER equilibrium potential. For pristine RuO₂ the relevant ΔG_i^+ are the third and fourth steps in Figure 5 (left), that is, *OOH formation and O₂ evolution, and the corresponding ESSI descriptor becomes 0.391 V. For the core-shell system, the ESSI descriptor yields 0.153 V which is much

smaller and indicates that it is significantly closer to the ideal catalyst than pristine RuO₂. The reduction is, as discussed above, due to the strain induced destabilization of the O binding in the *O state. The equally strained RuO₂ has an intermediate ESSI value of 0.226 V. In spite of the nearly identical overpotentials η_{TD} of the core-shell and the strained RuO₂ system, this large ESSI change can simply be attributed to a change in the number of terms *n* contributing to the average in Equation (5). The second reaction step at the strained RuO₂ is slightly below (by –0.02 eV) the threshold of 1.23 eV while it is slightly above (+0.08 eV) for the core-shell system. Such large deviations in the ESSI descriptor by a threshold induced discretization error for the average should be taken with a grain of salt based on typical DFT errors. The simple η_{TD} estimate is more robust for such cases. As shown in Figure 5 (right), we can generally conclude though that the RuO₂/TiO₂ core-shell system, especially for the most relevant (011)/(101), (110) and (111) surfaces, could provide a promising RuO₂-based OER electrode as the free-energy change of the second reaction step ranges between 1.03 and 1.43 eV and it exhibits ESSI values below 0.45 V.^[53]

Conclusions

Systematically analyzing the interfacial stability, strain and surface free energies, our first-principles calculations predict a general thermodynamic feasibility of epitaxial core-shell particles, in which an ultrathin film of RuO₂ coherently encapsulates a rutile-structured TiO₂ core. A high directional dependence of adhesion and lattice mismatch disfavors in particular the (110) orientation, which suffers from maximum strain and offers the smallest density of interfacial bonds. While the same trend with regards to direction is obtained for IrO₂, its intrinsically higher surface energies render this oxide a less suitable material for such core-shell concepts.

A key aspect for the practical realization is the ability of both studied MO₂ to stabilize O-rich surface terminations at more oxidizing conditions. This increasingly lowers their surface free energies relative to TiO₂, for which only stoichiometric terminations are found as most stable up to high oxygen chemical potentials. Generally favoring wetting, this points towards growth protocols operating at oxidizing conditions, as for example achievable by electrodeposition. Apart from reducing the precious oxide content, our calculations further indicate two additional benefits of corresponding pseudomorphic core-shell particles. On the one end, an increased stability at OER operation conditions results as the implied higher surface area and/or exposure of TiO₂ penalizes a dewetting or strain-relieving formation of extended defects. On the other end, the additional strain in particular of the prevalent (110) facet leads to a lowered thermodynamic overpotential for few monolayer, coherent RuO₂ films at rutile TiO₂. We hope that these insights will stimulate advanced growth endeavors to overcome the presently realized massively loaded composites with their incoherent thick, precious oxide films towards tailored

epitaxial core-shell particles with a predicted increased stability and activity at simultaneously minimized mass loading.

Methods

In order to assess the interfacial stability we use ab initio thermodynamics^[55] to calculate two general key quantities, the interface formation energy $\gamma_{\text{interf}}^{(hkl)}$ and the work of adhesion $W_{\text{adh}}^{(hkl)}$ of a stoichiometric interface with crystallographic orientation (hkl) . The prior indicates the cost of creating the interface from the respective bulk materials and is defined as

$$\gamma_{\text{interf}}^{(hkl)} = \frac{1}{A^{(hkl)}} \left\{ G_{\text{interf}}^{(hkl)} - \nu_{\text{Ti}}^{(hkl)} G_{\text{TiO}_2, \text{bulk}} - \nu_{\text{M}}^{(hkl)} G_{\text{MO}_2, \text{bulk}} \right\}. \quad (6)$$

Here, $A^{(hkl)}$ is the area of the interface model employed in the calculations, $G_{\text{interf}}^{(hkl)}$ its Gibbs free energy, $\nu_{\text{Ti}}^{(hkl)}$ its number of Ti atoms, and $\nu_{\text{M}}^{(hkl)}$ its number of M=Ir or Ru atoms. $G_{\text{TiO}_2, \text{bulk}}$ is the Gibbs free energy per TiO₂ formula unit of a rutile bulk unit-cell and $G_{\text{MO}_2, \text{bulk}}$ correspondingly the Gibbs free energy per MO₂ formula unit of a rutile bulk unit-cell. The work of adhesion is the reversible work required to separate the interface into two free surfaces in vacuum

$$W_{\text{adh}}^{(hkl)} = \frac{1}{A^{(hkl)}} \left\{ G_{\text{interf}}^{(hkl)} - G_{\text{TiO}_2, \text{surf}}^{(hkl)} - G_{\text{MO}_2, \text{surf}}^{(hkl)} \right\}, \quad (7)$$

where $G_{\text{TiO}_2, \text{surf}}^{(hkl)}$ and $G_{\text{MO}_2, \text{surf}}^{(hkl)}$ are the Gibbs free energies of surface models of TiO₂ and MO₂, respectively, exhibiting the (hkl) facet and the same stoichiometric surface termination as the interface model.

In analogy to $\gamma_{\text{interf}}^{(hkl)}$, the central quantity determining the thermodynamic stability of a specific facet of a core-shell particle with termination σ containing $\nu_{\text{M}}^{(hkl), \sigma}$, $\nu_{\text{O}}^{(hkl), \sigma}$, and $\nu_{\text{H}}^{(hkl), \sigma}$ with M=(Ir or Ru), O, and H atoms, respectively, in an aqueous environment and under an applied potential U is the surface free energy

$$\gamma_{\text{surf}}^{(hkl), \sigma}(U) = \frac{1}{A^{(hkl)}} \left\{ \begin{array}{l} G_{\text{surf}}^{(hkl), \sigma} - \nu_{\text{Ti}}^{(hkl)} G_{\text{TiO}_2, \text{bulk}} - \nu_{\text{M}}^{(hkl), \sigma} G_{\text{MO}_2, \text{bulk}} - \\ \left[\nu_{\text{O}}^{(hkl), \sigma} - 2 \left(\nu_{\text{Ti}}^{(hkl)} + \nu_{\text{M}}^{(hkl), \sigma} \right) \right] \mu_{\text{H}_2\text{O}} - \\ \left[\nu_{\text{H}}^{(hkl), \sigma} - 2 \left(\nu_{\text{O}}^{(hkl), \sigma} - 2 \left(\nu_{\text{Ti}}^{(hkl)} + \nu_{\text{M}}^{(hkl), \sigma} \right) \right) \right] \\ \left(\mu_{\text{H}^+}^{\text{aq}} + \mu_{\text{e}^-} \right) \end{array} \right\} \quad (8)$$

Here, the second line accounts for any off-stoichiometries of the surface termination σ by releasing or taking water molecules from the water environment represented by the chemical potential of water $\mu_{\text{H}_2\text{O}}$ at normal conditions. As a byproduct, the surface may be (de)protonated. At the metallic surface, we assume this to proceed in form of a proton coupled electron transfer, thus introducing as relevant reservoir the sum $(\mu_{\text{H}^+}^{\text{aq}} + \mu_{\text{e}^-})$ of the electrochemical potential of a solvated proton and the electron electrochemical potential in the

system. Within the computational hydrogen electrode (CHE) concept of Nørskov and coworkers^[56] $(\mu_{\text{H}^+}^{\text{aq}} + \mu_{\text{e}^-}) = \frac{1}{2} \mu_{\text{H}_2} + eU$, where μ_{H_2} is the chemical potential of hydrogen gas at normal conditions and the applied potential U is referenced to the reversible hydrogen electrode (RHE). Here, any treatment of aqueous surrounding is not included in our model. We note that both the solvent dielectric environment and specific interactions with surrounding water molecules can lead to different absolute energetics.^[57,58] In contrast, we assume such solvent effects to be small when comparing the energetics of materials within the same class differing due to mechanical modifications.

When instead focusing on the stability of a facet in an oxygen gas environment, the surface free energy is analogously given as

$$\gamma_{\text{surf}}^{(hkl), \sigma}(\Delta\mu_{\text{O}}) = \frac{1}{A^{(hkl)}} \left\{ \begin{array}{l} G_{\text{surf}}^{(hkl), \sigma} - \nu_{\text{Ti}}^{(hkl)} G_{\text{TiO}_2, \text{bulk}} - \nu_{\text{M}}^{(hkl), \sigma} G_{\text{MO}_2, \text{bulk}} - \\ \left[\nu_{\text{O}}^{(hkl), \sigma} - 2 \left(\nu_{\text{Ti}}^{(hkl)} + \nu_{\text{M}}^{(hkl), \sigma} \right) \right] \left(\frac{1}{2} E_{\text{O}_2} + \Delta\mu_{\text{O}} \right) \end{array} \right\}, \quad (9)$$

where the relative chemical potential of oxygen, $\Delta\mu_{\text{O}} = \Delta\mu_{\text{O}}(T, p)$, now summarizes the dependence of the surface free energy on temperature T and oxygen pressure p .^[59] In detail, as the O₂ environment forms an ideal-gas-like reservoir, the chemical potential of oxygen, μ_{O} , is expressed as

$$\mu_{\text{O}}(T, p) = \mu_{\text{O}}(T, p^\circ) + \frac{1}{2} kT \ln \left(\frac{p}{p^\circ} \right). \quad (10)$$

The chemical potentials of oxygen at the standard state pressure are obtained from reported experiments.^[60] Note that both Equations (8) and (9) can also be used for the calculation of the native oxide surfaces ($\nu_{\text{Ti}}^{(hkl)} = 0$ and using the $G_{\text{surf}}^{(hkl), \sigma}$ from a corresponding oxide slab model), as well as for the calculation of the Gibbs free energy change of a reaction step $\Delta G = A^{(hkl)} \left(\gamma_{\text{surf1}}^{(hkl), \sigma}(\Delta\mu_{\text{O}}) - \gamma_{\text{surf2}}^{(hkl), \sigma}(\Delta\mu_{\text{O}}) \right)$ where the two surface terminations surf1 and surf2 differ in their composition according to the reaction step studied.

For the differences of solid-state Gibbs free energies entering Equations (6)–(9) we follow the approach of Reuter and Scheffler^[59] and approximate them with the difference of the corresponding zero-point energy (ZPE)-corrected^[61] total energy contributions. These total energies are then obtained by first-principles density-functional theory (DFT) calculations with the FHI-aims code^[62] and within the generalized-gradient approximation using the Perdew-Burke-Ernzerhof (PBE) functional.^[63] Here, we note that it is well established that the PBE level of theory provides an adequate description for the metallic rutile oxides, for example, the reported better agreement of the density-of-states of IrO₂ with experimental XPS spectra compared to hybrid functionals,^[64] and we thus use the PBE for IrO₂ and RuO₂. ZPE and entropic contributions to the molecular chemical potentials $\mu_{\text{H}_2\text{O}}$ and μ_{H_2} were obtained from experimental data and reference tables.^[65,66] To achieve a more

accurate electronic structure of the metal-insulator interface system, Hubbard-corrected DFT has been applied to the Ti3d states using an effective on-site parameter of 4.5 eV.^[67] Double counting in this DFT + *U* approach has been treated in the fully localized limit.^[67] A detailed account of the computational settings employed in the DFT calculations is provided in the Supporting Information.

Acknowledgements

This research was supported by the <Kopernikus/P2X-2 programme (funding number 03SFK2V0-2) of the German Federal Ministry of Education and Research (BMBF). We acknowledge PRACE for awarding us access to Curie at GENCI@CEA, France, and Daniel Opalka for fruitful discussions. Open Access funding enabled and organized by Projekt DEAL.

Conflict of Interest

The authors declare no conflict of interest.

Data Availability Statement

The data that support the findings of this study are available in the supplementary material of this article.

Keywords: ab initio thermodynamics core-shell particles · DFT calculations · electrolysis · oxygen evolution reaction

- [1] M. Carmo, D. L. Fritz, J. Mergel, D. Stolten, *Int. J. Hydrogen Energy* **2013**, *38*, 4901–4934.
- [2] S. Cherevko, S. Geiger, O. Kasian, N. Kulyk, J.-P. Grote, A. Savan, B. R. Shrestha, S. Merzlikin, B. Breitbach, A. Ludwig, K. J. J. Mayrhofer, *Catal. Today* **2016**, *262*, 170–180.
- [3] A. Buttler, H. Spliethoff, *Renew. Sust. Energ. Rev.* **2018**, *82*, 2440–2454.
- [4] M. Bernt, A. Siebel, H. A. Gasteiger, *J. Electrochem. Soc.* **2018**, *165*, F305.
- [5] A. Marshall, B. Børresen, G. Hagen, S. Sunde, M. Tsympkin, R. Tunold, *Russ. J. Electrochem.* **2006**, *42*, 1134–1140.
- [6] A. T. Marshall, R. G. Haverkamp, *Electrochim. Acta* **2010**, *55*, 1978–1984.
- [7] E. Fabbri, A. Habereder, K. Waltar, R. Kötz, T. J. Schmidt, *Catal. Sci. Technol.* **2014**, *4*, 3800–3821.
- [8] J. Y. Lim, G. Rahman, S. Y. Chae, K.-Y. Lee, C.-S. Kim, O.-S. Joo, *Int. J. Energy Res.* **2014**, *38*, 875–883.
- [9] J. Tong, Y. Liu, Q. Peng, W. Hu, Q. Wu, *J. Mater. Sci.* **2017**, *52*, 13427–13443.
- [10] B. M. Tackett, W. Sheng, S. Kattel, S. Yao, B. Yan, K. A. Kuttiyil, Q. Wu, J. G. Chen, *ACS Catal.* **2018**, *8*, 2615–2621.
- [11] S. Siracusano, V. Baglio, C. D'Urso, V. Antonucci, A. S. Arico, *Electrochim. Acta* **2009**, *54*, 6292–6299.
- [12] P. Mazúr, J. Polonský, M. Paidar, K. Bouzek, *Int. J. Hydrogen Energy* **2012**, *37*, 12081–12088.
- [13] E. Oakton, D. Lebedev, M. Povia, D. F. Abbott, E. Fabbri, A. Fedorov, M. Nachttegaal, C. Coperét, T. J. Schmidt, *ACS Catal.* **2017**, *7*, 2346–2352.
- [14] S. M. Alia, B. Rasimick, C. Ngo, K. C. Neyerlin, S. S. Kocha, S. Pylypenko, H. Xu, B. S. Pivovar, *J. Electrochem. Soc.* **2016**, *163*, F3105.
- [15] M. Bernt, H. A. Gasteiger, *J. Electrochem. Soc.* **2016**, *163*, F3179–F3189.
- [16] P. Lettenmeier, J. Majchel, L. Wang, V. A. Saveleva, S. Zafeiratos, E. R. Savinova, J.-J. Gallet, F. Bournel, A. S. Gago, K. A. Friedrich, *Chem. Sci.* **2018**, *9*, 3570–3579.
- [17] Umicore AG & Co. <https://pmc.umicore.com/en/products/elyst-ir75-0480>.
- [18] T. Akita, M. Okumura, K. Tanaka, S. Tsubota, M. Haruta, *J. Electron Microsc.* **2003**, *52*, 119–124.
- [19] M. J. S. Abb, T. Weber, L. Glatthaar, H. Over, *Langmuir* **2019**, *35*, 7720–7726.
- [20] W. Liu, J. C. Li, W. T. Zheng, Q. Jiang, *Phys. Rev. B* **2006**, *73*, 205421.
- [21] J.-S. Park, Y.-K. Jung, K. T. Butler, A. Walsh, *J. Phys. E* **2019**, *1*, 016001.
- [22] D. Y. Dang, L. Y. Shi, J. L. Fan, H. R. Gong, *Surf. Coat. Technol.* **2015**, *276*, 602–605.
- [23] C. L. McDaniel, S. J. Schneider, *J. Res. Natl. Bur. Stand.* **1967**, *71*, 119.
- [24] C. Noguera, *Physics and Chemistry at Oxide Surfaces*, Cambridge University Press, **1996**.
- [25] T. Wang, J. Jelic, D. Rosenthal, K. Reuter, *ChemCatChem* **2013**, *5*, 3398–3403.
- [26] J. Timmermann, F. Kraushofer, N. Resch, P. Li, Y. Wang, Z. Mao, M. Riva, Y. Lee, C. Staacke, M. Schmid, C. Scheurer, G. S. Parkinson, U. Diebold, K. Reuter, *Phys. Rev. Lett.* **2020**, *125*, 206101.
- [27] J. Timmermann, Y. Lee, C. G. Staacke, J. T. Margraf, C. Scheurer, K. Reuter, *J. Chem. Phys.* **2021**, *155*, 244107.
- [28] Y. Lee, J. Suntivich, K. J. May, E. E. Perry, Y. Shao-Horn, *J. Phys. Chem. Lett.* **2012**, *3*, 399–404.
- [29] D. Opalka, C. Scheurer, K. Reuter, *ACS Catal.* **2019**, *9*, 4944–4950.
- [30] M. Yousefpour, A. Shokuyh, *Superlattices Microstruct.* **2012**, *51*, 842–853.
- [31] S. Schlicht, P. Büttner, J. Bachmann, *ACS Appl. Energ. Mater.* **2019**, *2*, 2344–2349.
- [32] P. Steegstra, M. Busch, I. Panas, E. Ahlberg, *J. Phys. Chem. C* **2013**, *117*, 20975–20981.
- [33] T. Reier, D. Teschner, T. Lunkenbein, A. Bergmann, S. Selve, R. Kraehnert, R. Schlögl, P. Strasser, *J. Electrochem. Soc.* **2014**, *161*, F876.
- [34] D. F. Abbott, D. Lebedev, K. Waltar, M. Povia, M. Nachttegaal, E. Fabbri, C. Coperét, T. J. Schmidt, *Chem. Mater.* **2016**, *28*, 6591–6604.
- [35] P. Lettenmeier, L. Wang, U. Golla-Schindler, P. Gazdzicki, N. A. Cañas, M. Handl, R. Hiesgen, S. S. Hosseiny, A. S. Gago, K. A. Friedrich, *Angew. Chem. Int. Ed.* **2016**, *128*, 752–756.
- [36] E. Willinger, C. Massu'e, R. Schlögl, M. G. Willinger, *J. Am. Chem. Soc.* **2017**, *139*, 12093–12101.
- [37] T. Weber, J. Frommer, M. J. S. Abb, B. Herd, O. Khalid, M. Rohnke, P. H. Lakner, J. Evertsson, S. Volkov, F. Bertram, R. Znaiguia, F. Carla, V. Vonk, E. Lundgren, A. Stierle, H. Over, *ACS Catal.* **2019**, *9*, 6530–6539.
- [38] A. Goryachev, M. E. C. Pascuzzi, F. Carl'a, T. Weber, H. Over, E. J. M. Hensen, J. P. Hofmann, *Electrochim. Acta* **2020**, *336*, 135713.
- [39] H. Over, *ACS Catal.* **2021**, *11*, 8848–8871.
- [40] S. Trasatti, *J. Electroanal. Chem.* **1980**, *111*, 125–131.
- [41] R. Kötz, H. J. Lewerenz, S. Stucki, *J. Electrochem. Soc.* **1983**, *130*, 825–829.
- [42] J. Rossmeisl, Z.-W. Qu, H. Zhu, G.-J. Kroes, J. K. Nørskov, *J. Electroanal. Chem.* **2007**, *607*, 83–89.
- [43] T. Reier, M. Oezaslan, P. Strasser, *ACS Catal.* **2012**, *2*, 1765–1772.
- [44] N. Danilovic, R. Subbaraman, K.-C. Chang, S.-H. Chang, Y. Kang, J. Snyder, A. P. Paulikas, D. Strmcnik, Y.-T. Kim, D. Myers, V. R. Stamenkovic, N. M. Markovic, *Angew. Chem. Int. Ed.* **2014**, *53*, 14016–14021; *Angew. Chem.* **2014**, *126*, 14240–14245.
- [45] C. Griesser, H. Li, E.-M. Wernig, D. Winkler, N. Shakibi Nia, T. Mairegger, T. Götsch, T. Schachinger, A. Steiger-Thirfeld, S. Penner, D. Wielend, D. Egger, C. Scheurer, K. Reuter, J. Kunze-Liebhäuser, *ACS Catal.* **2021**, *11*, 4920–4928.
- [46] A. Zagalskaya, V. Alexandrov, *ACS Catal.* **2020**, *10*, 3650–3657.
- [47] K. Schweinar, B. Gault, I. Mouton, O. Kasian, *J. Phys. Chem. Lett.* **2020**, *11*, 5008–5014.
- [48] V. Sumaria, D. Krishnamurthy, V. Viswanathan, *ACS Catal.* **2018**, *8*, 9034–9042.
- [49] K. S. Exner, *Electrochim. Acta* **2021**, *375*, 137975.
- [50] K. S. Exner, H. Over, *ACS Catal.* **2019**, *9*, 6755–6765.
- [51] K. A. Stoerzinger, L. Qiao, M. D. Biegalski, Y. Shao-Horn, *J. Phys. Chem. Lett.* **2014**, *5*, 1636–1641.
- [52] N. Govindarajan, J. M. García, E. J. Meijer, F. Calle-Vallejo, *Curr. Opin. Electrochem.* **2018**, *8*, 110–117.
- [53] K. S. Exner, *J. Phys. Chem. C* **2019**, *124*, 822–828.
- [54] O. Piqué, F. Illas, F. Calle-Vallejo, *Phys. Chem. Chem. Phys.* **2020**, *22*, 6797–6803.
- [55] K. Reuter, *Catal. Lett.* **2016**, *146*, 541–563.
- [56] J. K. Nørskov, J. Rossmeisl, A. Logadottir, L. R. K. J. Lindqvist, J. R. Kitchin, T. Bligaard, H. Jonsson, *J. Phys. Chem. B* **2004**, *108*, 17886–17892.
- [57] J. A. Gauthier, C. F. Dickens, L. D. Chen, A. D. Doyle, J. K. Nørskov, *J. Phys. Chem. C* **2017**, *121*, 11455–11463.

- [58] S. Ringe, N. G. Hörmann, H. Oberhofer, K. Reuter, *Chem. Rev.* **2021**, doi: 10.1021/acs.chemrev.1c00675.
- [59] K. Reuter, M. Scheffler, *Phys. Rev. B* **2001**, *65*, 035406.
- [60] M. Chase, NIST-JANAF Thermochemical Tables, American Institute of Physics, **1998**.
- [61] Q. Sun, K. Reuter, M. Scheffler, *Phys. Rev. B* **2003**, *67*, 205424.
- [62] V. Blum, R. Gehrke, F. Hanke, P. Havu, V. Havu, X. Ren, K. Reuter, M. Scheffler, *Comput. Phys. Commun.* **2009**, *180*, 2175–2196.
- [63] J. P. Perdew, K. Burke, M. Ernzerhof, *Phys. Rev. Lett.* **1996**, *77*, 3865.
- [64] Y. Ping, G. Galli, W. A. Goddard III, *J. Phys. Chem. C* **2015**, *119*, 11570–11577.
- [65] W. S. Benedict, N. Gailar, E. K. Plyler, *J. Chem. Phys.* **1956**, *24*, 1139–1165.
- [66] K. K. Irikura, *J. Phys. Chem. Ref. Data* **2007**, *36*, 389–397.
- [67] M. Kick, K. Reuter, H. Oberhofer, *J. Chem. Theory Comput.* **2019**, *15*, 1705–1718.

Manuscript received: January 4, 2022

Revised manuscript received: March 11, 2022

Accepted manuscript online: March 16, 2022